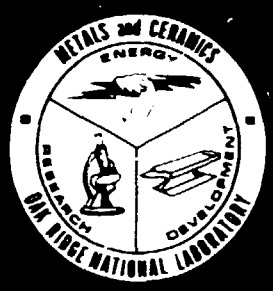

Lib. 556

10-5-78

ORNL-5437

MASTER

Metals and Ceramics Division Materials Science Annual Progress Report for Period Ending June 30, 1978

ORNL-5437
Distribution
Category UC-25

Contract No. W-7405-eng-26

METALS AND CERAMICS DIVISION MATERIALS SCIENCE ANNUAL PROGRESS REPORT FOR PERIOD ENDING JUNE 30, 1978

Compiled by C. J. McHargue, Manager, Materials Science

Edited by Sigfred Peterson

Date Published: September 1978

OAK RIDGE NATIONAL LABORATORY
Oak Ridge, Tennessee 37830
operated by
UNION CARBIDE CORPORATION
for the
DEPARTMENT OF ENERGY

CONTENTS

BLANK PAGE

SUMMARY

1. STRUCTURE OF MATERIALS

1.1 Theoretical Research

Our calculation of the electron-phonon interaction in niobium and the experimental confirmation obtained by measuring the phonon line width with neutrons was singled out by the American Institute of Physics for its newsworthiness. Our studies on electron-phonon interactions have allowed us to find a new correlation in the data on the electron-phonon contribution to thermal resistance, to accurately predict the high-temperature electrical resistivity of a transition metal for the first time, and to show why p-wave superconductivity is not observed in palladium.

Since the coherent potential approximation was proposed in 1967, the goal has been to calculate the electronic states for a real alloy system within this framework with no further simplifying approximations. We achieved this goal with our KKR-CPA calculations on copper-nickel alloys. Our CPA calculations on palladium hydride have explained the experimental measurements on that nonstoichiometric material very well.

In the area of lattice defect theory, we have made continuous progress in radiation damage studies. We have analyzed the depth dependence of void swelling in self-ion-irradiated metals by using the generalized rate theory model of void swelling. Our finding that the deposited self-ions are the important physical source of the depth-dependent swelling is a significant result in view of the development of simulation experiments. We have also developed a unified rate theory model for the nucleation and growth of interstitial dislocation loops. This model has been used to interpret some of the results of electron irradiation experiments.

An essential part of our understanding of the behavior of solids in various environments involves interactions that occur at the surface. Theoretical studies of this program are focused on atomic and molecular bonding with (metallic) surfaces with the goal to determine the relative roles of various surface characteristics (defects, "impurity overlayers," etc.) in chemisorption and molecular dissocation processes. This work is intended to provide an understanding of how features of the surface electronic structure affect adsorption and dissociation mechanisms.

1.2 X-Ray Diffraction Research

Synchrotron radiation was employed in an attempt to detect superheavy elements. Thresholds for elemental detectability were significantly reduced with this tunable excitation source. Analyses of x-ray diffraction data from monoclinic europia crystals are being coupled with improvements in our theoretical understanding of secondary extinction effects. Studies of the effects of chemical environment on the crystal structure of monoclinic europia continue to suggest sensitivity

to water vapor. Small angle x-ray scattering experiments with coals, polymers, and irradiated metals are reviewed.

1.3 Fundamental Ceramics Studies

The erosion of ceramics is observed to involve both brittle and plastic processes. The study of ceramic commercial refractories and ceramic single crystals reveals both fracture and shear displacement at particle impact sites. In some circumstances, melting is detected at the damage surface. The study of the micromineralogy and microporosity of coals is continuing. Near-infrared microscopy has been used to reveal microstructural features of coal that are opaque in the visible spectrum. Features exhibiting birefringence and having variably oriented domains were noted by infrared microscopy. The microporosity and micromineral sizes were found to correlate well with evaluations of pore and mineral dimensions made by small angle x-ray scattering.

1.4 Preparation and Synthesis of High-Temperature and Special Service Materials

We report continued progress with the internal zone growth technique, which holds much promise as a means of synthesizing high-temperature crystals and directionally solidified eutectics. Experimentally we have confirmed the predictions of the mathematical model that one can avoid or reduce the difficulties associated with the thermal instability by proper selection of sample diameter, generator frequency, and physical geometry. A technique was developed to reduce the adverse effect of the thermal instability in Cr_2O_3-Mo compacts. Consideration of the thermodynamics of gas-metal reactions yielded two criteria, which establish principles of composition control and alloying in metal oxide-metal eutectic composites. These criteria have been used for predicting the stability and controlling the composition of several binary and ternary eutectics.

A computer model of the boundary-layer diffusion problem for eutectic composite growth from a thin liquid film — as in edge-defined film-fed growth — has been developed. We report the results of a program to directionally solidify metal-metal boride and metal carbide eutectics. Excellent allignment of WCoB lamellae have been obtained for the Co-WCoB system. The presence of oxygen as an impurity has inhibited progress on the Co-WC system. Dense composites of WC-TiB_2 and TiB_2-Fe have been prepared by liquid-phase hot-pressing. These hard composites have potential for tool application, and their mechanical properties are now being studied. The large-diameter hydrothermal autoclave and furnace have been constructed. Quartz crystals of sufficient size for direct measurement of their electronic oscillator quality have been grown. Single-crystal boules of Fe_2SiO_4 (fayalite) up to 10 mm in diameter were grown by the Czochralski method. The melting behavior and possible defect structure of these crystals are reported. By the Bridgman

method, $RbCaF_3$, ThF_4, $ThCl_4$, and $ThBr_4$ have been grown. Crystals of $ThCl_4$ were grown doped with ^{249}Bk and $ThBr_4$ was doped with Tb. The resulting samples are used in an electron paramagnetic resonance and optical study of such crystals.

2. DEFORMATION AND MECHANICAL PROPERTIES

2.1 Physical Metallurgy

The shape memory effect (SME) in U–14 at. % Nb was characterized and found to be two-way. The strain recovery was associated with the α'' (monoclinic) to γ° (tetragonal) phase transformation. At low strains a uranium alloy containing 7.5 wt % Nb and 2.5 wt % Zr exhibited pseudoelasticity, underwent elastic twinning, and developed substantial texture. Pole figures were used to identify the preferred orientations, which profoundly accentuated an aging-induced shape instability in this alloy. Factors such as lattice curvature, wide subgrain distributions, and deformation microstructure strongly influenced the recrystallization tendencies of homogeneously deformed tantalum single crystals.

2.2 Grain Boundary Segregation and Fracture

Fracture at 77 K shows phosphorus to segregate to grain boundaries and embrittle Fe–3% Si bicrystals. Grain boundary phosphorus concentrations of 30 at. % were observed for specimens with an average concentration of 1200 ppm.

Phosphorus and sulfur were found on fracture surfaces of stainless steel that contained creep cavities. An association of the impurities with the creep cavities was inferred.

3. PHYSICAL PROPERTIES AND TRANSPORT PHENOMENA

3.1 Mechanisms of Surface and Solid-State Reactions

Multiple modes of tritium diffusion in TiO_2 were identified, and initial results of a parallel study of tritium diffusion in Al_2O_3 also suggested the existence of more than one mode of diffusion. Measurements of tracer diffusivities of Ni and Ti in NiO between 1000 and 1500°C verified doubly ionized Ni vacancies as the dominant defect in NiO and provided evidence of vacancy-impurity interactions. The theory of diffusion in an alloy in dissociative equilibrium was developed further, and the negative solute diffusivity enhancement observed in very dilute Pb-Cd alloys was interpreted as a reflection of the formation of interstitial-substitutional solute pairs. Studies of diffusion in Pb-Ni and Sn-Au alloys are expected to provide additional information concerning dissociative diffusion mechanisms. Very pure (99.99%+) FeS was synthesized and used as the starting material for growing single

crystals of FeS. Investigations of the kinetics and morphology of sulfide scales formed on Fe at 700–900°C were continued. Highly accurate and reliable techniques for measuring oxidation kinetics at elevated temperatures (up to 1500°C) were developed, and a comparative study of the oxidation of zirconium and Zircaloy-4 was initiated. Oxygen diffusivities in the oxide and oxygen-stabilized alpha layer on Zircaloy-4 were determined. A computer program was written to model oxidation processes in terms of mass flow in a one-dimensional, multiphase, moving boundary system with finite geometry.

3.2 Physical Properties Research

A method was developed to calculate the lattice thermal conductivity (λ) of alloys as a function of temperature and composition from readily available data on atomic or molecular species in the alloy. The λ of SrF_2 was measured from 80 to 400 K and the $1/\lambda$ results disagree by a factor of 3 with calculations using the Liebfried and Schloman equation. An apparatus was constructed to study the factors that influence the λ of epoxy-containing materials at low temperatures. A correlation describing the interaction of phonons with conduction electrons is in fair agreement with a simple theoretical estimate. Measurements of the Soret effect of molten Ag–Te solutions show the heat of transport to decrease at high temperatures. The λ of commercially pure Nb was measured from 100 to 1400 K; the Lorenz ratio appears to be near L_0 with a small lattice contribution. Analysis of λ measurements on alloys of 50 Cu–50 Ni and 50 Ag–50 Pd (at. %) when combined with calculated lattice contributions yield positive deviations from the Sommerfeld limit of the Lorenz function. Data analysis on two Cr-Fe alloys shows that the lattice contribution in Cr is significant. The total hemispherical emittance of black chromium coatings on copper was unstable at 580 K. Our λ measurements on a graphite λ standard from 80 to 900 K agree to within ±2% with results by others. The thermal conductivity of ordered alloys is greater than that of disordered alloys for Ni_4Mo and $V(Fe_{0.22}Co_{0.78})_3$.

3.3 Superconducting Materials

A study of flux pinning by a single grain boundary in Nb bicrystals resulted in an unambiguous determination of the elementary pinning force between grain boundary and flux line. Since the grain boundaries were symmetric tilt boundaries, it could be concluded that the pinning interaction was not due to H_{c_2} anisotropy. Work on the strain sensitivity of the critical current density, J_c, of bronze-processed multifilamentary Nb_3Sn conductors has shown the importance of Kirkendall voids in the region of the Nb_3Sn–bronze interface and has indicated that short reaction times, resulting in smaller void densities and thinner Nb_3Sn layers, are advantageous. Measurements of the critical field H_{c_2} in such materials as a function of temperature and strain have shown larger changes in H_{c_2} than would be expected from the variation of transition temperature, T_c. Measurements of J_c and H_{c_2} as functions of

temperature and strain in a monofilament bronze-processed conductor have indicated that much of the strain dependence of J_c is due to changes in the fundamental properties H_{c_2} and I_c rather than to microstructural changes or cracks.

4. RADIATION EFFECTS

The Radiation Effects Program is organized to provide an understanding of the effects of composition and microstructure on the structure and properties of materials irradiated at elevated temperatures. Activities supported by the Division of Materials Sciences complement and support work sponsored by the Breeder Reactor and Magnetic Fusion Energy Programs by examining relatively simple systems and by conducting studies aimed at identifying mechanisms that control damage.

A generalized rate theory model has been formulated to describe microstructural evolution during particle irradiation. The model accounts for temporal and spatial variations in defect production and thus is applicable to ion and electron irradiation situations. A theory of impurity trapping of point defects has been developed and incorporated into the model. Effects of trapping on void nucleation and growth and on irradiation creep have been examined in detail. A quantitative description of the temperature shift of swelling with changes in dose rate has been developed and applied to neutron and ion bombardment of nickel. A numerical technique for calculating diffusion of point defects to dislocation loops has been used to study stress-assisted diffusion. Faulted loops are found to act as stronger sinks than edge dislocations. Results have been used to calculate loop growth kinetics for nickel during electron irradiation.

The effects of amount and method of injection of helium on void nucleation and growth during heavy-ion bombardment of nickel and of low- and high-swelling stainless steels are presented. Results depend on the material studied. A technique for simultaneously bombarding a material with hydrogen, helium, and heavy ions with only two accelerators is described. Effects of stress on the growth of bubbles of helium, introduced by injection from an accelerator, have been studied in a high-purity stainless steel. Bubbles located at special positions such as triple point junctions or grain boundaries grow significantly faster than those within the grains. Studies of heavy-ion damage in Ni-Mo alloys that maintain short-range order during irradiation have been extended to include effects of simultaneously injected helium, but still no swelling could be detected. A theory of point defect trapping at incoherent and semicoherent θ' interfaces has been applied to swelling in Al–4% Cu alloys during neutron irradiation. The model predicts an extension of the time for the onset of swelling and end-of-irradiation swelling values that agree with experimental results. Microstructural studies of neutron damage in molybdenum, zirconium, and zirconium alloys are presented. Only dislocation loops, a substantial fraction of which are of vacancy character, are found in zirconium and its alloys. The suggestion is offered that the preferential attraction of the loops for interstitials is very weak. Microstructural features have been related to tensile properties for highly irradiated 1100-0 and 6061 aluminum

alloys. Initial results of the ORNL light-ion irradiation creep facility are presented and shown to be consistent with other observations. Other applications of the facility are described. Specimen thickness in the range 25–200 μm has been shown to have no influence on thermal creep rate.

Advances in the development of our capability in electron microscopy are described, including design of a double focusing magnetic sector electron energy loss spectrometer for the analytical electron microscopes, software and hardware modifications to expand the capability of the PDP 11/34 computer system, acquisition of specialized tilting, heating, and straining holders for the 1-MV electron microscope, and modifications to the 1-MV microscope for energy-dispersive x-ray analysis. In the area of electron microscopy research a systematic study of contamination processes occurring in high-current-density electron probes is presented along with instrument modifications to restrict the problem. The procedure for obtaining small-angle electron scattering patterns in the electron microscope is described and applied to the study of Hf-O clusters in an oxidized Ta–8% W–2% Hf alloy. Weak-beam dark-field imaging has been used to reveal fine details of structural changes introduced by neutron irradiation of Al–4% Cu alloys. Calculations have suggested that the peak-to-background ratio for microanalysis by x-ray emission in TEM is reduced for increased accelerating voltage. An experiment to demonstrate this has been undertaken. Moiré patterns and micro-micro diffraction techniques have been used to identify positively Li_2O precipitate in Li-doped MgO. Improvements to the dual Van de Graaff irradiation facility are described.

The nuclear microanalysis facility has been used to identify sodium tetraborate as the source of oxygen during the anodization of vanadium. The depth distribution of injected deuterium and helium has been measured as a function of implantation energy pattern, injection temperature, and subsequent nickel ion bombardment. The center of the distributions remains constant, but the distribution broadens as the injection temperature increases or nickel ion bombardment proceeds.

5. ENGINEERING MATERIALS SCIENCE

5.1 Fundamentals of Welding and Joining

Ferrite observed at room temperature in type 308 stainless steel weld metal is the untransformed δ-ferrite that formed during initial stages of solidificaiton. A study of solidification of model austenitic systems has begun. Formation of sigma phase can be prevented in welds by controlling the chromium equivalent. Laves and chi phases can be prevented by controlling the molybdenum content. Careful control of the solubility product, [C][Ti], is necessary in titanium-modified steels to prevent formation of stringers. Measured x-ray intensities of $M_{23}C_6$ do not appear to follow their predicted values. A new precipitate seen in type 321 stainless steel aged 17 years at 650°C is similar to Fe_2P and $(Fe,Cr)_2As$. A similar phase has been seen in irradiated steels. Carbon precipitates on quenching Ni-C alloys; interpretation of internal friction

measurements therefore needs revision. Thermodynamics of the fcc Fe-C system are re-analyzed; the activity coefficient of carbon in nickel was measured.

1. STRUCTURE OF MATERIALS

1.1 THEORETICAL RESEARCH — J. S. Faulkner

We are developing a fundamental theoretical framework for condensed matter that makes it possible to synthesize the diversity of observed phenomena into a single internally consistent picture. The purpose of this development is to facilitate studies and applications in materials science. We used band-theory techniques based on multiple-scattering theory (MST) and the discrete variational method (DVM) to study the relation between the electronic states in crystals and their binding energy, physical properties, and superconducting properties. The full muffin-tin coherent potential approximation (CPA) is used for similar studies on random substitutional solid solutions and nonstoichiometric compounds. The physical and chemical properties of surfaces interacting with their environments are studied with layer and cluster techniques based on both MST and DVM. Lattice defect theory is used to develop an understanding of radiation effects and mechanical properties of solids.

1.1.1 Electron-Phonon Contribution to the Phonon Linewidth in Nb: Theory and Experiment[1,2] — W. H. Butler, H. G. Smith,[3] and N. Wakabayashi[3]

Phonons have a finite lifetime and a nonzero energy width due to the electron-phonon interaction. In this paper we present theoretical calculations and experimental measurements of this line width for Nb. The calculations employ the rigid muffin-tin approximation and a realistic band structure. The measurements were done at low temperature to minimize the contributions to the line width from phonon-phonon interactions. The calculations predict and experiments confirm strong electron-phonon coupling for the longitudinal phonon modes in the [110] direction.

---

[1]Summary of *Phys. Rev. Lett.* 39: 1004 (1977).

[2]This work has been singled out in the American Institute of Physics publication *Physics News in 1977* as being unusually interesting and newsworthy.

[3]Solid State Division.

BLANK PAGE

1.1.2 Electron-Phonon Interaction and Lattice Thermal Conductivity[4] — W. H. Butler and R. K. Williams

Phonons in a metal have a finite lifetime due to the emission of electron-hole pairs. This process leads to an electron-phonon contribution, W_{ep}, to the thermal resistance, which limits the lattice thermal conductivity, λ_p. We summarize the available experimental data on W_{ep}, emphasizing uncertainties and contrasting results from different types of experiments. Methods for obtaining better data are suggested. The available data are in fair agreement with a simple theoretical estimate:

$$\lim(T \to 0) W_{ep}^{p}(T/\theta_D)^2 = 0.21\Omega_a^{1/3} N\Lambda(\text{deg cm/watt}) ,$$

where Ω_a is the atomic volume in Å^3, N is the Fermi energy density of states (1 spin) in states/eV, and Λ is the electron-phonon mass enhancement. The deviations from this limiting formula may prove useful for understanding the electron-phonon interaction.

1.1.3 Calculation of Resistivity and Electron-Phonon Coupling in Pd[5,6] — F. J. Pinski,[7] P. B. Allen,[7] and W. H. Butler

We have calculated electron-phonon properties of palladium using KKR energy bands and wave functions and the rigid muffin-tin electron-phonon scattering operator. The mass enhancement parameter λ is small, 0.29, suggesting that spin fluctuations enter in the renormalized electronic specific heat. However, rather little contribution from spin fluctuations is necessary to account for either the large magnitude of electrical resistivity or the absence of superconductivity. The high-temperature resistivity departs strongly from linearity in T. Mott attributed this to Fermi smearing, but previous Fermi smearing calculations are not convincing. The room-temperature mean free path is 3.3 nm,

---

[4]Abstract of a paper submitted to *Physical Review*.

[5]Abstract of a talk presented at the American Physical Society meeting in Washington, D.C., March 27–30, 1978.

[6]Supported in part by NSF Grant DMR76-82946.

[7]Department of Physics, State University of New York, Stony Brook.

which suggests that "saturation" should be beginning by 1000 K. Using a simple phenomenological treatment of saturation, we propose that the observed low-temperature T^2 resistivity[8] of magnitude 0.31 pΩ m/K^2 persists up to very high temperature but is hidden by saturation.

1.1.4 Electron-Phonon Contribution to Electrical Resistivity and Superconducting "*P*-Wave" Transition Temperature of Pd[9] — F. J. Pinski,[7] P. B. Allen,[7] and W. H. Butler

We present first-principles calculations of the electron-phonon parameters that govern transport and superconductivity in palladium. Our calculated resistivity is in good agreement with experiment. The "*s*-wave" coupling constant (or mass enhancement) is 0.41 and the "*p*-wave" coupling constant is −0.02, making the existence of observable electron-phonon induced "*p*-wave" pairing in palladium very doubtful.

1.1.5 A Complete Solution of the KKR-CPA Equations: Cu-Ni Alloys[9] — G. M. Stocks, W. M. Temmerman,[10] and B. L. Gyorffy[10,11]

We report on calculations of the electronic states in disordered Cu_cNi_{1-c} alloys based on a complete solution of the coherent potential approximation for a muffin-tin model of the alloy potential (KKR-CPA). The computational effort required is modest on the scale of that involved in multi-atom-per-unit-cell band structure calculations. The calculated densities of states agree well with the results of photoemission and other experiments. The adequacy of previous approximate KKR-CPA and averaged *t*-matrix calculations is discussed.

1.1.6 The Atomic Sphere Approximation to the KKR-CPA: Electronic Structure of Paramagnetic Cu_cNi_{1-c} Alloys[4] — W. M. Temmerman,[10] B. L. Gyorffy,[10,11] and G. M. Stocks

We considered the Coherent Potential Approximation (CPA) for a substitutionally disordered alloy crystal potential of the nonoverlapping muffin-tin form. We simplified the KKR-CPA theory using the

---

[8] J. T. Schriempf, *Phys. Rev. Lett.* 20: 1034-35 (1968).
[9] Abstract of a paper submitted to *Physical Review Letters*.
[10] H. H. Wills Physics Laboratory, University of Bristol, U.K.
[11] Present address, Brookhaven National Laboratory, Upton, New York.

Atomic Sphere Approximation (ASA) of Andersen. In its new form the fundamental equations of the theory can be solved numerically. The computational effort necessary is not particularly large on the scale of modern band structure calculations. As an illustration of our method, we calculated the Bloch spectral functions and the partially averaged local density of states for a number of alloy potentials designed to represent paramagnetic Cu_cNi_{1-c} alloys. Where comparison was possible we found good agreement with previous calculations. Our results are also consistent with various experimental data.

1.1.7 Cluster Calculation of the Electronic Structure of Oxygen Chemisorbed on the Aluminum (111) Surface[5] — G. M. Stocks and G. S. Painter

In recent years, considerable interest has been focused on characterizing the interaction of oxygen with aluminum surfaces. Recent experimental data suggest the existence of a chemisorbed state on the (111) surface. Here we report results from a first-principles linear variational calculation for a cluster representation of oxygen on the (111) aluminum surface. Features of the electronic structure are related to experimentally determined spectral structures. The wave function components are analyzed to provide information about chemisorptive bonding in this system.

1.1.8 Surface Electronic Structure of Cu-Ni Alloys in a Thin Film Model[5] — G. S. Painter and G. M. Stocks

Copper-nickel alloys are among the most widely studied and best characterized of alloys in terms of the bulk electronic structure, but relatively little is understood about the surface electronic structure. We report here some calculations for thin-film representations of the Cu-Ni surface. Various features of the surface film electronic structure are compared with corresponding ones of the bulk, as determined from calculations carried out in the coherent potential approximation. These results are used to discuss the bonding properties of the Cu-Ni alloy surface. The usefulness of bulk alloy properties for discussion of surface characteristics is assessed.

1.1.9 Theoretical Studies of the Electronic Structure and Bonding Properties of Stepped Metal Surfaces[12] — G. S. Painter

It is widely recognized that structure sensitivity of surface processes is a reflection of the electronic structure of the surface and is thus coupled to the geometrical arrangement of surface atoms. The interactions that take place between the surface and an adsorbate species depend upon the bonding among the atoms of the surface, and this in turn is determined by the structural arrangement of the surface atoms. Surface irregularities that alter the coordination number of a surface atom are particularly effective in altering the bonding properties of that atom. Theoretical electronic structure calculations for models chosen to represent features of stepped surfaces are summarized in this presentation. Emphasis is placed on the changes in the local densities of states and the surface orbitals induced by the presence of the steps. The results also indicate how electron distributions in small atomic clusters differ from those in the atom and the solid.

1.1.10 Bonding of Oxygen on Aluminum: Relation Between Energy-Band and Cluster Models[13] — G. S. Painter

A study of some factors that influence the position and shape of the resonance bands of adsorbates on surfaces is presented with emphasis upon the case of oxygen chemisorbed on aluminum. A twofold approach has been taken to determine the relative roles of local and delocalized electron effects: the energy-band structure for a thin-film geometry is correlated with the eigenvalue spectrum from a "surface-molecule" cluster model. Oxygen resonance features are found to depend mainly upon a bond mechanism involving orbitals directed parallel to the surface such that the local bonding in the cluster model provides a reasonable description of the resonance position. Delocalization of the substrate electrons in the plane is found to provide a bulklike background against which the localized resonance is observed.

---

[12]Abstract of an invited paper presented at the Materials Research Society Symposium on Catalysis and Catalytic Materials, Boston, Mass., Nov. 14–16, 1977.

[13]Abstract of *Phys. Rev. B* 17: 662–71 (1978).

1.1.11 Bonding in a Cu (001) Monolayer[4] — G. S. Painter

Results of a first-principles, all-numerical linear variational energy band calculation are presented for a Cu (001) monolayer. The electronic structure is discussed in terms of the changes in d-bonding that accompany the descent in symmetry in going from the bulk to the surface. The relation of the splittings and ordering of the levels to those of the bulk follow expectations based on simple d-bonding considerations. Results are compared with those from other studies, and some discrepancies among earlier works are resolved.

1.1.12 Level Ordering of States in a Cu (001) Monolayer[4] — G. S. Painter

In presenting their layer multiple-scattering approach to the energy band problem for thin films, Kar and Soven reported that the ordering of levels in their calculation for a copper monolayer differed from previous results obtained by Kasowski. Some question also arose in relating the d-level splittings at the surface to the orders of the bulk E_g and T_{2g} levels. This comment suggests that these discrepancies arise from an inconsistency in coordinate systems used by Kar and Soven. It is shown that within a consistent system, the level splittings and orderings in Kar and Soven's results follow expectations based on simple bonding considerations. The resulting good agreement with other works supports the essential accuracy of the multiple scattering approach of Kar and Soven.

1.1.13 Theoretical Models of the Electronic Structure and Bonding Interactions at Surface Irregularities[14] — G. S. Painter

The main purpose of this paper is to present some results of theoretical calculations of the electronic structure of metal atomic clusters and thin films chosen to represent surface irregularities, to show how features differ from corresponding ones of the bulk and perfect surface, and to offer suggestions as to why these differences occur. There are a number of electronic characteristics of ultrasmall ($\sim$1 nm) crystallites and surface structural irregularities (steps, kinks, etc.)

---

[14]Abstract of paper to appear in *Materials Research Bulletin*.

that differ remarkably from those of the perfect surface. This paper will emphasize features that appear to be general rather than specific to the case considered.

1.1.14 A Generalized Model of Void Swelling — The Depth-Dependent Swelling by Self-Ion Irradiation[15] — M. H. Yoo

The depth dependence of void swelling in self-ion-irradiated pure metals has been investigated by using the general rate theory model of void swelling[16] that includes the effects of displacement cascades and deposited self-ions. Three major physical sources of the depth-dependent void swelling are identified as the free surface, the displacement damage, and the deposited self-ions. Example calculations for nickel self-ion damage with ion energy in MeV range show that the deposited self-ions produce a substantial perturbation on the swelling profile expected on the basis of the damage profile alone, and that the surface effect on void swelling is relatively small. The significance of the calculated results is discussed in view of the development of simulation experimental techniques.

1.1.15 Growth Kinetics and "Preference Factor" of Frank Loops in Nickel During Electron Irradiation[17] — M. H. Yoo and J. O. Stiegler

The growth kinetics of interstitial type Frank loops in a thin foil of high purity Ni at 450°C was measured during electron irradiation in an HVEM operating at 650 kV. The depth positions of the loops with respect to the foil surfaces were determined by stereomicroscopy. The experimental data were analyzed by use of the general rate theory model[16] that takes into account both temporal and spatial dependence of loop growth. It is found from systematic variations of the vacancy migration energy, E_v^m, and the preference factor of dislocation loops for self-interstitials, δ_i, that E_v^m = 1.2 eV and δ_i = 0.06 together yield reasonable agreement between the theoretical model and the experimental data.

---

[15] Abstract of paper submitted to *Journal of Nuclear Materials*.

[16] M. H. Yoo, "Dislocation Loop Growth and Void Swelling in Bonded Media by Charged Particle Damage," *J. Nucl. Mater.* 68: 193–204 (1977).

[17] Abstract of *Philos. Mag.* 36: 1305–15 (1977).

1.1.16 Nucleation and Growth of Interstitial Dislocation Loops in Irradiated Foils[18] — M. H. Yoo

A unified rate theory model of the homogeneous nucleation of interstitial dislocation loops and their subsequent growth under irradiation is formulated. It is assumed that self-interstitials, vacancies, and divacancies are mobile, and di-interstitials and interstitial clusters of higher hierarchy are all immobile. The reaction rate constants for the defect clusters are prescribed in terms of the effective capture radii. After a characteristic nucleation time, which depends on dose rate, temperature, foil thickness, and sink strength, the loop growth is treated by the previously proposed growth model (Sect. 1.1.15). The calculated results of nucleation kinetics on point defects and their clusters are directly applied as the initial conditions for the growth calculation. Example calculations for Al and Ni foils irradiated in a high-voltage electron microscope are discussed.

1.1.17 Slip, Twinning, and Fracture in Hexagonal Close-Packed Crystals[19] — M. H. Yoo

The role of deformation twinning in the crack initiation of hcp crystals is investigated by theoretically analyzing various possible slip-twin and twin-twin interactions. For 16 elemental metals, operative deformation modes of slip and twin systems are predicted on the basis of crystallographic and elastic properties of dislocations. Cleavage habit planes are predicted by considering both the anisotropic elastic energies of slit cracks and the interatomic forces estimated from the elastic constants. For the most feasible combinations of slip-twin and twin-twin interactions, the possibility of nucleating either a new twin or a crack is examined in terms of the orientation-dependent stress concentration factors. The calculated results are compared with the reported experimental data and discussed in view of the fracture strength and ductility of polycrystalline hexagonal metals.

---

[18]Abstract of talk given at Irradiation Effects Session of 107th AIME Annual Meeting, Denver, Colorado, February 26–March 2, 1978.

[19]Abstract of an invited talk to be given at a special session on "The Role of Twinning in Fracture of Metals and Alloys," the Fall Meeting of AIME, St. Louis, Mo., Oct. 15–19, 1978.

1.1.18 Electronic States in Metals and Alloys[20] — J. S. Faulkner

Techniques for calculating the electronic states in condensed matter have developed so rapidly in recent years that statements concerning what can or cannot be achieved may well be out of date shortly after they are made.

One of the most exciting recent achievements in this area is the development of computational techniques for carrying out full muffin-tin coherent-potential-approximation (CPA) calculations of the electronic states of substitutional solid solutions by Malcolm Stocks. This is the culmination of the efforts of many people at Oak Ridge and the University of Bristol in England.

The purpose of this talk is to discuss the relationship between this and other recent developments to transformations and phase stability in real alloy systems. From phase diagrams the materials scientist can obtain useful insights into the macroscopic properties of alloys. I will discuss some ways in which the wealth of detail in the modern calculations can be used to get even more information about such properties.

1.1.19 Scattering Theory and Cluster Calculations[21] — J. S. Faulkner

It is shown that a formula due to Lloyd for the density of states of a cluster of muffin-tin potentials can be derived very easily from a theorem in formal scattering theory that was proved by Krein. Some questions in the usual interpretation of the formulae are discussed in the light of Krein's theorem and also the time-delay operator. Generalized Jost functions are introduced and used to furnish a picture of the limiting process in various kinds of cluster calculations.

1.1.20 Krein's Theorem and Cluster Calculations[5] — J. S. Faulkner

A theorem due to M. G. Krein[22] is shown to provide a mathematically rigorous derivation of Lloyd's formula for the density of states

---

[20]Abstract of paper presented at TMS(AIME) Alloy Phase Stability Seminar, Chicago, Oct. 26, 1977.

[21]Abstract of *J. Phys.* C 10: 4661 (1977).

[22]M. G. Krein, "O Formule Sledov v Teorii Vozmushchenii," *Mat. Sb.* 33: 597–626 (1953).

of a cluster of scatterers. Other aspects of this problem are discussed in the light of this derivation.

1.1.21 Coherent Potential Approximation Calculation[5] for PdH_x —

D. A. Papaconstantopoulos,[23] B. M. Klein,[23] L. L. Boyer,[23] and J. S. Faulkner

The angular momentum components of the density of states (DOS) for sub-stoichiometric PdH_x were calculated by the coherent potential approximation (CPA). A tight binding form[24] of the CPA, based on an improved Slater-Koster fit to first principles APW calculations,[25] was used. The CPA DOSs have been used to calculate the electron-phonon interaction as a function of hydrogen concentration x. The results are in good agreement with experiment and consistently verify previous calculations,[25] in which the rigid band model was used. In addition, the coefficient of the electronic specific heat, γ, was calculated as a function of x and agreed well with experiment.[26]

1.2 X-RAY DIFFRACTION RESEARCH — H. L. Yakel

Although experiments to detect superheavy elements with energy-tuned synchrotron radiation as the source of excitation for x-ray fluorescence gave negative results, the techniques developed dramatically improved the sensitivity of fluorescence analyses. Additional applications of synchrotron radiation in materials science research are proposed.

---

[23]Naval Research Laboratory, Washington, D.C.

[24]J. S. Faulkner, "Electronic States of Sub-Stoichiometric Compounds and Application to Palladium Hydride," *Phys. Rev. B* 13: 2391–97 (1976).

[25]D. A. Papaconstantopoulos et al., "Band Structure and Superconductivity of PdD_x and PdH_x," *Phys. Rev. B* 17: 141–50 (1978).

[26]C. A. Mackliet, D. J. Gillespie, and A. I. Schindler, "Specific Heat, Electrical Resistance, and Other Properties of Superconducting Pd-H Alloys," *J. Phys. Chem. Solids* 37: 379–88 (1976); G. Wolf, M. Zimmermann, and K. Bohmhammel, "The Molar Heat Capacity of Non-Superconducting PdH_x in the Temperature Range from 2 to 7 K," *Phys. Status Solidi* (a) 37: 179–82 (1976).

The structure of a monoclinic europia crystal, protected from the atmosphere, has been refined from an extensive x-ray diffraction intensity data set. These data are being used to test methods for estimating secondary extinction effects, with both the Zachariasen approximation and an exact solution of the Darwin transfer equations. The latter approach has been facilitated by development of computational techniques whereby the exact solution may be applied to real crystal shapes.

Progress in small-angle x-ray scattering research on coals, polymers, and irradiated metal is reported. The ability of the 10-m scattering instrument to measure anisotropic scattering at high data acquisition rates proved crucial in experiments on polymer crystallization. Studies of vitrinites from high-volatile bituminous coals gave quantitative descriptions of the distribution of micropores, mesopores, and microminerals in these materials. Experiments with irradiated molybdenum suggest the importance of scattering from small irradiation-induced dislocation loops in the overall scattering pattern.

1.2.1 The Crystal Structure of Monoclinic Europium Sesquioxide — H. L. Yakel

An untwinned monoclinic europium sesquioxide crystal with little mosaic spread was obtained from NaF-grown material that had been kept in a helium-filled dry box. The crystal was inserted into a glass capillary, which was then sealed in the dry box. With an automated diffractometer (Mo Kα x radiation) in a $\theta - 2\theta$ scan mode 7000 individual x-ray diffraction data were collected from this crystal. Precise lattice constants were measured with data to scattering angles of 163°; these are listed in Table 1.1. Recorded data were corrected for Lorentz, polarization, and photoelectric absorption effects. At a later stage in the analysis, effects due to secondary extinction were also estimated. Full-matrix linear least-squares calculations, based on a structure derived[27] for Sm_2O_3, confirmed the essential outlines of the model. Preliminary atomic position coordinates for monoclinic

[27] D. T. Cromer, "The Crystal Structure of Monoclinic Sm_2O_3," *J. Phys. Chem.* 61: 753–55 (1957).

Table 1.1. Lattice Parameters of Monoclinic Europium Sesquioxide

Quantity	Value
a_0, nm	1.41105(2)
b_0, nm	0.36021(1)
c_0, nm	0.88080(2)
ß, deg	100.037(1)
V, nm^3	0.44084(3)
Space group	$C2/m$, $C2$, or Cm
(Eu_2O_3)/cell	6
X-ray density, Mg/m^3	7.9536(5)

europia are given in Table 1.2. Some modest improvements in the customary measures of agreement between observed and computed structure factors were obtained when the refinements were carried out in the noncentric space groups $C2$ or Cm rather than $C2/m$.

Diffraction data from this well-formed crystal would seem to provide a useful test for current theories and practices of extinction correction. To date, our calculations have shown that: (1) least squares refinements of the basic diffraction data alone, based on Zachariasen's treatment of extinction[28] as extended by Coppens and Hamilton,[29] lead to a statistically preferred extinction model that is difficult to reconcile with physical reality; (2) intensities measured at several angles of rotation about the diffraction vector of an extinction-affected reflection vary in a manner that agrees with the more physically sensible extinction model; and (3) while either model

[28]W. H. Zachariasen, "A General Theory of X-Ray Diffraction in Crystals," *Acta Crystallogr.* 23: 558–64 (1967).

[29]P. Coppens and W. C. Hamilton, "Anisotropic Extinction Corrections in the Zachariasen Approximation," *Acta Crystallogr.* A26: 71–83 (1970).

Table 1.2. Preliminary Atomic Position Coordinates for Monoclinic Eu_2O_3[a]

Atom	Coordinate		
	x	y	z
Eu(1)	0.13470(1)	0.5	0.48971(2)
Eu(2)	0.18972(1)	0.5	0.13761(2)
Eu(3)	0.46636(1)	0.5	0.18962(2)
O(1)	0.1291(2)	0.0	0.2856(3)
O(2)	0.3248(2)	0.5	0.0269(3)
O(3)	0.2963(3)	0.5	0.3733(4)
O(4)	0.4735(2)	0.0	0.3433(3)
O(5)	0.0	0.5	0.0

[a]Refinements based on space group $C2/m$.

for extinction must improve the fit between observations and calculations, neither should be trusted to reflect real features of the crystal.

1.2.2 The Stability of the Room-Temperature Structure of Monoclinic Eu_2O_3 — H. L. Yakel

Previously reported observations have indicated that crystals of monoclinic europia may interact with a normal atmospheric component (probably water) to produce a small triclinic distortion of the lattice. The protected monoclinic europia crystal, from which extensive diffraction data have been collected, will be deliberately exposed to water vapor in an effort to confirm this change.

Confusion concerning the thermodynamically stable form of Eu_2O_3 at room temperature may be connected with the extent to which the material has reacted with its environment. We have reported high-temperature x-ray diffraction experiments with unprotected monoclinic

material in which about half of the diffraction specimen was irreversibly converted to the cubic modification between 500 and 800°C. Similar experiments with protected monoclinic Eu_2O_3 showed no significant conversion in the same temperature range. These results suggest that the stable form of Eu_2O_3 at room temperature is monoclinic and, further, that reaction, probably with water vapor, may facilitate a thermally activated transformation to the cubic form.

1.2.3 A Refinement of the Crystal Structure of Orthorhombic Zinc Chloride[30] — H. L. Yakel and J. Brynestad[31]

The structure of orthorhombic zinc chloride has been refined by least squares calculations based on single-crystal x-ray diffraction data. All features of the preliminary model were confirmed; the tetrahedral environment of zinc ions is quite regular, with Zn–Cl distances varying about 0.227 nm by no more than 1 pm and Cl–Zn–Cl angles departing from the ideal tetrahedral angle by no more than 2°.

1.2.4 The Correction of Integrated Intensity Measurements for Secondary Extinction — B. S. Borie

To reduce measurements of diffraction maximum integrated intensities to experimental values of the structure factors, one must understand and correct for the phenomenon of extinction. Secondary extinction, characteristic of crystals of moderate perfection, accounts for this effect in most crystals. The pair of coupled partial differential equations that govern the intensity distributions due to secondary extinction within a crystal have recently been solved without approximation by Werner.[32] We are concerned with the systematic application of this solution to diffraction data in ways sufficiently simple that they may be incorporated in standard computer reductions.

We have established criteria for the subdivision of a crystal cross section into regions such that particular forms of the Werner solution

---

[30]Abstract of note submitted for publication to *Inorganic Chemistry*.

[31]Chemistry Division.

[32]S. A. Werner, "Extinction in Mosaic Crystals," *J. Appl. Phys.* 45: 3246–54 (1974).

obtain in each region. We have shown how boundary conditions appropriate for a region may be used to find integration constants appearing in the solution. We have shown how these boundary conditions propagate from region to region across the crystal. We are able to calculate intensity distributions within a crystal as a function of a single dimensionless extinction parameter — the ratio of the scattering strength to the absorption coefficient. We have applied these results to a crystal of simple square cross section.

We are currently attempting to find a rigorous extinction correction for cylindrical and spherical crystals. We are also trying to correct for secondary extinction a recently gathered set of integrated intensity measurements for europia.

1.2.5 Synchrotron Radiation as an Excitation Source for X-Ray Fluorescence Analysis[33] — C. J. Sparks, Jr., Enzo Ricci,[34] M. O. Krause,[31] S. Raman,[35] R. V. Gentry,[36] H. L. Yakel, and J. B. Hastings[37]

Electrons circulating in storage rings provide an intense photon flux, which was used as an excitation source for multielement x-ray fluorescence analysis (XRF). This experiment was conducted at the Stanford Synchrotron Radiation Laboratory to measure the concentration that could be detected with the unique properties of synchrotron radiation. Compared with conventional x-ray sources, synchrotron radiation is much more intense, highly collimated, nearly linearly polarized, and pulsed. Both the continuous photon spectrum and that monochromated with a curved graphite crystal (followed by collimation) to produce a focused beam of about-37-keV x rays containing $\sim 7 \pm 10^{10}$ photons/s in an area 0.45 by 1 mm were used to excite the fluorescence spectrum. This exceeded the intensity from conventional

---

[33]Abstract of a paper given at the 26th Annual Denver X-Ray Conference on Applications of X-Ray Analysis, Aug. 3–5, 1977, Denver, Colo.

[34]Analytical Chemistry Division.

[35]Physics Division.

[36]Visiting scientist from Columbia Union College, Takoma Park, Md.

[37]Present address, Brookhaven National Laboratory, Upton, N.Y.

1.5-kW x-ray sources by a factor of 300. Various samples and NBS reference standards were analyzed and the results compared with proton and conventional x-ray source excited fluorescence analysis. Detection limits for several elements were determined to be in the range of 1 pg (10^{-12} g), with concentration limits of about 10 parts per billion by weight (ppb). An outstanding advantage of synchrotron radiation is the improved sensitivity for small samples and for macroanalysis compared with conventional x-ray sources and a thousandfold reduction in the heat dissipated in the samples for similar detection limits with proton-excited XRF(PIXE). Synchrotron radiation for XRF analysis will permit detection limits to 10 fg (10^{-14} g) and concentration limits to less than a ppb with improved instrumentation for recording the fluorescent signal.

A scanning x-ray microprobe based on the small source size and the intensity of synchrotron radiation will give concentration limits that are 10^{-4} those achieved with electron microprobes. Elemental distributions in materials, environmental, and biological samples can be determined with spatial resolution below a few micrometers.

1.2.6 Evidence Against Superheavy Elements in Giant-Halo Inclusions Re-Examined with Synchrotron Radiation[38] — C. J. Sparks, Jr. S. Raman,[35] E. Ricci,[34] R. V. Gentry,[36] and M. O. Krause[31]

The giant-halo inclusion 19D reported to show the strongest evidence for superheavy elements on the basis of proton-induced x-ray fluorescence has been re-examined with ≈55 times greater sensitivity by employing synchrotron radiation as the exciting source. It is shown conclusively that at concentration levels of ≈5 x 10^8 atoms per inclusion, superheavy elements are not present in GH19D or in numerous other giant-halo inclusions studied.

The detection of characteristic x rays is one of the best methods for identifying the atomic number (Z) of a new element. Proton-induced x-ray emission (PIXE) techniques were employed recently by Gentry et al.[39]

---

[38]Abstract of *Phys. Rev. Lett.* 40: 507–11 (1978).

[39]R. V. Gentry et al., "Evidence for Primordial Superheavy Elements," *Phys. Rev. Lett.* 37: 11–15 (1976).

at the Florida State University (FSU) tandem Van de Graaff accelerator to obtain evidence for the possible presence of superheavy elements (SHE) in giant-halo (GH) monazite inclusions. Spurred by this report, which if found correct would have important experimental and theoretical consequences, several searches have been undertaken, all with negative results. The many samples searched were chosen because of their similarity to those examined previously, but none were giant-halo inclusions. Therefore, it was desirable to examine the original GH inclusions 15, 19A, and 19D in order to remove any vestigial doubts. Unfortunately, GH15 was lost in sample transfer at FSU, and GH19A was lost through overheating at Harwell, leaving only GH19D for confirmation attempts. In the present Letter, we describe an improved experiment at SSRP, in which we studied 19D and numerous other GH samples with record levels of sensitivity, again with negative results for the presence of SHE. In particular, no evidence for SHE ($Z = 126$) was found at a sensitivity level 50 to 100 times better than the evidence reported from proton excitation.

1.2.7 X-Ray Cross Sections for Microanalytical Detection Limits[40] — C. J. Sparks, Jr.

X-ray diffraction and fluorescence detection of small amounts of matter depends on the various cross sections for x-ray interactions. As cross sections for various x-ray interactions have been tabulated and source strengths for x-ray tubes are generally known, we can readily calculate the signal from the diffracted and fluorescent intensities. We combine this information with the characteristics of the experimental arrangement (the kind of sample, x-ray flux, backgrounds, detector efficiencies, and x-ray energy resolution of the experiment) to arrive at the lower weight limits for the determination of the structure and elemental composition of small single crystals, polycrystals, second phases embedded in a matrix, and surface films.

It is shown that background radiation generally becomes the ultimate limitation to the amount of material that can be detected. Compton

[40]Abstract of an invited paper given at the American Crystallographic Association meeting March 19–24, 1978, University of Oklahoma, Norman.

and thermal diffuse scatter are major contributions to the backgrounds beneath diffraction signals for polycrystalline samples, whereas the incident x-ray flux determines the detectable limit for single crystals. Bremsstrahlung generated in the sample by photoejected electrons is an important background beneath fluorescent lines. With conventional x-ray sources, diffraction patterns can be measured for single crystals less than 1 μm diam and weighing a few picograms. A few micrograms of polycrystalline sample would be required for detection by diffraction. Fluorescent detection limits are about 10 pg at concentrations of 10^{-7} (weight). Position-sensitive detectors and 2π detectors for measuring complete Debye diffraction rings can speed the data collection. Powerful x-ray sources such as synchrotron radiation can push the detection limits still lower.

1.2.8 Calculation of X-Ray Fluorescence Cross Sections for K and L Shells[41] — M. O. Krause,[31] E. Ricci,[34] C. J. Sparks, Jr., and C. W. Nestor, Jr.[42]

Exact expressions are given for the K and L x-ray fluorescence cross sections. Hole transfer between the L subshells is considered and leads to a substantial enhancement of the cross sections for x rays of the L2 and L3 emission series. Absolute values of Kα and Lα cross sections are calculated for all elements and four excitation energies, namely Ge K $\hat{=}$ 10.0 keV, Mo Kα $\hat{=}$ 17.44 keV, Ag K $\hat{=}$ 22.5 keV, and ^{241}Am $\hat{=}$ 59.6 keV.

With currently available values for subshell photoionization cross sections, x-ray emission rates, fluorescence yields, and Coster-Kronig yields, it is now possible to calculate K and L x-ray fluorescence cross section values with sufficient accuracy to serve the many areas in which photo-excited characteristic x rays play a role.

---

[41] Abstract of *Adv. X-Ray Anal.* 21: 119–27 (1978).
[42] Computer Sciences Division.

1.2.9 Uses of Synchrotron Radiation for Materials Science Research[43] — C. J. Sparks, Jr.

X rays are a widely applied probe for determining the structure of materials to lead to a better understanding of their physical and chemical properties. An x-ray source 10^3-10^4 times more intense than conventional sources permits major advances in materials science research thought impossible a few years ago. This intense x-ray source is generated by electrons circulating in synchrotrons or storage rings. In addition to the intensity, the synchrotron radiation has other advantages compared with conventional sources: it is pulsed, linearly polarized, and highly collimated in a plane, and it has a broad energy spectrum (1 eV–50 keV). Although the intense synchrotron-produced x-ray source is just beginning to be available for research, several promising applications have been made to materials science.

X rays interact with matter either by scattering, which gives information on the structural arrangements of the atoms and/or molecules, or by photo-ejecting electrons, which provides the basis for photoelectron, Auger, and x-ray spectroscopy of materials. Thus, many experimental techniques will benefit from providing new structural and analytical information on more dilute systems, including studies of time-dependent phase transformation, surfaces, defect structures, and localized atomic arrangements in matter.

Advances in our understanding of catalysis, amorphous and liquid matter, and atomic environments of atoms have already emerged from studies of the x-ray absorption edges of elements in alloys and compounds. The improved signal-to-noise ratios achieved by ejecting electrons with x-rays instead of electrons have permitted more detailed study of materials surfaces.

---

[43]Abstract of an invited paper at 1977 Fall Meeting of TMS-AIME, Oct. 23-27, 1977, Chicago.

1.2.10 Recent Developments in X-Ray and Neutron Small-Angle Scattering Instrumentation and Data Analysis[44] — J. Schelten[45] and R. W. Hendricks

The developments in instrumentation and data analysis that have occurred in the field of small-angle x-ray and neutron scattering since 1973 are reviewed. For x rays, the cone camera collimation system was invented, synchrotrons and storage rings were demonstrated to be intense sources of x radiation, and one- and two-dimensional position-sensitive detectors were interfaced to cameras with both point and line collimation. For neutrons, the collimators and detectors on the Jülich and Grenoble machines were improved, new D-11 type instruments were built or are under construction at several sites, double-crystal instruments were set up, and various new machines have been proposed. Significant progress in data anlaysis and evaluation has been made through application of mathematical techniques such as the use of spline functions, error minimization with constraints, and linear programming. Several unusual special experiments — which involve the anisotropy of the scattering pattern, gravitational effects, moving scatterers, and fast time-slicing dynamic experiments — are discussed.

1.2.11 The ORNL 10-m Small-Angle X-Ray Scattering Camera 9. — Camera Control Programs[46] — R. W. Hendricks

Program SAX and its associated programs OVF and MOT are high-priority, prequeued nonresident foreground tasks, which run under the MODCOMP II MAX III operating system to provide complete user control of the ORNL 10-m small-angle x-ray scattering camera.

---

[44]Accepted for publication in *Journal of Applied Crystallography*.

[45]Institut für Festkörperforschung der Kernforschungsanlage, 517 Jülich, West Germany.

[46]Abstract of ORNL/TM-6342, vol. 9, in press.

1.2.12 Microporosity and Micromineralogy of Vitrinite in a Bituminous Coal[47] — J. S. Lin, R. W. Hendricks, L. A. Harris, and C. S. Yust

Small-angle x-ray scattering (SAXS) and transmission electron microscopy (TEM) have been used to study the microporosity and micromineralogy of vitrinite in a high-volatile bituminous coal (Illinois No. 6). Micropores and fine minerals with sizes ranging between 1 and 100 nm were observed. The minerals, primarily silicates, were heterogeneously distributed in layers parallel to the bedding plane of the coal. The radii of gyration, surface area, volume fraction, and size distribution of micropores, mesopores, and fine-size minerals were obtained from an analysis of the SAXS curves. The total volume fraction of these components was determined from the integrated intensity to be 0.09 ± 0.02. The size distributions were found to be trimodal with peaks at 3.0, 10, and 22 nm. These peaks are associated with micropores, microminerals, and mesopores, respectively. The specific surfaces associated with each peak are 140 ± 20, 3 ± 1, and 10 ± 3 m^2/g, respectively, while the corresponding volume fractions are 0.004 ± 0.001, 0.026 ± 0.005, and 0.056 ± 0.018, respectively. Comparison of the results from SAXS and TEM showed good agreement.

1.2.13 Small-Angle Scattering Studies of Voids in Neutron Irradiated Molybdenum[47] — S. Liu,[48] J. Moteff,[48] R. W. Hendricks, and J. S. Lin

Disks of molybdenum were irradiated in the Oak Ridge Research Reactor to a fast-neutron fluence of about 1×10^{25} n/m^2 at temperatures between 220 and 900°C. The defect structure in the neutron-irradiated specimens was determined by transmission electron microscopy (TEM) to consist of both dislocation loops and small voids at the lower irradiation temperatures, whereas essentially only voids were observed at the higher irradiation temperatures. Small-angle x-ray scattering

---

[47]Abstract of paper accepted for publication in *Journal of Applied Crystallography*.

[48]Department of Materials Science and Metallurgical Engineering, University of Cincinnati, Cincinnati, Ohio.

(SAXS) measurements were made with the ORNL 10-m small-angle x-ray camera using Mo Kα radiation. Satisfactory agreement between the TEM and SAXS results for the void sizes and degree of swelling has been obtained in those samples containing essentially only voids. However, for samples containing both small voids and dislocation loops, the values of both void sizes and the degree of swelling as determined by SAXS were consistently larger than those obtained by TEM. We believe that the presence of the small irradiation-induced loops contributes a significant fraction of the x-ray scattering.

1.2.14 A Dynamic Study of the Crystallization of Polyethylene[47] — J. M. Schultz,[49] J. S. Lin, and R. W. Hendricks

Crystallization of a linear polyethylene from the melt was followed in situ with the ORNL 10-m SAXS camera. Specimens were rapidly cooled in the x-ray beam in tandem birdcage furnaces from approximately 180°C to temperatures between 115 and 126°C, and scattering patterns were recorded for 30 s in 50-s intervals. Because of this relatively high-speed data acquisition, we could obtain data in time periods that were short compared with the rate of change of the scattering patterns. The SAXS curves showed shapes that changed continuously during crystallization. The scattering curves are the superposition of a zero-angle peak and a Bragg maximum. Guinier plots of the zero-angle peak manifest scattering by lamellae of constant thickness. The thickness value is nearly that expected for crystallites at these crystallization temperatures. A model in which skeletal spherulites form and then later fill in is consistent with these results. Decreasing SAXS intensity and changing Bragg peak intensities indicate crystal thickening during cooling to room temperature.

---

[49]Department of Chemical Engineering, University of Delaware, Newark.

1.2.15 Effect of Crystallization Time on the Properties of Melt-Crystallized Polyethylene[50] — M. A. McCready,[49] J. M. Schultz,[49] J. S. Lin, and R. W. Hendricks

Linear polyethylene was crystallized isothermally from the melt. Specimens were removed at different crystallization times and quenched to room temperature. The density, static mechanical properties, and small-angle x-ray scattering (SAXS) behavior of these specimens were measured at room temperature. The density and Young's modulus increased with crystallization time, whereas the upper yield point decreased with crystallization time. A zero-angle peak gradually disappeared as crystallization time increased. Concurrently, the breadth of the SAXS peaks, their Bragg angles, and the integrated intensity decreased. Changes in the ratio of second- and first-order peak intensities were also noted. On the basis of the SAXS and density data, it was concluded that the thickening of existing crystals competes with the creation of new crystallites between the older ones. At relatively low crystallization times, numerous new crystals can form during quenching to room temperature, whereas quenching after prolonged crystallization results primarily in the additional thickening of existing crystals. No change in the density of the amorphous material was found. A model is given whereby the upper yield stress is coupled to these morphological changes through the thickness of the resulting amorphous layers.

1.2.16 Kinetics of Lamellar Thickening During Isothermal Crystallization of Polyoxymethylene From the Melt[51] — P. H. Karr,[52] P. Predecki,[52] R. W. Hendricks, and J. S. Lin

Samples of polyoxymethylene (Delrin 500, $\bar{M}_n$ = 35,000–40,000, and Delrin 100, $\bar{M}_n$ = 65,000–70,000) were isothermally crystallized from the melt at various temperatures, T_x, from 151 to 161°C and crystallization times, t_x, from 5 s to 10 h.

The lamellar crystal thickness, ℓ, and the long period, L, at room temperature were determined by the fast-heating-rate (1500°C/min)

---

[50]Submitted to *Journal of Polymers: Polymer Physics Edition.*
[51]Submitted to *Journal of Macromolecular Science.*
[52]Department of Chemistry, University of Denver, Denver, Colo.

melting temperature method and the ORNL 10-m small-angle x-ray scattering system. The value of $\dot{\iota}$ does not change appreciably with t_x but increases with T_x and molecular weight. However, ζ increases linearly with log t_x, suggesting that as crystals form from the melt they thicken at the expense of interlamellar amorphous material. Fold surface free energies of 40.8 ± 3.1 and 43.8 ± 2.3 mJ/m^2 were obtained for Delrin 500 and 100, respectively. Arrhenius plots were made of the lamellar thickening rate at fixed values of t_x and at fixed values of ζ. Assuming a single-relaxation-time process, the former gave activation energies of 130 ± 12 and 106 ± 13 kJ/mol (31.2 ± 2.8 and 25.3 ± 3.0 kcal/mol) for Delrin 500 and 100, respectively, in agreement with values reported for the α relaxation. The latter gave activation energies for thickening in the range 0.4 to 1.3 MJ/mol (100–300 kcal/mol). These energies increased linearly with ζ and were larger for the lower molecular weight polymer at the same ζ. This linear dependence of ζ supports a thickening mechanism in which all the repeat units in a single traverse of the crystal by a chain are simultaneously activated.

The molecular weight dependence of the fold surface energy and the activation energies suggests that the presence of crystalline chain ends at crystal surfaces reduces the dilatational strain at the crystal-to-amorphous interface.

1.2.17 Melting Temperature and Lamellar Thickening During Isothermal Crystallization of Bulk Polyoxymethylene[53] — P. H. Karr[52] P. Predecki,[52] R. W. Hendricks, and J. S. Lin

Changes in lamellar morphology during isothermal crystallization have been studied with an improved melting temperature method and a rapid small-angle x-ray scattering (SAXS) method for polyoxymethylene of two molecular weights: Delrin 500 and 100 having $\bar{M}_n$ = 35,000–40,000 and 65,000–70,000, respectively. Samples were isothermally crystallized at various temperatures, T_x, from 151 to 161°C, and for various times, t_x, from 5 s to 10 h in an optical hot stage. The ORNL 10-m camera was used for the SAXS study. Detailed analysis of the data

[53] *Abstract of Polymer Preprints* 19(1): 572–77 (1978).

showed that (1) the SAXS long period of polyoxymethylene does not change appreciably with crystallization time but increases with crystallization temperature and molecular weight, (2) the lamellar crystal thickness changes linearly with log t_x, (3) the fold surface free energy decreases slightly with T_x and increases with molecular weight, and (4) the activation energies for thickening are 105 to 130 kJ/mol (25–31 kcal/mol) at fixed t_x and in the range of 0.63 to 1.05 MJ/mol (150–250 kcal/mol) at fixed lamellar crystal thickness.

1.2.18 The Use of Anisotropic Small-Angle X-Ray Scattering Data for the Study of Deformation of Polymer Systems[50] — S. K. Baczek,[54] R. S. Stein,[54] R. D. Carlson,[55] and R. W. Hendricks

We have performed deformation experiments using the ORNL 10-m small-angle x-ray scattering camera in which samples of polyethylene were deformed to various strain ratios up to 1.83 and the increasingly anisotropic scattering patterns were recorded. The Hermans orientation function was computed for each strain and the results indicate that the predictions of an overall affine model are followed over the entire elongation range studied, but that localized positionally dependent processes that deviate from affineness occur.

1.2.19 Positron Lifetimes in Voids and Other Defects in Annealed, Neutron-Irradiated Aluminum[56] — J. D. McGervey,[57] V. W. Lindberg,[57] and R. W. Hendricks

A single crystal of aluminum was irradiated at 55°C to a fast fluence of 4.96×10^{25} n/m^2 in the HFIR. Pieces of the specimen were annealed at temperatures between 150 and 350°C. The void sizes and swelling were measured by small-angle x-ray scattering, and positron lifetimes were measured after each anneal. Below 310°C, where voids

---

[54]The Polymer Research Institute, Polymer Science and Engineering Department, University of Massachusetts, Amherst.

[55]Now with Biology Department, Brookhaven National Laboratory, Upton, New York.

[56]Abstract of *J. Nucl. Mater.* 69/70: 809–12 (1978).

[57]Physics Department, Case Western Reserve University, Cleveland, Ohio.

were present, three positron lifetimes were observed, corresponding to annihilations from positrons in the bulk, those trapped in voids, and those trapped in some other defect, hypothesized to be small vacancy-silicon clusters. Above 310°C, only bulk and defect annihilations were observed.

1.3 FUNDAMENTAL CERAMICS STUDIES — C. S. Yust

Erosion is a complex form of wear, involving simultaneous operation of several basic wear mechanisms. We are studying erosion in an effort to better understand the operation of these mechanisms in crystalline nonmetals. Such materials are expected to be used in coal conversion plant applications involving exposure to high temperature, corrosive environments, and high-velocity abrasive particles, where optimization of the materials to be used requires an understanding of the erosion damage process. Our observations show that some ceramics are subject to plastic deformation as well as fracture, even when eroded at room temperature. In fact, under some circumstances, local melting can be observed at particle impact sites.

In coal conversion systems, both the erosive and the corrosive aspects of the environment are the result of the chemistry of the coal in process. We are continuing our study of the nature of coal by the application of metallurgical techniques to extend the understanding of coal microstructure and coal mineralogy.

1.3.1 Melting at Particle Impact Site During Erosion of Ceramics[58] — C. S. Yust and R. S. Crouse

The eroded surfaces of high-alumina and mullite refractories were examined by scanning electron microscopy. The surfaces, which were exposed to 240-μm-diam silicon carbide particles carried in an argon gas stream at 24 m/s, are found to contain regions of fracture and regions of plastic shear. In the sheared regions, long stringers of the eroded surface are pulled away from the surface in the direction of motion of the

[58]Abstract of a paper accepted for publication in *Wear*.

eroding particle. The surface appearance at the impact site is indicative of the flow of a viscous liquid. Calculations show that local temperatures above the melting temperature of alumina can be attained. The calculation and the surface appearance indicate that melting can occur at impact sites in alumina and in mullite refractories.

1.3.2 The Erosion of Alumina and Mullite Refractories — C. S. Yust

Samples of alumina and mullite commercial refractories have been erosion tested at room temperature and at 500°C. The specimens were prepared from commercial bricks and from cast blocks. In the case of alumina, a dense polycrystalline body was also tested. The samples were exposed to a stream of 240-μm-diam silicon carbide particles carried in an argon gas stream at 24 m/s. Erosion rates were measured for each form, and the surfaces were studied by scanning electron microscopy.

The erosion rate is related to the microstructure of the material. In general, the denser the body, the more resistant it is to erosion. However, the alumina erosion rate did not vary with temperature, while the erosion rate of mullite was diminished by an increase in temperature. Surface examination reveals that fracture is the principal mechanism by which material was removed from the alumina surface at both temperatures under the imposed erosion conditions. Under the same conditions, however, a significant portion of the damage in mullite is due to plastic processes. The plastic mechanism is apparently less efficient in removing material from the surface and is active to a greater degree in mullite at elevated temperatures.

1.3.3 Single-Crystal Erosion Experiments — C. S. Yust

Experiments are in progress involving the preparation of single particle impacts on single-crystal surfaces. These experiments provide the opportunity to control the orientation relationship between the impinging particle and the target lattice, and will facilitate the analysis of any deformation that may occur. Experiments have been performed to date on alumina single crystals and on lithium fluoride single crystals. On alumina, scanning electron microscopy has demonstrated

that melting can be induced at the impact site if sufficient energy is transferred to the target. Alumina crystals eroded by 240-μm-diam silicon carbide particles striking the surface at 24 m/s do not show significant evidence of melting, while the same particles colliding with the surface at 55 m/s commonly show melting indications. In general, deformation on the basal planes of the hexagonal alumina is also observed at impact sites. In lithium fluoride, which melts at only 840°C, melting is not observed at impact pits, but the cubic lattice deforms extensively. Further details of the deformation and melting behavior will be studied by transmission electron microscopy.

1.3.4 The Application of Near-Infrared Microscopy to Materials Science[59] — L. A. Harris

The use of an infrared imaging tube in conjunction with optical microscopy extends the range of useful wavelengths from 400–750 nm to 400–1200 nm. Thus, a host of materials whose transparency increases in the near infrared can now be studied by transmission light microscopy. A review of materials that have been examined by infrared microscopy is presented. In addition, results from current studies on ceramic material at this laboratory are discussed.

1.3.5 Transmitted Near Infrared Microscopy of Coal[60] — L. A. Harris and C. S. Yust

Thin sections of an eastern Kentucky high-splint coal (high-volatile bituminous) from the Thiessen collection have been studied by transmitted infrared microscopy. Several normally opaque structures in the inertinite maceral group were observed to transmit in the near infrared (700–1200 nm). These same structures were also found to be birefringent and to consist of variably oriented optical domains similar in appearance to a polycrystalline material.

---

[59]Abstract of a paper accepted for publication in *Microstructural Science*.

[60]Abstract of a paper submitted for publication in *Fuel*.

1.3.6 Microporosity and Micromineralogy in a Bituminous Coal — J. S. Lin, R. W. Hendricks, L. A. Harris, and C. S. Yust

The size and distribution of porosity and minerals in a high-volatile bituminous coal determined by transmission electron microscopy agreed well with the values obtained by small-angle x-ray scattering. An abstract describing these studies is given in Sect. 1.2.12 of this report.

1.3.7 A Study of Solids Formed in a Solvent Refined Coal Pilot Plant[60] — L. A. Harris, C. R. Kennedy, and C. S. Yust

Optical and x-ray diffraction methods have been used to study microstructures in a carbonaceous deposit. This deposit, obtained from a feed line in a solvent refined coal (SRC) pilot plant, was shown to consist primarily of minerals and semicoke. The semicoke formed the matrix phase surrounding the minerals, mineral and coke mixtures, and fusinite.

The studies revealed that all the pyrite had been transformed to pyrrhotite, which in turn formed shell-like structures surrounding both inorganic and organic constituents. In addition, the slurry mixture of coal and solvent oil had been converted to semicoke.

1.3.8 SEM and EMA Studies of a Solvent Refined Coal Pilot Plant Carbonaceous Plug[61] — L. A. Harris and C. S. Yust

Scanning electron microscopy (SEM) and electron microprobe analyses (EMA) have proven to be extremely useful methods for analyzing microstructures observed in a carbonaceous material retrieved from a feed line of a solvent refined coal (SRC) conversion plant. Typical petrographic micrographs revealed a semicoke matrix enclosing nearly uniformly sized minerals or mineral assemblages, as well as unaltered coal (fusinite) fragments. The identity of the minerals, by SEM and EMA, revealed two distinct mineral types within the plug, namely minerals that have undergone transformations, such as pyrite (FeS_2) →

---

[61] Abstract of pp. 537–42 in *Scanning Electron Microscopy/1978*, Vol. 1, ed. by O. M. Johari, Scanning Electron Microscopy, Inc., AMF O'Hara, Illinois.

pyrrhotite (FeS), and those minerals that are essentially unaltered; for example, quartz and kaolinite.

The examination of porous areas within the semicoke constituent showed a variety of solidified "mesophase" spherules either as individuals or as coalesced groups. These observations are significant in that they reveal the mechanism by which semicoke forms; that is, by spherical liquid crystals separating from the coal and solvent oil slurry. We observed additional structural features associated with the semicoke, such as ridges along the pore walls composed of coalesced spheres in a chainlike growth.

1.3.9 Submicron Mineral Component of Vitrinite[62] — R. A. Strehlow,[63] L. A. Harris, and C. S. Yust

Submicron mineral particles have been observed in the vitrinite maceral of Illinois No. 6 coal. Many of the particles displayed growth or cleavage forms, and were in the size range from the limit of resolution (about 4 nm) to about 100 nm. X-ray diffraction results indicate that the principal mineral components are the clays, illite and kaolinite, as well as quartz and some calcite. The sizes and number of particles have been measured on photomicrographs, since these factors may be related to the possible catalytic effectiveness of the minerals. Particles less than 30 nm in diameter account for about one-third of the mineral surface area of 0.30 m^2 per cubic centimeter of vitrinite. The weight fraction of minerals derived from the data is 0.015 kg minerals per kilogram of coal.

1.4 PREPARATION AND SYNTHESIS OF HIGH-TEMPERATURE AND SPECIAL SERVICE MATERIALS — G. W. Clark

Directional solidification of eutectics and the crystal growth of high-temperature materials form our central theme. We continue to devise and improve methods of directional solidification and crystal growth, to develop increased understanding of crystal growth processes and kinetics, and to provide materials needed in research. Crystals are

---

[62]Abstract of a paper accepted for publication in *Fuel*.
[63]Chemistry Division.

grown by several methods: by internal zone growth, by temperature-gradient zone melting, from molten-salt solvents, from supercritical aqueous systems, by edge-defined film-fed growth, by the Bridgman method, and by the Verneuil method. We investigate selected physical properties, both those related to the crystal growth process and those important for characterizing new compounds and eutectic structures. During this report period, our crystals were shared for investigating electron spin resonances, optical and elastic properties, deformation, field emission, and electronic oscillator quality.

Of specific consideration is the use of directionally solidified, complex eutectic and liquid-phase hot-pressed composites as special tool, turbine, or valve seat materials. Properly chosen, such composites may offer better microstructures and provide superior mechanical properties for enhanced wear resistance or toughness than the fine-grained composites commonly used in tools for cutting, drilling, etc.

1.4.1 New Developments in the IZG of Metal Oxide-Metal Eutectic Composites — J. D. Holder and G. W. Clark

We presently know of 37 binary and 9 ternary refractory metal oxide-metal eutectics of the type M'_aO_b-M'', where $M' \neq M''$. These eutectics are of particular interest because of the potential of coupled optical, electrical, thermal, and mechanical properties between the refractory metal and oxide phases.

The directional solidification of metal oxide-metal eutectics by crucible techniques is severely limited by the lack of compatible materials. The internal zone growth (IZG) technique circumvents this crucible compatibility problem by balancing rf heating with the large heat losses at the sample surface to produce an unmelted skin, which serves as the crucible.

The IZG process has been mathematically modeled by R. A. Hartzell and R. F. Sekerka (Carnegie-Mellon University). They predict a temperature instability related to the rf coupling and heat transfer at various frequencies, sample diameters, and sample electrical conductivities. The instability is most devastating when the surface

temperature increases uncontrollably past the eutectic melting point, thereby resulting in surface melting.

The Hartzell-Sekerka calculations indicated that as the sample diameter is increased, the instability would occur at lower temperatures. This was experimentally demonstrated for 20-, 30-, and 50-mm-diam compacts formed from −325 mesh Cr_2O_3 and Mo powders. For both the 20- and 30-mm-diam compacts, the heating instability occurred above 1600°C and resulted in surface melting and spilling of the internal molten zone. In the 50-mm-diam compacts, the instability occurred at about 1200°C and was followed by uncontrollable heating to 1400°C. These samples were still in the solid state and could be controllably heated to form the internal melt zone.

A technique has been developed to circumvent (or greatly reduce) the effects of the rf-heating instability of Cr_2O_3-Mo compacts. This technique should also be applicable to other metal oxide-metal systems considered for internal zone growth.

1.4.2 Oxygen Partial Pressure vs Phase Equilibrium for Directional Solidification in the Cr-O-Mo System — J. D. Holder and G. W. Clark

Calculations made in 1976 predicted the oxygen partial pressure, P_{O_2}, that would be required for equilibrium of Cr_2O_3-Cr and Cr_2O_3-Mo eutectics with their melts. In 1977 the calculations were further extended to predict equilibrium P_{O_2} for off-eutectic compositions and superheated melts of eutectic. During this report period, study of the thermodynamics of gas-metal reactions yielded two criteria, which establish the first principles of composition control and alloying in metal oxide-metal eutectic composites. The first is an existence criterion; the second is an alloying criterion. Both are useful for understanding and controlling the chemistry of metal oxide-metal eutectic reactions. These same criteria may also be used to identify potentially new metal oxide-metal eutectic systems.

The existence criterion is derived with consideration of the oxidation and reduction reactions of each component of the metal oxide-metal eutectic system being investigated. It requires a range of oxygen partial pressures at temperatures above and below the eutectic temperature over which neither the metal phase nor the oxide phase is susceptible to oxidation and reduction reactions. The range of oxygen partial pressures can be readily calculated from the standard free energies of formation.

The alloying criterion is based on the recognition that except at one unique oxygen partial pressure, an M'_aO_b-M'' (M' ≠ M'') eutectic must be pseudobinary in the M'-O-M'' ternary system. The alloying criterion stipulates that for all oxygen partial pressures between the limiting partial pressures dictated by the existence criterion, a unique metal oxide-metal alloy exists upon freezing.

We have verified experimentally these criteria for the Cr-O-Mo system. This was done by directionally solidifying the Cr_2O_3-Mo eutectic with controlled, reproducible Mo-Cr solid solution metal fibers by controlling the oxygen partial pressure between two calculated limits. This oxygen partial pressure criterion is paramount in all alloying considerations in metal oxide-metal eutectic systems.

The thermodynamics of gas-metal reactions also indicates an array of interesting problems involved with (1) the directional solidification of the Cr_2O_3-Cr eutectic and other such M_xO_y-M' eutectics (where M = M'), (2) metal oxide-metal directional solidification by the Bridgman technique, and (3) the existence of Cr_2O_3-Ta, -Nb, or -V eutectics.

Last year with the use of the metal oxide-metal existence criterion we predicted that six systems would be stable: $LaCrO_3$-Cr, -Mo, and -W and $YCrO_3$-Cr, -Mo and -W. These criteria also should be applicable to other complex families such as sulfide-metal, oxysulfide-metal, nitride-metal, oxide-carbide, and other such systems where melt stoichiometry is sensitive to the partial pressure of a reactant gas.

1.4.3 Ternary Eutectics of $LaCrO_3$-La_2O_3-Mo and $LaCrO_3$-Cr_2O_3-Mo — J. D. Holder and G. W. Clark

The thermodynamic existence and alloying criteria used in predicting the stability and controlling the composition of binary eutectics between $LaCrO_3$-Mo, La_2O_3-Mo, and Cr_2O_3-Mo have been applied to two of the ternary combinations of these systems. Our predictions were that ternary eutectics of $LaCrO_3$-La_2O_3-Mo and $LaCrO_3$-Cr_2O_3-Mo could exist and could be synthesized under the partial pressure of oxygen developed by CO–10% CO_2 gas mixtures.

Appropriate mixtures of La_2O_3, Cr_2O_3, and Mo powders were hot-pressed to form 20-mm-diam rods. The rods were melted and resolidified by internal zone growth, and the microstructures were studied with standard optical techniques. Ternary eutectic structures were observed in both systems. The ternary eutectic temperatures were estimated to be about 1900°C by optical pyrometer measurements.

1.4.4 The Directional Solidification of $LaCrO_3$-Mo — J. D. Holder and G. W. Clark

Several rare earth chromites have been identified as potential MHD electrode materials, particularly $LaCrO_3$. In 1977, eutectics of $LaCrO_3$-W, $LaCrO_3$-Mo, $LaCrO_3$-Cr were synthesized. We have now successfully directionally solidified $LaCrO_3$-Mo by Internal Zone Growth (IZG) at 2.2 MHz frequency (for 0.20-mm diam compact). The gas mixture used for crystal growth was CO–9.5% CO_2 at 0.1 MPa. The eutectic temperature was determined by optical pryometer to be about 1950°C. The eutectic composites consist of a $LaCrO_3$ matrix with oriented Mo fibers of about 50×10^{10} fibers per square meter in the plane perpendicular to the growth direction.

1.4.5 Model of the Thin Film Effect in the Edge-Defined Film-Fed Growth of Eutectic Composites — J. D. Holder and G. W. Clark

A computer model of the boundary-layer difffusion problem for eutectic composite growth from a thin liquid film — as in edge-defined film-fed growth — has been developed. The model allows the

determination of fluctuations in composite composition due to growth rate irregularities. Results of our modeling indicate that for growth rate perturbations, there should be less composition fluctuation in eutectic composites grown from thin films than from infinite melts.

1.4.6 Directional Solidification of Metal-Metal Boride Eutectics — S. L. Bennett and G. W. Clark

Studies on the eutectic systems Co-WCoB, Ni-Mo_2NiB_2, Fe-Mo_2FeB_2, and Ni-W_2NiB_2 are continuing. We have refined the eutectic compositions for the first three systems. The eutectic microstructures exhibited by these systems are lamellar, blocky, and rod-type, respectively.

Several attempts have been made to directionally solidify the Co-WCoB eutectic. The prereacted sample, contained in an alumina tube, was withdrawn through a water-cooled coil situated within a graphite furnace heated to 1550°C. However, only modest successes were achieved. In order to improve the unidirectional growth, larger temperature gradients would be required. We have constructed an apparatus that allows the sample to be heated by rf power (10 kW, 400 kHz) and to be withdrawn through a water spray. Gradients of 250–350°C/cm are anticipated. Working with the Co-WCoB eutectic system we have achieved excellent alignment of the WCoB lamellae. Experiments are in progress to study the interlamellar spacing as a function of growth rate. Mechanical property measurements are to be made.

A 1957 patent[64] claimed that superior cutting tools can be produced from compositions within a large area of the three-phase region bounded by Mo_2NiB_2, Mo_2B, and MoNi. We have demonstrated that a eutectic trough extends through this three-phase region. Our interpretation of the experimental results was complicated by incongruent melting of all the components and segregation resulting from the slow cooling of the specimen. Drawing an arc-melted bead across selected samples demonstrated that segregation could be avoided, and the rapid solidification revealed a blade-type eutectic microstructure. However,

---

[64]R. Steinitz, U. S. Patent 2,776,468, January 8, 1957.

we are abandoning work on these compositions because the intermetallic phase MoNi is brittle.

We found in the literature that eutectics exist between some very hard borides and very hard carbides, for example TiB_2-TiC, ZrB_2-ZrC, TiB_2-B_4C, WB-W_2C and W_2B_5-B_4C. Recent Soviet work[65] has revealed a reduction in the hardness and an increase in the plasticity at compositions near the eutectics in the group IV boride-group IV carbide systems.

Superior high-speed cutting tools might be produced from such eutectics, and further improvements might be realized on directional solidification. We have begun preliminary studies on the TiB_2-TiC system.

1.4.7 Directional Solidification of Co-WC Melt — C. F. Yen and G. W. Clark

We continued to investigate the growth of Co-WC composites by directional solidification. We confirmed that a binary eutectic exists between Co and WC, with a discontinuous structure similar to that of aluminum and silicon. New differential thermal analysis results indicated that the eutectic temperature was near 1275°C. Our early attempts to grow composites were complicated by gaseous evolution from the melt, due to the presence of oxygen impurity in the as-received Co and WC powders. This outgassing can be avoided by either using a prereacted charge or adding minor amounts of aluminum.

An rf heating furnace has been constructed whereby, during directional solidification, the crucible can be cooled with a water spray below the induction coil. The temperature gradient at the liquid-solid interface exceeded 250°C/cm. We shall continue in our efforts to grow in situ composites with aligned WC fibers. Samples with the proper morphology will be characterized with property measurements.

---

[65] S. S. Ordan'yan, V. I. Unrod, and A. E. Lutsenko, *Inorg. Mater. USSR (Engl. Transl.)* 13: 546-47 (1977).

1.4.8 Hard Ceramic Composites — C. F. Yen and G. W. Clark

We extended our program on metal-ceramic systems to cover other complex ceramic components. Our study of the WC-TiB_2 system has begun. Carbide composites have widespread applications in cutting and drilling operations. Titanium diboride, on the other hand, demonstrated outstanding resistance to erosion and abrasion for the development of wear-resistant valve materials for coal conversion systems.[66]

Dense composites have been achieved by hot-pressing powders of the components. After a sample of original composition TiB_2–10 mol % WC was hot-pressed at 2100°C for 20 h, x-ray diffraction study determined it to be a three-phase composite of WB, $W_{0.56}Ti_{0.44}C$ and TiB_2. The room-temperature hardness was about 2700 DPH (5-kg load).

Experimental evidence indicated the formation of a liquid phase for the WC-TiB_2 join (tie-line) at temperatures below 2000°C. This would represent a lower melting reaction in the quaternary case when compared with the Ti-B-C and W-B-C systems.

1.4.9 Mechanical Strength of Hot-Pressed TiB_2-Fe Composites — C. F. Yen and G. W. Clark

The high room-temperature hardness and superb wear resistance of TiB_2 composites provide potential for tool applications. We have studied the enhancement in mechanical strength of TiB_2 composites through the addition of iron. Rectangular bar specimens with up to 20 wt % Fe were hot-pressed from fine-grained powders (in a graphite die) in the presence of a liquid phase. The experiments were generally carried out in vacuum at temperatures ranging from 1450 to 1800°C and with pressures up to 21 MPa (3000 psi) applied for 2 to 4 h. One sample, containing 10 wt % Fe, had an average room-temperature hardness of about 2400 DPH (5 kg load).

Four-point bending results on polished samples indicated that the improvement in strength of TiB_2 composites was proportional to the

---

[66]W. W. Leavenworth, J. E. Kelley, and J. S. Hansen, "Development of Wear-Resistant Valve Materials," in *Second Quart. Prog. Rep. January–March 1978*, Albany Metallurgy Research Center, Bureau of Mines, Albany, Oregon.

volume fraction of the Fe phase on the surface under tension (Fig. 1.1). However, one particular exception was a sample with an interesting microstructure of some eutectic-like Fe-TiB_2 regions intermingled with TiB_2 grains on the polished surface. It had a mechanical strength of 613 MPa (point A in Fig. 1.1). Scanning electron microscopy revealed some transgranular fracture and also suggested evidence that microcracking nucleated from pores existing inside exceptionally large TiB_2 grains (~100 μm). The iron phase was present both as grains at multigrain junctions and also as thin films between TiB_2 grains. They are thought to act as barriers to crack propagation during fracture.

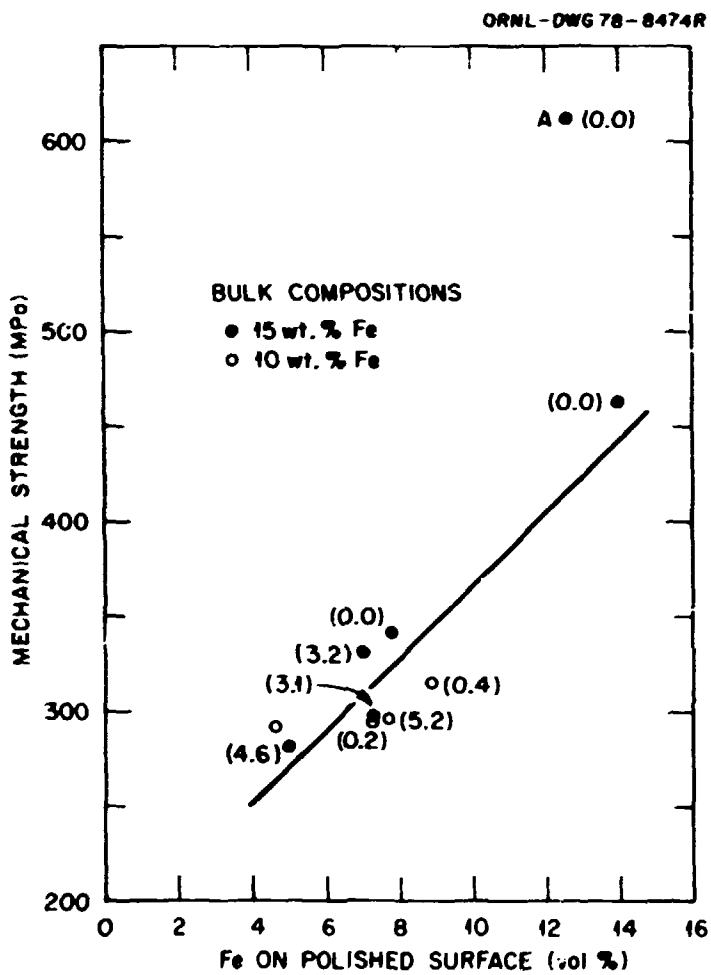

Fig. 1.1. The Mechanical Strength of TiB_2 Composites is Enhanced by the Increase in Fe Content. A: specimen with eutectic in microstructure. (Numbers in parenthesis represent the volume percent of porosity on the surface.)

1.4.10 Hydrothermal Growth of Quartz – O. C. Kopp and G. W. Clark

The large-diameter (~32 mm ID) hydrothermal vessel and new furnace system have now been completed and are in operation. Temperature along the axis of the vessel can be controlled within ±2°C over the usual 14-d growth period through the use of a single base heater (constant power input) supplemented by two cylindrical heaters whose power inputs are temperature controlled. Initially, the vessel is pressurized with distilled water alone. After operating conditions are reached, a portion of the distilled water is removed, at pressure, and replaced with a concentrated alkaline solution to bring the vessel to its final operating conditions of temperature, pressure, and solvent molarity. This avoids early leaks that may occur if the solvent is heated directly.

Three test runs have been completed. Crystals of sufficient size for the fabrication of oscillator plates were obtained. During the next several months we expect to grow several crystals under a variety of conditions for both infrared and anelastic loss measurements.

1.4.11 Czochralski Growth of Single-Crystal Fe_2SiO_4 (Fayalite)[67] – C. B. Finch, O. C. Kopp, and G. W. Clark

Single-crystal boules of Fe_2SiO_4 (fayalite) up to 10 mm in diameter by 15 mm in length were grown by the Czochralski method. The crystals were pulled at about 1200°C from high-purity oxide melts of an approximate 2:1 Fe:Si proportion. The melts were contained in platinum crucibles under moist Ar–4% H_2, an atmosphere ($P_{O_2} \cong 0.1$ μPa) that favored the stability of Fe(II). Growth rates in the [001] and [100] directions of up to 0.8 μm/s (~3 mm/h) were possible by cooling the seed with a current of inlet gas (~5 cm^3/s) and thermally shielding the growing crystal from the exposed crucible walls and melt surface with iridium. Under these conditions, the growth interface was very nearly planar. Uniform temperature control and cooling gas regulation were necessary to prevent spurious growth and freezing of the exposed melt

[67]Abstract submitted to 4th American Conference on Crystal Growth, Gaithersburg, Md., July 16–21, 1978.

surface. Boules were prone to crack when rapidly cooled, but usually survived intact when cooled to room temperature over 1-h periods. Crystals appear black in reflected natural light, but are amber by transmission in thin section (<200 μm). The lattice parameters were determined by the Debye-Scherrer technique to be: a_0 = 0.48218 (±0.00004), b_0 = 1.04768 (±0.00008), and c_0 = 0.60884 (±0.00008) nm for an orthorhombic, olivine-structure cell. The measured density of 4.37 ± 0.03 Mg/m^3 (Berman balance) closely approximated the value of 4.40 Mg/m^3 computed from the diffraction data (an integral stoichiometry being assumed). The optical absorption spectrum is similar to that previously recorded for natural fayalite.

1.4.12 Investigation of the Melting Behavior and Possible Defect Structure of Czochralski-Grown, Single-Crystal Fe_2SiO_4 (Fayalite) — C. B. Finch, M. M. Abraham,[68] J. O. Thomson,[69] and C. F. Yen

Considerable discussion exists in the literature concerning the melting behavior and defect structure of crystalline Fe_2SiO_4, a compound of current interest in pyrometallurgical and geophysical (earthquake) research. Previous work suggested that Fe^{3+}-free Fe_2SiO_4 should melt incongruently. To reconcile these data with our Czochralski (melt) growth of single-crystal Fe_2SiO_4, we performed differential thermal and thermogravometric analyses on our as-grown crystals under simulated growth conditions. Additionally, we analyzed the crystal Fe^{3+} content by Mössbauer, wet chemical (colorimetric), and electron paramagnetic resonance methods. The results indicate that our samples melt congruently at 1205 ± 2°C, displaying no observable phase transitions or weight loss before melting. A small, gradual weight loss after melting was attributed to evolution of O_2 and apparently accompanied diffusion of iron into the platinum test crucible (which had not been presaturated with iron). The consequent change in the melt composition was substantiated on cooling, where primary Fe_2SiO_4

[68]Solid State Division.
[69]Department of Physics, University of Tennessee.

crystallization (1188 ± 2°C) was followed by traces of eutectic solidification (1163 ± 2°C).

The Fe^{3+} content of our as-grown Fe_2SiO_4 crystals was below the limits of detection of the three analysis methods: Mössbauer, <2%; colorimetric, <1000 ppm; EPR, <5 ppm. Our crystals would thus appear to be devoid of any significant iron-vacancy-compensated Fe^{3+} defect structure, and on the basis of density would appear to be of an approximate integral stoichiometric composition.

1.4.13 Melt Growth of $RbCaF_3$ and ThF_4 under Gaseous HF[70] — C. B. Finch

To provide samples for spectroscopic studies, single crystals of $RbCaF_3$ (mp ≈ 1125°C) and ThF_4 (mp ≈ 1100°C) were grown by the Bridgman (melt solidification) method. The melts were contained in conical-bottom platinum vessels and were swept by a slow current of diluted anhydrous HF. The HF eliminated oxide impurities in the starting materials and ensured an optimal crystal optical clarity. Growth rates of 0.8 μm/s (≈3 mm/h) with an interface dT/dx of about 25°C/cm resulted in single crystals up to 10 by 10 by 10 mm.

1.4.14 Preparation of $ThBr_4$ and $ThCl_4$ Single Crystals Containing Tb or Bk — C. B. Finch and M. Hussonnois[71]

Single crystals of $ThBr_4$ (mp ≈ 700°C) and $ThCl_4$ (mp ≈ 820°C) up to 4 mm in diameter by 10 mm were grown from the melt by the Bridgman method. The anhydrous melts were contained in evacuated and sealed quartz ampules, which were lowered through a 20°/cm furnace thermal gradient at ∿1 mm/h. Crystals were doped with about 1000 cation ppm Tb, and (for the case of $ThCl_4$ only) with about 1000 ppm ^{249}Bk. The resulting samples are part of an electron paramagnetic resonance and optical study of lanthanide and actinide dopants in thorium tetrahalide hosts. The $ThCl_4$:Bk sample, which has a green self-luminescence, will

---

[70] A portion of this work was performed in collaboration with the Institut de Physique Nucleaire, Orsay, France.

[71] Guest from Institut de Physique Nucleaire, Orsay, France.

be examined by N. Edelstein at Lawrence Berkeley Laboratory, M. Abraham at ORNL Solid State Division, and others.

2. DEFORMATION AND MECHANICAL PROPERTIES

2.1 PHYSICAL METALLURGY — R. A. Vandermeer

The research of this group focuses on several topics in physical metallurgy: (1) the fundamentals of annealing phenomena, (2) the mechanisms of phase transformation, and (3) deformation processes. The following then are summaries and abstracts of our most important contributions during the past year. We emphasize the relationship between structure and properties in this work.

2.1.1 Shape Memory Effects in U–14 at. % Nb Alloy[1] — R. A. Vandermeer, J. C. Ogle, and W. B. Snyder, Jr.[2]

If uranium–niobium alloys near the monotectoid composition are rapidly cooled from the high-temperature bcc phase, the diffusion-controlled formation of the equilibrium phases can be skipped. Alternatively, displacement transformations occur, resulting in metastable transition phases. Dilatometry has been used to detect these transformation events. Recently progress has been made in identifying and characterizing a shape memory effect (SME) in these alloys. Uniaxial tension tests followed by dilatometric observations established that as much as 7% strain can be completely recovered simply by heating a deformed alloy containing 14 at. % Nb. This strain recovery has been correlated with the reversion of the above-mentioned metastable phases, particularly the α'' (monoclinic) $\rightarrow \gamma^{\circ}$ (tetragonal) transition, to the bcc allotrope during heating. This and other circumstantial evidence suggest that α'', the metastable room-temperature phase, is a thermoelastic martensite. Unlike other SME alloys, the precursor to the martensite phase is not chemically ordered; it is displacement ordered, instead. It was also demonstrated that the SME is two-way: a portion of the strain is reversible on partial heating and subsequent cooling.

---

[1]Summary of *Scr. Metall.* 12: 143–48 (1978).
[2]Development Division, Oak Ridge Y-12 Plant.

2.1.2 The Development of Texture and Its Role in Shape Memory Behavior in a Uranium Alloy[3] — R. A. Vandermeer and O. B. Cavin

The U–7.5 wt % Nb–2.5 wt % alloy when quenched from a high temperature undergoes a displacement ordering reaction: γ (bcc) → γ° (tetragonal). In certain respects the alloy behaves analogous to a martensitic gold-cadmium SME alloy. During deformation at low strains, a pseudoelastic, transformation-associated strain component was operative in the alloy. Bending and tension experiments have revealed that: (1) the pseudoelastic strain component can be stabilized by aging under constraint at intermediate temperatures, and subsequently recovered by heating to much higher temperatures; (2) twinning is an important deformation mode and many of the twins behave elastically during loading and unloading; and (3) a profound grain reorientation can be accomplished at strains below 1%. Pole figures have been obtained from the outer fiber tension and compression layers of four-point bend specimens and the outer fiber tension surfaces of U-bend specimens documenting this deformation-produced, transformation-associated texture. Detailed studies have confirmed that grain reeorientation during bending caused the longer tetragonal a-axes to align with the tension axis but perpendicular to the compression axis, while conversely the shorter c-axis aligned with the compression axis and perpendicular to the tension axis. Such a texture is the key to understanding aging-induced shape instability in the alloy.

2.1.3 Recovery and Recrystallization in Rolled Tantalum Single Crystals[4] — R. A. Vandemeer and W. B. Snyder, Jr.[2]

The recovery and recrystallization behavior of rolled tantalum single crystals having the initial orientations (001)[1$\bar{1}$0], (112)[1$\bar{1}$0], and (111)[1$\bar{1}$0] has been studied. Each crystal developed a simple single-component texture on rolling. The texture became more diffuse and the local lattice curvature more intense as the rolling plane

---

[3]Summary of paper presented at 5th International Conference on Textures of Materials, Aachen, West Germany, March 28–31, 1978. Paper to be published in Conference Proceedings.

deviated from (001) towards (111). The (001)[$\bar{1}$10] and (112)[$\bar{1}$10] crystals formed a uniform dislocation array, and on annealing only polygonization occurred. The (001)[$\bar{1}$10] crystal did not recrystallize at temperatures up to 1400°C. A few randomly oriented recrystallized grains were nucleated in the (112)[$\bar{1}$10] crystal, but these may have been artificially nucleated. Only the (111)[$\bar{1}$10] crystal reoriented during rolling; it also formed a cellular dislocation microstructure. This was the only orientation to recrystallize easily, primarily because of the large lattice curvature. Wide log normal dislocation cell size distributions were noted in this crystal. Subgrain growth was relatively more rapid in this crystal than the others. However, all cases had a large discrepancy between the observed subgrain growth rate and that theoretically predicted by the coalescence model. The orientation of the recrystallized grains in the (111)[$\bar{1}$10] crystal was related to the deformation texture by a rotation of 23–24° about a common ⟨111⟩ direction parallel to the normal direction of the sheet. The nature of the misorientation spread after rolling may have dictated this relation as a compromise to the one usually found in bcc materials: 25–30° rotation about a common ⟨110⟩ axis.

2.2 GRAIN BOUNDARY SEGREGATION AND FRACTURE — C. L. White

2.2.1 Low-Temperature Grain Boundary Fracture[5] — C. L. White

The embrittlement of Fe–3% Si bicrystals by phosphorus is being investigated. Fracture tests in liquid nitrogen (77 K) indicate large decreases in fracture energy (at least one order of magnitude) as the bulk phosphorus concentration is increased from less than 10 to 1200 ppm. Analysis using Auger electron spectroscopy (AES) indicates that samples

---

[4]Abstract of invited paper presented at TMS-AIME Symposium on "Recovery, Recrystallization and Grain Growth in Materials," Chicago, Oct. 24–27, 1977. Paper to be published in *Metallurgical Transactions*.

[5]Cooperative study with J. J. Wert and R. G. Thompson, Vanderbilt University.

containing 1200 ppm P have approximately 30 at. % P at the grain boundaries. Samples containing less than 200 ppm P have not yet been successfully analyzed by AES, so information on phosphorus segregation is limited to the alloys with higher phosphorus concentrations.

A series of fracture tests in liquid helium will be carried out, and additional attempts to analyze the grain boundary composition in the low-phosphorus alloys will be made.

2.2.2 Solute and Impurity Segregation to Creep Cavities[6] — C. L. White

Auger analysis of type 316 stainless steel containing creep cavities has shown localized regions of high phosphorus and sulfur concentration on fracture surfaces exposed in vacuum. It is suspected that these regions correspond to impurity-enriched surfaces of creep cavities. Extensive impurity segregation to creep cavity surfaces, if verified, could have significant implications regarding the role of impurities in grain boundary cavitation during creep.

---

[6]Cooperative study with V. K. Sikka, Mechanical Properties Group, Metals and Ceramics Division.

3. PHYSICAL PROPERTIES AND TRANSPORT PHENOMENA

3.1 MECHANISMS OF SURFACE AND SOLID-STATE REACTIONS — J. V. Cathcart

The fundamental research of this group is aimed at understanding basic mechanisms of oxidation and diffusion. In particular we attempt to understand the influence of defect interactions on diffusion processes in both metals and oxides and in material transport phenomena in growing alloy oxide scales. Specific projects worked on during the past year include an investigation of the dissociative mechanism of diffusion in lead-base alloys, studies of the diffusion of interstitials (tritium) and aliovalent cations in oxides, characterization of the defect structure of FeS and the scale morphology and rate of sulfidation of iron in pure sulfur vapor, and a study of the high-temperature oxidation of zirconium and its alloys.

3.1.1 Diffusion in Oxides

3.1.1.1 Current Investigations — J. V. Cathcart and L. C. Manley, Jr.

We extended our study of tritium diffusion in oxides to the system T-Al_2O_3. The corundum crystal structure of alumina is shared by chromia; thus this investigation will provide information concerning tritium diffusion in two technologically important oxides. The objective of the work is to provide an atomistic description of tritium diffusion in Al_2O_3 through the determination of the activation energy for diffusion in the temperature range 600 to 1000°C and through the identification of the diffusing species by infrared spectroscopy and Raman scattering experiments. These latter measurements will be made as a part of a cooperative study with the Solid State Division. Preliminary diffusivity determinations between 800 and 1000°C provided evidence for the operation of at least two diffusion mechanisms in Al_2O_3 and suggested that the extrinsic defect structure of Al_2O_3 may significantly influence the rate of tritium diffusion in Al_2O_3.

3.1.1.2 Tritium Diffusion in Rutile (TiO_2)[1] — R. A. Perkins,[2] J. B. Bates,[3] and L. C. Manley

The diffusivity of tritium in rutile single crystals has been measured parallel to the *a*- and *c*-axes in the temperature range from 250 to 900°C. Raman scattering measurements were also made to aid in identifying a nonpolar tritium species involved in the diffusion process. Two species, OT^- ions and T_2 molecules, are involved in tritium migration. The OT^- ions dissociate before each tritium jump. Along the *c*-axis the T_2 molecules are slower by a factor of one-half. No dependency of the tritium diffusivity upon the rutile defect structure was observed. A zero-point energy correction was necessary to account for the difference between H^+ and T^+ diffusivities parallel to the *c*-axis.

3.1.1.3 Infrared Spectral Properties of Hydrogen, Deuterium, and Tritium in TiO_2 (Ref. 4) — J. B. Bates[3] and R. A. Perkins[2]

Infrared spectra of TiO_2 single crystals containing either hydrogen, deuterium, or tritium were measured at 300, 77, and 8 K. Bands observed at 3276, 2437, and 2065 cm^{-1} near 300 K are, respectively, assigned to OH^-, OD^-, and OT^- on the basis of a two-term anharmonic-oscillator model of the hydrogenic species. The frequencies were also analyzed by using a linear hydrogen-bonded model with harmonic forces, but the correlation between frequencies and band widths was at variance with that of known H-bonded systems. The absorption strength per ion of OT^- was calculated at several levels of approximation, and the best value determined was $a_T = 9.24 \times 10^{-20}$ m. The narmonic and anharmonic mean-square displacements of OH^-, OD^-, and OT^- were calculated, and the differences between these quantities reflect the changes in the infrared band widths with reduced mass.

---

[1]Abstract of paper submitted for publication in *Metallurgical Transactions*.

[2]Current address: Owens-Corning Fiberglas Corporation, Granville, Ohio.

[3]Solid State Division.

[4]Abstract of *Phys. Rev.* 16B: 3713–22 (1977).

3.1.1.4 Tracer Diffusion of Ti and Ni in NiO (Ref. 5) — R. A. Perkins[2]

The tracer diffusivities of Ni and Ti in high-purity single crystals of NiO were measured between 1000 and 1500°C and as a function of oxygen pressure from 0.1 MPa to 0.1 Pa (1 to 10^{-6} atm). At an oxygen pressure of 0.1 MPa (1 atm) the following expressions were obtained for the diffusivities in units of m^2/s.

$$D_{Ni}^{NiO} = 6.02\ (^{+8.5}_{-3.5}) \times 10^6 \exp[(-254 \pm 16\ kJ/mol)/RT]\ ;$$

$$D_{Ti}^{NiO} = 3.85\ (^{+3.2}_{-1.7}) \times 10^7 \exp[(-204 \pm 7\ kJ/mol)/RT]\ .$$

The error limits are for the 95% confidence level. The Ni diffusivity decreased with a 1/6 dependence on oxygen pressure over the entire temperature range, indicating the predominance of doubly ionized Ni vacancies in the NiO. Below 10 kPa (0.1 atm) D_{Ti}^{NiO} also decreased with P_{O_2}, but between 1100 and 1300°C and 100 and 10 kPa (1 and 0.1 atm) oxygen pressure, small increases in D_{Ti}^{NiO} were observed. Possible diffusion mechanisms are discussed.

3.1.2 Diffusion in Metals and Alloys

3.1.2.1 The Concentration and Temperature Dependence of Cadmium Diffusivity Enhancement in Lead-Cadmium Alloys[6] — P. T. Carlson and R. A. Padgett, Jr.

Experiments have been performed to explain the anomalously fast diffusion of cadmium in lead in terms of the dissociative mechanism of diffusion, in which a substitutionally dissolved solute atom is thermally activated to an interstitial position. The degree of interaction between the resulting vacancy and interstitial atom, as well as that between the interstitial and other substitutional solute atoms, can

---

[5]Abstract of paper to be submitted for publication in *Metallurgical Transactions.*

[6]Abstract of paper presented to the American Physical Society, Washington, D.C., March 27–30, 1978.

appreciably affect the solute and solvent diffusivities. The diffusivity of cadmium tracer in lead-cadmium alloys containing from 0 to 1.0 at. % Cd was measured from 200 to 300°C. At 200, 225, and 250°C the cadmium diffusivity in the alloy relative to that in pure lead decreased with increasing cadmium concentration in the very dilute regions. As the cadmium content increased, its diffusivity increased in accordance with the expected behavior of solute diffusivity enhancement. Furthermore, the decrease in cadmium diffusivity is more pronounced as the temperature decreases. We believe that the occurrence of such a minimum in the plot of $D_2(C)/D_2(0)$ versus cadmium concentration is a reflection of the existence of interstitial solute-substitutional solute pairs. This suggestion is supported by the observed temperature dependence, since the formation of solute-solute pairs is energetically favored at the lower temperatures. With the formation of relatively immobile solute-solute pairs, fewer atoms are available to contribute to the diffusivity; hence, the tracer diffusivity decreases. Experiments are being conducted currently to define the temperature dependence of the negative solute diffusivity enhancement coefficient, which will allow the determination of the solute-solute binding energies.

3.1.2.2 Anomalously Fast Diffusion in Pb-Ni and Sn-Au Alloys by the Dissociative Mechanism — P. T. Carlson and R. A. Padgett, Jr.

In conjunction with the study of diffusion processes in Pb-Cd alloys, two current investigations should contribute to an understanding of the mechanisms of fast diffusion. When dissolved in Pb, Ni is thought to reside principally on interstitial sites, in contrast to Cd, which resides primarily on substitutional sites. Consequently, an investigation of Ni diffusion in Pb represents the opposite extreme of the dissociative mechanism, in which the formation of interstitial-interstitial solute pairs is possible. We grew 14 single crystals of dilute Pb-Ni alloys of varying Ni content by a modified Bridgman technique in preparation for the study of solute diffusivity enhancement in this system.

Early experiments demonstrated that the diffusion of Au in pure Sn is approximately three orders of magnitude greater than the self-diffusion of Sn. These results were interpreted as evidence that Au

diffuses in Sn primarily by an interstitial mechanism. However, recent channeling experiments have indicated that 95% of the Au dissolved in Sn resides on substitutional sites. We have started to study solute diffusivity enhancement in Sn-Au alloys on the basis of this observation coupled with the anomalously fast diffusion of Au in Sn. In view of the results of the Pb-Cd research and recent evidence that Au atoms form solute pairs in Pb-Au alloys, a study of the concentration dependence of Au diffusivity in Sn-Au alloys is expected to add to the understanding of the dissociative mechanism and the role of solute-solute pairs.

3.1.2.3 Intrinsic Diffusion and Vacancy Flow Effects in Vanadium-Titanium Alloys[7] — P. T. Carlson

Intrinsic diffusion coefficients and vacancy flow parameters have been determined in the vanadium-titanium system from 900 to 1500°C. The experimental results reflect a greater influence of the vacancy flow phenomenon on the intrinsic flux of each species than that predicted by the random alloy model. The principal assumptions of the randon alloy model are that a single-vacancy mechanism is the operative diffusion mechanism and that all diffusing species find themselves in random environments with the absence of preferred sites for either atoms or vacancies. However, solvent diffusivity enhancement calculations suggest the existence of two competing vacancy mechanisms in this system. The observed discrepancies between theoretical and experimental values are examined in light of the occurrence of a combined monovacancy-divacancy mechanism. In addition, we discuss other nonrandom effects, which result in violations of the random alloy model assumptions and which lead to differences between theoretical and experimental quantities.

---

[7]Abstract of manuscript submitted for publication in *Metallurgical Transactions A*.

3.1.3 Diffusion Theory — R. A. McKee

3.1.3.1 Thermomigration in Alloys for Which Substitutional-Vacancy and Interstitial-Vacancy Mechanisms are Operative[8] — R. A. McKee

The theoretical treatments of alloy diffusion in a temperature gradient by the substitutional-vacancy mechanism and by the interstitial-vacancy mechanism were combined, and two types of thermomigration experiments, which differ in initial conditions, were analyzed. These experiments, as measurements of the impurity heat of transport, are apparently incapable of distinguishing between the two mechanisms of diffusion. However, an expression for the lattice velocity in such a combined-state alloy is developed and will distinguish between the two mechanisms in a rather specific fashion.

3.1.3.2 Solute and Solvent Diffusion for an Alloy in Dissociatve Equilibrium[9] — R. A. McKee

Solute and solvent diffusion have been analyzed with the pair association theory for a dilute fcc alloy in which the solute is partitioned between the three states of unassociated substitutional solute atoms, interstitial-vacancy close pairs, and isolated interstitial solute atoms. Correlation factors are identified for solute and vacancy motion, and the relationship between the enhancement factor for solvent diffusion and the vacancy correlation factor attributable to solvent-vacancy exchanges in the presence of the interstitial solute-vacancy defect has been derived.

3.1.3.3 The Concentration Dependence of Solute Diffusion for an Alloy in Dissociative Equilibrium[10] — R. A. McKee

An analysis of solute pairing for an alloy in dissociative equilibrium permits an expression to be written for the concentration-dependent, solute diffusion coefficient in a dilute fcc alloy. This

---

[8]Abstract of *Philos. Mag.* 35: 715–26 (1977).
[9]Abstract of *Phys. Rev.* B 15: 5612–17 (1977).
[10]Abstract of paper submitted for publication in *Physical Review*.

expression provides an explanation for recently reported measurements of Au diffusion in Au-Pb alloys and Ag diffusion in Ag-Pb alloys. Furthermore, a unique result is predicted for the change in diffusivity in such alloys since the extremes of the dissociative equilibrium allow the solute pairs to form in distinctly different configurations. The conclusions are presented in terms of correlation factors, solute-solute binding energies, and the formation energy of interstitial-vacancy pairs.

3.1.4 Sulfidation of Iron

3.1.4.1 Current Investigations — R. A. McKee, R. E. Druschel, and G. F. Peterson

One part of this program involves the growth of single crystals of FeS from specially synthesized starting material to characterize the defect structure of FeS adequately and provide samples for subsequent diffusion studies. Very high-quality FeS (Sect. 3.1.4.2), especially with regard to oxygen and carbon contamination, was successfully prepared. This material was used to grow FeS samples with a grain size of about 10 mm. The crystals were grown by the Bridgman technique in a boron nitride crucible contained in a system where the sulfur pressure could be carefully controlled. Magnetic susceptibility measurements on the crystals began.

In a second phase of this effort we are investigating the kinetics and morphology of sulfidation at 700 to 900°C. Essentially linear sulfidation rates were obtained at 700°C in pure sulfur vapor at about 1 and 100 Pa, indicating either interface or gas phase control of the kinetics. The corresponding high rate of cation vacancy diffusion in the FeS scale is reflected by the number of voids formed at the boundaries of the columnar grains of the FeS (see Fig. 3.1). The FeS in the scale must become more nearly stoichiometric as the specimen is cooled from the reaction temperature. This compositional readjustment is accomplished by

the rejection of excess cation vacancies and sulfur atoms. We hypothesize that grain boundaries in the FeS scale serve as sinks for the vacancies, thus leading to the void formation shown in Fig. 3.1. No voids are observed near the sulfide-gas or the sulfide-metal interfaces because vacancies in these regions of the scale have time to diffuse to either of these interfaces.

3.1.4.2 The Preparation of Pure FeS (Ref. 11) — G. F. Peterson and R. A. McKee

Iron sulfide (FeS) at least 99.99% pure was prepared by reacting the previously purified constituents in a quartz vessel at 650°C. We further purified MARZ grade iron powder by alternate oxidation and reduction of its surface in wet and dry hydrogen. Substantial quantities of carbon were removed from nominally 99.999% S by refluxing with MgO followed by vacuum distillation. Mass spectroscopy, neutron activation analysis, and fast-neutron activation analysis were used to determine final purity of the iron and sulfur.

3.1.5 Alloy Oxidation at Elevated Temperatures — R. E. Pawel and J. J. Campbell

Alloy oxidation kinetics is determined by mass transport across a growing oxide layer, and this process is influenced by a number of factors, including oxide impurities, scale morphology, and oxidation stresses. A mechanistic interpretation of scale growth is, therefore, greatly facilitated when oxidation parameters obtained under a variety of conditions can be compared. Such an approach, however, requires a high degree of measurement accuracy, a condition difficult to achieve at temperatures above 1000°C.

We have developed a technique that permits the oxidation behavior of reactive metals to be examined in a highly reproducible manner. The apparatus is based on a low-thermal-inertia radiant heating furance and employs a computer-operated data acquisition system for precise recording

---

[11] Abstract of paper prepared for publication.

Fig. 3.1. Section Through FeS Scale Formed in 1 h at 700°C in Sulfur Vapor at 1 Pa. Gas-sulfide interface is at the upper right. The lower left of the picture shows a portion of the specimen when the scale has spalled off. (a) 300×. (b) 1000×.

of the temperature excursions experienced by the specimens. Considerable effort has led to exceptional accuracy in temperature measurements and temperature control for oxidation experiments up to 1500°C. A high degree of reproducibility of the high-temperature kinetic data obtained by this technique allows us to base meaningful mechanistic interpretations on relatively small variations in oxidation rate produced by changes in the oxidizing medium or alloy compositon.

Zirconium and zirconium alloys have been chosen for the intital experimental materials for these studies because previous observations for Zircaloy-4 indicated that layer growth in the early stages of oxidation is parabolic and, therefore, may be amenable to simple modeling in terms of diffusion parameters. In such a case, the effect of alloying elements could be treated quantitatively in terms of differences related to the particular diffusion process determining the rate.

3.1.5.1 Oxidation of Zirconium from 900 to 1500°C — R. E. Pawel and J. J. Campbell

At temperatures above the alpha-beta transition, the oxidation of zirconium and certain of its alloys results in the formation of relatively uniform layers of zirconia and oxygen-stabilized α-zirconium, as well as the solution of oxygen into the innermost beta phase. This scenario is the framework of a model, based on diffusion behavior in the three phases, that describes the oxidation kinetics in terms of the mass-transport quantities.

An accurate set of oxidation data for Zircaloy-4 between 900 and 1500°C is available, and we will make a comparative study of the oxidation characteristics of pure zirconium in this same temperature range. The differences will be examined in terms of the model pictured above, with particular emphasis on describing the influence of the alloying element on the transport properties, the defect structure, and the morphology of the ZrO_2 scales. Experimental measurements of the kinetics of oxidation of crystal-bar zirconium are in progress.

3.1.5.2 The Kinetics of Oxidation of Zircaloy-4 in Steam at High Temperatures[12] – R. E. Pawel, J. V. Cathcart, and R. A. McKee

The kinetics of oxidation of Zircaloy-4 in steam was examined under isothermal conditions from 900 to 1500°C. Rate curves describing the growth of the reaction product layers, oxide and oxygen-stabilized alpha, were obtained at 50°C intervals under carefully defined and documented experimental conditons. The early stages of oxidation for temperatures above 1000°C were shown to be virtually ideally parabolic; below 1000°C, the growth of the oxide layer was nonparabolic.

Statistical evaluations of the data in terms of the rate constants and their Arrhenius parameters established the high degree of self-consistency of these measurements. The features of the experimental apparatus and techniques that were necessary to ensure accurate measurements are discussed.

3.1.5.3 "Anomalous" Oxide Growth During Transient-Temperature Oxidation of Zircaloy-4 (Ref. 13) – R. E. Pawel, J. V. Cathcart, and R. A. McKee

Oxidation tests of Zircaloy-4 PWR tube specimens in steam were conducted for several types of temperature excursions. These tests were used to evaluate the accuracy of predictions of the oxidation behavior based on ideal models that employ isothermal kinetic data. While oxidation during simple transient temperature excursions, where the peak temperature was between 1000 and 1400°C, could be predicted with reasonable accuracy, certain "two-peak" transients resulted in oxide layers considerably less than those anticipated. On the basis of our experiments, we propose that this effect is related to the manner in which the monoclinic-tetragonal phase transformation occurs in the oxide and the fact that the normal (bulk) transformation hysteresis is altered for a growing oxide film.

---

[12]Abstract of paper presented at meeting of the Electrochemical Society, Seattle, Wash. May 22–26, 1978.

[13] Abstract of paper prepared for publication.

3.1.5.4 Oxygen Diffusion in the Oxide and Alpha Phases of Zircaloy-4 During Oxidation in Steam from 1000 to 1500°C — R. E. Pawel

The effective chemical diffusion coefficients for oxygen in the oxide and alpha phases of Zircaloy-4 were determined from the parabolic rate constants for phase growth measured for steam oxidation. The equations for multiphase diffusion were solved in terms of the interface velocities, and the diffusion coefficients determined directly without resort to approximate calculations of the total oxygen consumed. A computer program was written to accomplish this calculation. The new calculations give values for D_2, the oxygen diffusion coefficient in the oxide phase, that are 2 to 4% lower than previously calculated. Values of D_1, the diffusion coefficient in the alpha phase, were unchanged. These data are important input to computer codes used to model this system.

3.1.5.5 Oxidation Kinetics of Zircaloy in Steam and Oxygen[12] — R. A. McKee, J. V. Cathcart, and R. E. Pawel

The reaction kinetics of the zirconium-base alloy Zircaloy-4 in steam in the range of temperatures from 1000 to 1500°C and in dry oxygen at 1253 and 1404°C is discussed. The reaction is slower in water vapor than in dry oxygen, and this result is analyzed in terms of the n-type semiconductor properties of ZrO_2 and of the scale morphology. The discussion and analysis of these experimental results provide a framework for a more coherent picture of the existing data for the zirconium-oxygen reaction.

3.1.5.6 MULTRAN — A Computer Program for Modeling Diffusion-Controlled Oxidation Reactions — S. Malang[14] and R. E. Pawel

We have written a computer program, MULTRAN, that models ideal layer growth oxidation processes by solving the diffusion equations for mass flow in a one-dimensional, multiphase, moving boundary system with finite geometry. The program utilizes finite difference calculations and can be applied to reactions with up to five separate product phases. Transient-temperature oxidation can also be considered.

---

[14]Guest scientist from Gesellshaft fur Kernforschung, Karlsruhe, FRG.

The program has been used to model the effect of specimen thickness on the isothermal growth of the oxide and alpha layers during steam oxidation of Zircaloy-4. These tests have shown that large changes in layer growth rates can be observed, depending upon the specimen geometry or the degree of saturation of the beta phase during the reaction.

3.2 PHYSICAL PROPERTIES RESEARCH — D. L. McElroy

This effort obtains and analyzes accurate values of physical properties of selected solids from 4.2 to 2600 K. A strong measurement capability is maintained for determination of thermal conductivity (λ), electrical resistivity (ρ), Seebeck coefficient (S), specific heat (C_p), coefficient of thermal expansion (α), and total hemispherical emittance (THE). Understanding the relationships between these properties and their temperature dependence provides: (1) useful insight about the solids, (2) information for systems where data do not exist, and (3) ways to improve and control properties. Improvement in the performance of many power generating systems is often limited by the lack of physical property data for solids.

3.2.1 Transport in Nonmetals

3.2.1.1 Method for Estimating Lattice Thermal Conductivity[15] — D. W. Yarbrough[16] and R. K. Williams

A method is described for calculating the lattice thermal conductivity of alloys as a function of temperature and composition for temperatures above $\theta_D/2$ using readily available information about the atomic species present in the alloy. The calculation takes into account phonon interactions with point defects, electrons, and other phonons. Comparisons between experimental thermal conductivities (resistivities) and calculated values are discussed for binary alloys of semiconductors,

---

[15]Abstracted from D. W. Yarbrough and R. K. Williams, *Method for Estimating the Lattice Thermal Conductivity of Metallic Alloys*, ORNL-5434 (in press).

[16]Consultant, Tennessee Technological University, Cookeville.

alkali halides, and metals. A discussion of the theoretical background is followed by sufficient numerical work to facilitate the calculation of lattice thermal conductivity of an alloy for which no conductivity data exist.

3.2.1.2 The Thermal Conductivity of Electrically Insulating AB_2 Compounds — J. P. Moore and F. J. Weaver

The thermal conductivity of a single crystal of SrF_2 has been measured from 80 to 400 K. The present results disagree with two previous measurements by others by +4% and −20% at 300 K. The thermal resistance, $1/\lambda$, is approximately linear with increasing temperature, and the deviations from linearity appear to be associated with the temperature dependence of the Debye temperature. The thermal resistance of SrF_2 is 3 times that calculated with the Liebfried and Schloman (L-S) equation. The thermal resistance of another AB_2 compound, ThO_2, is similar to that of SrF_2, and the comparison with the L-S equation yields a similar result. In some cubic crystals, such as rubidium and potassium halides, deviations from the L-S equation increase as the ratio of ionic masses increases. This is not the case here, however, since the ion mass ratio in ThO_2 is 14.5, whereas that in the SrF_2 is 4.61, and yet experimental results from both of these disagree with the L-S equation by a factor of 3.

3.2.1.3 Transport in Polymers — R. K. Williams[17]

Materials containing epoxy resins are used in constructing large superconducting magnets, motors, and generators. The thermal conductivity of these materials is an important design parameter since it influences energy consumption and the stability of supercurrents during thermal transients. This research aims to understand the factors that influence λ of epoxy-containing materials at low temperatures. An apparatus to measure λ from 4 to 30 K was constructed and is being used

[17]Work performed on assignment to Institut fur Experimentalle Kernphysik, Kernforschungzentrum, Karlsruhe, FRG, September 1978.

to study the effect of polymer cross-link spacing on λ of well-characterized epoxy resins and to investigate how Kapitza resistance might be minimized in two-phase epoxy systems.

3.2.2 Physical Properties of Metals

The paper, "Electron-Phonon Interaction and Lattice Thermal Conductivity," by W. H. Butler and R. K. Williams is reported in Sect. 1.1.2 of this report.

3.2.2.1 The Soret Effect in Molten Ag-Te Solutions[18] — R. K. Williams and W. O. Philbrook[19]

The Soret effect was studied in liquid Te solutions containing 17.5 to 69 at. % Ag. Measurements were obtained over a wide range of temperatures, and the factors affecting the experimental uncertainty are summarized. Thermodynamic data for the liquid solutions were reviewed and used to calculate experimental heat of transport, Q^*_{exp}, values. These Q^*_{exp} values decrease at high temperatures, and the possible relationships between this result and the thermoelectric properties of these semiconducting solutions are discussed.

3.2.2.2 Conduction in Niobium-Rich Alloys — J. P. Moore and R. S. Graves

The λ, thermal conductivity, of a commercially pure Nb (99.8% at. %) was measured from 100 to 1400 K. Results from 100 to 400 K were obtained by a longitudinal technique and results above 300 K were obtained in a new radial heat flow chamber. The results from the two techniques agreed to within ± 1.5% over the temperature range of overlap. We have noted previously that the electrical resistivities of Nb and Nb-rich alloys with W and Mo converge at high temperatures. The λ of Nb and Nb—10% W also converge at high temperature and are within 2% of each other above 1000 K. The Wiedemann-Franz ratios ($\lambda\rho/T$) for Nb and Nb—10% W are approximately constant at $1.05L_0$ and $1.02L_0$, respectively, above 300 K.

---

[18]Abstract prepared for submission to the *Journal of Applied Physics*; a portion of this work was conducted at Carnegie-Mellon University.

[19]Professor, Carnegie-Mellon University, Pittsburgh.

Existence of even a small contribution to the total λ from a lattice conduction component would indicate a Lorenz ratio near L_0.

3.2.2.3 Conduction in Silver-Palladium and Copper-Nickel Alloys — R. K. Williams, D. W. Yarbrough,[16] and R. S. Graves

Experimental values for λ, ρ, and S in the temperature range 300 to 1000 K have been obtained during the past year for the alloys 50 Cu–50 Ni and 50 Ag–50 Pd (at. %). The experimental data have been combined with a calculation[15] of the lattice component of the thermal conductivity to obtain λ_e. Values for the Lorenz function, L_e, were then obtained from measured electrical resistivities. Figure 3.2 compares the $L_e(T)$ resulting from the above analysis with $L_e(T)$ values published by Ho et al.[20] Our results indicate a modest positive deviation of $L_e(T)$ from the Sommerfield value for both the Cu-Ni and Ag-Pd alloys. The Cu-Ni data in addition tend toward the classical value at high temperature. These results are markedly different from the previously published data, primarily because of differences between λ values measured at ORNL and the λ values recommended in the literature by Ho et al.

3.2.2.4 Chromium — R. K. Williams, F. J. Weaver and R. S. Graves

Our analysis of λ data for high-purity Cr in the paramagnetic state indicates significant parallel phonon and electronic contributions. Others[21] hypothesize that the phonon contribution is negligible. Experimental values of λ, ρ, and S for Cr–1.07% Fe and Cr–0.56% Fe from 80 to 400 K have been obtained, and our initial analysis shows that phonon conduction is significant in Cr.

---

[20] C. Y. Ho, M. W. Ackerman, and K. Y. Wu, "Thermal Conductivity of Copper-Nickel and Silver-Palladium Systems," pp. 233–57 in *Thermal Conductivity* 14, ed. by P. G. Klemens and T. K. Chu, Plenum Press, New York, 1976.

[21] M. A. Mitchell and J. E. Goff, "Effect of Molybdenum and Vanadium on the Lattice Thermal Conductivity and Lorenz Number of Chromium," *Phys. Rev. B* 12: 1858–67 (1975).

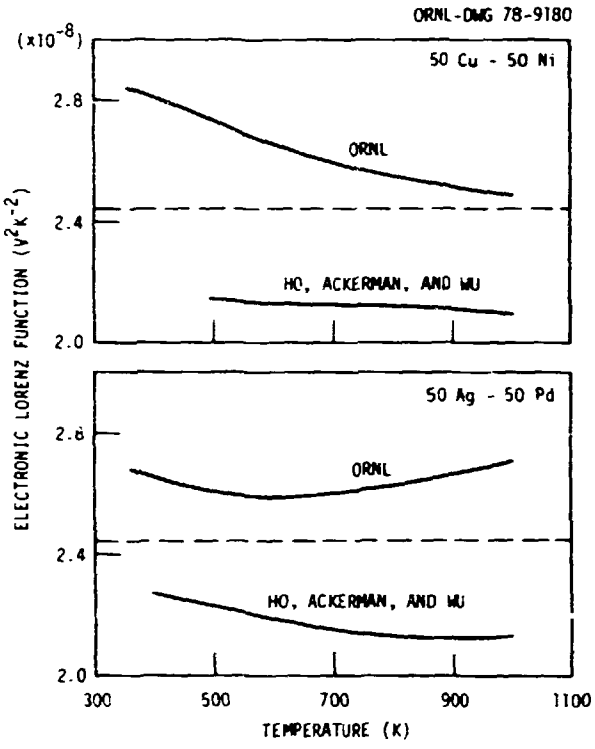

Fig. 3.2. Comparison of Electronic Lorenz Values for 50 Cu–50 Ni and 50 Ag–50 Pd (at. %) Alloys.

3.2.2.5 Properties of Experimental Alloys — R. S. Graves and D. L. McElroy

Physical property measurements were completed on several experimental alloys:

1. Heat-treated uranium-niobium alloys were suspected to undergo structural and compositional changes near room temperature that might be detectable by ρ measurements. However, our ρ data on alloys held at 21 and 50°C for 100 d indicated no changes greater than 0.02%.

2. The thermal conductivity of ordered and disordered Ni_4Mo was measured from 30 to 90°C. The ordered Ni_4Mo had a λ near 24 W/m K and the disordered Ni_4Mo was near 11 W/m K. This enhanced conduction appears to be due to the electronic component of the total λ.

3. Measurements of ρ (22°C) of ordered and disordered $V(Fe_{0.22}Co_{0.78})_3$ gave values of 0.61 and 0.81 $\mu\Omega$ m, respectively. These ρ values suggest smaller λ changes than observed for Ni_4Mo.

3.2.3 Properties of Solar Absorbers — J. P. Moore and D. W. Yarbrough[16]

Since solar flux on the earth's surface is low, selectively absorbing surfaces are needed for optimization of solar thermal systems, whether these are flat collectors or low-temperature concentrator systems. The total hemispherical emittance, THE, of good surfaces must be low to prevent loss of heat by radiation. Some of the best surfaces are fragile, and degradation may severely limit the surface lifetime. Any degradation would depend on the surface structure and degradation mechanism. Studies keyed to Auger spectroscopy, metallographic examination, reflectance in the infrared, and THE are being used to examine film structures.

Surfaces were prepared for THE measurements in an existing direct heating apparatus. The specimens were all fabricated by electrodeposition onto 0.127-mm-thick nickel strip. Copper was deposited onto the nickel followed by chromium metal or black chromium. The latter is used extensively as a solar surface, but it is fragile since absorption is due to a fine smut coating, which can be removed with the slightest touch. Some modifications had to be made to the existing technique because of the extremely low THE of most of the specimens and the low operation temperatures, which caused conductive end losses to exceed the radiative losses.

Results to date show that the THE of black chromium coatings are essentially constant at 0.083 from 300 to 510 K both before and after the smut coating is wiped off leaving a shiny gray metal. Although the black chromium surface will survive 480 K in air almost indefinitely, some degradation is apparent after only 7.2 ks at 580 K, and total destruction occurs after 7.2 ks at 650 K. Others have shown that black chromium will not remain stable above 570 K, and in this particular case the 580 K treatment apparently oxidizes the gray metallic material down to the copper layer, where thermal expansion differences cause spalling.

3.2.4 Graphite Thermal Conductivity Standards — J. P. Moore and R. S. Graves

A commercial grade of graphite has been proposed as an international thermal conductivity (λ) standard for high temperatures. Extensive

measurements of its thermal conductivity have been made by others at high temperatures, and our results from 80 to 900 K supplement these results. Over the temperature range of overlap the results from three techniques agreed to within ±2%. The λ versus temperature curve has a characterisic broad maximum near 300 K, and λ is related to ρ within 6% of the previously proposed[22] equation

$$\lambda = \frac{0.00156}{\rho} - \frac{0.266 \times 10^{-8}}{\rho^2} ,$$

where λ is in W/m K and ρ is in Ωm, both measured at 300 K.

3.3 SUPERCONDUCTING MATERIALS — D. M. Kroeger

We study the effects of metallurgical variables on the properties of superconducting materials. The superconducting property most structure sensitive appears to be current-carrying capacity in an applied magnetic field. It is affected by microstructural variables such as grain size, dislocation density and distribution, and morphology, composition, and volume fraction of second-phase particles. Meaningful correlation of structure and properties requires detailed knowledge of both. Consequently, some of our effort is devoted to obtaining basic metallurgical information on phase diagrams, transformation kinetics and products, and the microstructures that result from them in superconducting alloy systems. We correlate current-carrying capacity with the "model" microstructures.

Our laboratory has facilities to measure most superconducting properties of interest, such as critical current density, J_c, ac losses, superconducting-to-normal transition temperature, T_c, and upper critical field, H_{c_2}. We also measure low-temperature specific heat and effects of stress on superconducting properties.

---

[22] D. L. McElroy, T. G. Kollie, W. M. Ewing, R. M. Steele, and R. S. Graves. *Room Temperature Measurements of Electrical Resistivity and Thermal Conductivity of Various Graphites*, ORNL/TM-3477 (July 1971).

3.3.1 Flux Pinning by Grain Boundaries in Niobium Bicrystals[23] — A. DasGupta, Y. T. Chou,[24] C. C. Koch, and D. M. Kroeger

Bicrystals of niobium with symmetric tilt boundaries, grown directly from the melt with bicrystal seeds, have been used as a model system to measure the resistive critical current I_c as a function of the applied transverse magnetic field H and the angle, ϕ, between H and the grain boundary plane. The specimens were investigated in the as-received, chemically polished, and surface-oxidized states. Of these, the last condition brought out the true grain boundary contribution to I_c by suppressing the surface I_c. Extremely narrow peaks in $I_c(\phi)$ with half-intensity width $\leq 1°$ and heights up to 8 times the off-peak values were found for $\phi = 0$. The present results provide direct evidence of the efficacy of grain boundary pinning. The simplicity of the pinning system allows the elementary pinning force f_{pL} to be evaluated without the complications of statistical summation. Typically, $f_{pL} \simeq 7$ uN/m at $b = 0.67$ ($b = B/B_{c_2}$). From a consideration of the orientations of the grains, the possibility of grain boundary pinning occurring through the anisotropy of H_{c_2} is ruled out in our bicrystals. A calculation of the parelastic interaction between the grain boundary dislocations and the flux line lattice shows no pinning. Our results suggest the presence of an inhomogeneous layer at the grain boundary as the cause of the grain boundary flux pinning.

3.3.2 Flux Pinning by the First-Order Perturbation of Ginzburg-Landau Free Energy in Type II Superconductors[25] — A. DasGupta and D. M. Kroeger

For small pin size and variations in the superconducting order parameter $|\psi|^2$, the first-order perturbational approach of Campbell and Evetts can be taken to calculate the pinning force. Thus, variations of the upper critical field H_{c_2} and the Ginzburg-Landau parameter κ

---

[23]Abstracted from a paper presented at the International Cryogenic Materials Conference, Boulder, Colo., August 1977, and a paper to be published in *Philosophical Magazine*.

[24]Lehigh University, Bethlehem, Pa.

[25]Abstracted from a paper presented at the March Meeting of the American Physical Society, Washington, D.C., March 1978.

were considered and combined to obtain the interaction energy, E_{int}, between fluxoid lattice (FLL) and pin. The interaction energy is proportional to $\kappa_1^2(1 - \kappa_2^2)$. Its spatial variation was studied in a plane perpendicular to the fluxoid. Three sets of stationary points are found for $E_{int}(b = B/B_{c2})$ in the FLL. The elementary pinning force f_p scales with b; it shows a minimum at $b = 0.3$ and a maximum at $b = 0.65$. Comparisons have been made with data from the literature. The good agreement indicates that this mechanism of flux pinning may be operative in a wide variety of pinning systems.

3.3.3 Recent Developments in Fluxoid Pinning and Stress Effects in Superconductors[26] — C. C. Koch

Critical current density, J_c, is the most structure-sensitive parameter that limits the application of superconductors in practical devices. It is dramatically influenced by the metallurgical structure. Applied stress under operating conditions can also influence — in most cases degrade — J_c. This review discusses some of the recent developments in understanding fluxoid pinning in both hard superconductors and model materials. Mechanical effects on J_c were also reviewed.

3.3.4 Effect of Nb_3Sn Layer Thickness and Kirkendall Voids on Multifilamentary Nb_3Sn Conductors[27] — D. S. Easton and D. M. Kroeger

The effects of varying the reaction time, and hence the Nb_3Sn layer thickness, on the mechanical and superconducting properties of a multifilamentary Nb_3Sn conductor have been studied. The conductor contained 1369 niobium filaments with a bronze-to-superconductor ratio of 3.4. As a consequence of varying the reaction time, each conductor behaved differently because of (1) Kirkendall voids produced in the matrix by the diffusion of tin; (2) depletion of tin in the matrix;

---

[26] Invited review presented at the 1977 TMS-AIME Fall Meeting, Chicago, October 1977.

[27] Abstracted from papers presented at the International Cryogenic Materials Conference, Boulder, Colo., August 1977, and at the TMS-AIME Fall Meeting, Chicago, October 1977.

(3) changes in the thermal expansion coefficients of both matrix and filaments; (4) mechanical property changes, particularly the yield stress of the matrix and the modulus of the filament; (5) a volume expansion of the filament; and (6) a change in the ratio of normal conductor to superconductor as a result of the volume change. Increases in Kirkendall voids with reaction time are shown in photomicrographs and analyzed by the use of quantitative television microscopy. We suggest that these voids produce thermal and electrical instabilities as well as decreased ductility. Calculations of the residual stress state were made taking into account the above changes. The applied strain at maximum J_c correlates with the calculated residual compressive strain only for the thin layered materials, apparently because of unequal stress concentrations when a large number of voids is present.

3.3.5 Causes of Strain Sensitivity of Critical Current in Nb_3Sn Conductors[28] — D. M. Kroeger, D. S. Easton, A. DasGupta, and J. O. Scarbrough

Measurements were made of $H_{c_2}(T)$, T_c, and J_c as functions of strain, ε, for both mono- and multifilamentary Nb_3Sn diffusion-processed conductors. Results for the two types of material are essentially similar, but because the matrix-to-filament ratio is much larger in the monofilament material, the prestrain due to differences in thermal contraction upon cooling to T_c is much greater than in the multifilament material. Therefore, the observed changes in T_c, H_{c_2}, and J_c upon application of tensile stress are larger, making this an easier material to study. For the monofilament material, $H_{c_2}(T)$ and $J_c(T)$ (for $T_c/2 < T < T_c$) and T_c were measured as functions of strain simultaneously in the same apparatus to avoid uncertainties arising from differences among specimens and calibrations of stress or strain measurements. A linear relationship was found between $J_c(H, T, \varepsilon)$ and the condensation energy at (H, T, ε) as determined by the measured values of $(dH_{c_2}/dT)_{T_c}$ and T_c. We concluded that J_c is affected by strain primarily

[28]Papers based on this work have been presented at the International Cryogenic Materials Conference, Boulder, Colo., August 1977, and at the TMS-AIME Fall Meeting, Chicago, October 1977.

through changes in the fundamental superconducting properties H_{c2} and T_c rather than through changes in microstructure.

3.3.6 Cryogenic Mechanical Properties of Solder Joints in a Niobium-Titanium Superconductor[29] — A. J. Moorhead,[30] J. J. Woodhouse,[30] and D. S. Easton

Although many alternate techniques are being studied for joining of superconductor composites (e.g., ultrasonic, electron beam, explosion, and resistance spot welding), at this time soldering is still the most common. Soldering has the advantages of requiring limited capital investment for equipment or facilities, is amenable to making joints in situ, and is a simple, familiar process to fabrication personnel. However, we have found a notable lack of published data on the mechanical properties of solder joints at cryogenic temperatures.

We determined the wetting and flow behavior of various solder and flux combinations on a copper-clad Nb-Ti composite, developed equipment and techniques for soldering and inspection of lap joints, and determined the shear strength of joints at temperatures down to −269°C (4 K). We studied 15 solders and 17 commercial and experimental fluxes in the wettability and flow tests. A resistance unit was built for soldering test specimens. Samples soldered with 80 Pb–20 Sn, 83 Pb–15 Sn–2 Sb, 97.5 Pb–1.5 Ag–1 Sn, 80 In-15 Pb–5 Ag, or 25 In–37.5 Pb–37.5 Sn (wt %) were inspected by three nondestructive techniques. Through-transmission ultrasound gave the best correlation with nonbond areas revealed in peel tests. Single lap shear specimens soldered with 97.5 Pb–1.5 Ag–1 Sn had the highest strength (72 MPa, 10.4 ksi) and total elongation of four solders tested. Discontinuous yielding was found in some cases. This effect could produce local temperature rises that could affect the performance of magnetic devices.

---

[29]Abstracted from a paper presented at the International Cryogenic Materials Conference, Boulder, Colo., August 1977, and from a paper "Soldering of Copper-Clad Niobium-Titanium Superconductor Composites," *Weld. J. (Miami)* 56: 23–31 (1977).

[30]Welding and Brazing Group, Metals and Ceramics Division.

3.3.7 Differentiation and Characterization of Type-II Superconductors via Synthesis of Observed Induced Voltage Waveforms — D. J. Griffiths[31] and D. M. Kroeger

Induced voltage waveforms exhibited by type-II superconductors in response to a time-varying magnetic field superimposed on a steady dc magnetic field have been calculated by use of a modification of a computer program developed by Rouse and Clem. The program allows a choice of critical state model, equilibrium magnetization function, field-dependent entry and exit barriers, and the specific form of the time-dependent magnetic field. The objective of the work is to be able to develop a method of generating waveforms whose shapes are sensitive to the collection of models chosen and, thereby, characterize the superconductor both qualitatively and quantitatively within the framework of the critical state concept.

Once agreement between predicted and observed waveforms has been achieved ac losses and their dependence on both dc bias field and time-varying field amplitude can be generated. It is hoped that this program will allow consistent predictions of the loss behavior of type-II superconductors based on the examination of a few carefully chosen induced voltage waveforms and, thus, lead to a simple method of classifying most available superconductors.

---

[31] Oregon State University, Corvallis.

4. RADIATION EFFECTS

J. O. Stiegler and K. Farrell

The Radiation Effects Program has as its goal the understanding of changes in the physical and mechanical properties of metals and alloys resulting from elevated-temperature neutron irradiation. The work is focused on studying the effects of composition and microstructure since these may be used to minimize or control the property changes. Although the objective of the program is an understanding of the effects of neutron irradiation, simulation techniques that allow accelerated testing and evaluation of mechanisms are exploited. Both experimental and theoretical approaches are employed. Since understanding the property changes requires an ability to describe composition and microstructure at the atomic level, a substantial effort has been mounted to develop and utilize analytical and high-resolution electron microscopy techniques. The development of a nuclear microanalysis capability based on the accelerators operated by the group has also been initiated.

Work on this program complements the radiation effects activities in the ORNL Solid State Division, which are directed at understanding the primary production of defects by particle irradiation. The effort in the Metals and Ceramics Division is concerned with the organization of these defects into more complex configurations and with the properties of materials after large irradiation exposures. This work parallels applied programs in the Metals and Ceramics Division, but is aimed at describing the mechanisms of damage production and property changes through the study of simple or model systems. Through such activities we hope to broaden the foundation upon which the alloy development efforts of the applied programs are based.

4.1 THEORETICAL STUDIES

4.1.1 General Rate Theory Model of Void Swelling and Dislocation Loop Growth in Irradiated Metals — M. H. Yoo, L. K. Mansur, and W. A. Coghlan

In order to develop a generalized rate theory model of void swelling in metals under irradiation by fast neutrons or by high-energy charged particles, the usual assumptions listed below must be closely examined for their validity:

1. quasi-steady-state defect concentrations,
2. homogeneous distribution of defects,
3. spatially uniform loop and void sizes,
4. spatially uniform defect generation rate,
5. no mobile defects other than vacancies and interstitials,
6. constant recombination volume,
7. constant capture efficiencies of internal sinks, and
8. evolution of dislocation microstructure estimated simply by a dose-dependent dislocation density.

A system of rate equations for the growth of interstitial dislocation loops and voids in one-dimensionally bounded media, namely the semi-infinite medium and the foil, under charged-particle irradiation has been formulated, and a numerical method of integrating the rate equations has been presented.[1] In this model the first four assumptions are eliminated altogether. The extent to which this model has been generalized with respect to the other assumptions is:

5. for nickel, divacancies contribute to void swelling and loop growth in the temperature range from 100 to 400°C (375–675 K), but have little effect at higher temperatures;

---

[1]M. H. Yoo, "Dislocation Loop Growth and Void Swelling in Bounded Media by Charged Particle Damage," *J. Nucl. Mater.* 68: 193–204 (1977), ORNL/TM-5789 (April 1977).

6. the temperature dependence of the recombination volume has been calculated and is used;[2]
7. the size and temperature-dependent capture efficiency of dislocation loops (Sect. 4.1.6 of this report) is accounted for; and
8. the effects of unfaulting and mutual entanglement of Frank loops on void swelling are included in the model.[3]

In addition, for the case of self-ion irradiation, the model has been extended to include the effects of deposited self-ions[4] and also those of a thermal nucleation of defect clusters in displacement cascades.[5] This general model will be applied to correlation studies of void swelling by self-ion and neutron irradiation and to the interpretation of void swelling data obtained by step-height measurements and transmission electron microscopy.

4.1.2 Theory of Impurity Trapping of Point Defects and Its Effects on Irradiation-Induced Swelling and Creep[6] — L. K. Mansur and M. H. Yoo

Early experimental studies to characterize irradiation-induced void swelling revealed that impurity and alloy additions in a metal strongly affect its propensity to swell. It was proposed that trapping of point defects by solutes increases the

---

[2]M. H. Yoo and W. H. Butler, "Steady-State Diffusion of Point Defects in the Interaction Force Field," *Phys. Status Solidi* (b) 77: 181–93 (1976).

[3]M. H. Yoo and L. K. Mansur, "General Rate Theory Model of Void Swelling in Irradiated Metals," *Trans. Am. Nucl. Soc.* 27: 326–27 (1977).

[4]A. D. Brailsford and L. K. Mansur, "Effect of Self-Ion Injection in Simulation Studies of Void Swelling," *J. Nucl. Mater.* 71: 110–16 (1977); see also Sect. 1.1.14 of this report.

[5]R. Bullough, B. L. Eyre, and K. Krishan, "Cascade Damage Effects on the Swelling of Irradiated Materials," *Proc. R. Soc. (London)* A346: 81–102 (1975).

[6]Summary of L. K. Mansur and M. H. Yoo, "The Effects of Impurity Trapping on Irradiation Induced Swelling and Creep," *Journal of Nuclear Materials*, in press.

fraction of vacancies and interstitials undergoing mutual recombination, thus reducing the fraction flowing to voids. We have developed a comprehensive theory to describe the effects of solute trapping upon radiation-induced deformation processes. Both vacancy and interstitial trapping at a multiplicity of traps and the effects of point defect trapping on void nucleation, void growth, and irradiation creep have been considered. The equations explicitly include spatial inhomogeneity and time dependence. The correction due to exclusion of sites near traps of free vacancies becomes important when the trap concentration is of the order of 1%. The traps are described by their concentration, trapping radius, capture radius for a free defect when the opposite type defect is trapped, and binding energy for point defects. These parameters may be varied to include solute atoms, solute atom clusters, or precipitates as traps.

Trapping can be viewed in terms of effective recombination or diffusion coefficients, and expressions for these effective coefficients are derived. The general result — that vacancy trapping is effective in reducing swelling and creep at relatively small binding energies but that interstitial trapping is effective only if the binding energy exceeds approximately the difference in the migration energies of free vacancies and interstitials — can be understood in terms of effective diffusion coefficients.

Point defect trapping increases the fraction of defects recombining in the matrix at the expense of those diffusing to sinks and thereby decreases the concentration of free point defects. With respect to void nucleation, void growth, and irradiation creep, trapping is predicted to be most effective in decreasing the void nucleation rate. The next largest effect of trapping is on void growth rate and to exactly the same degree on the climb-glide creep rate. The smallest effect is on the stress-induced preferential absorption dislocation climb mechanism of irradiation creep. The effects predicted are illustrated primarily as functions of binding energy, trap concentration, temperature, and dose rate for parameter ranges of interest. In the figures shown below, the largest vacancy binding energy is 0.5 eV and the largest interstitial binding energy is 1.7 eV. The results for these binding energies

and for no trapping form an envelope that should give reasonable upper and lower limits for the possible effects of point defect trapping. Figure 4.1 shows the fraction of defects recombining in the matrix — that is, not being removed at sinks — as a function of temperature, dose rate, and solute concentration. The change in fraction recombining with increasing solute concentration is more pronounced for reactor conditions than for charged particle conditions.

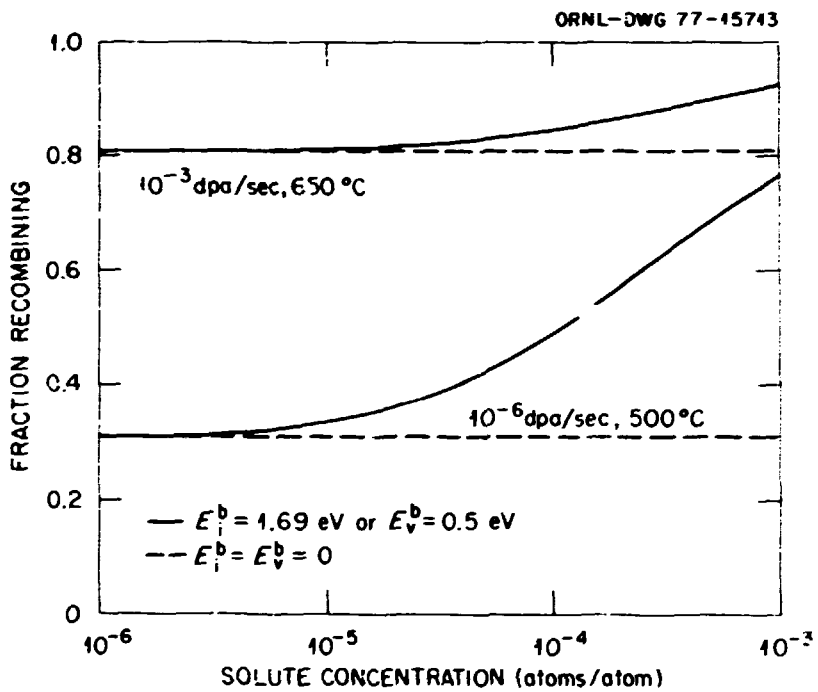

Fig. 4.1. Fraction Recombining Versus Solute Concentration with no Trapping and with Either Vacancy Trapping at E_v^b = 0.5 eV or Interstitial Trapping at 1.7 eV. Results for both typical charged particle and fast reactor dose rates and temperatures are given. Trapping becomes effective at smaller solute concentrations and produces a larger increase in the fraction recombining for reactor conditions.

Figures 4.2 and 4.3 display the effects of point defect trapping on void nucleation and void growth. The results in Fig. 4.2 show the free energy of void nucleation, and the corresponding nucleation rates are given in the figure caption. Figure 4.3 gives the results for void growth. The upper set of curves in each figure displays the effects of vacancy trapping and the lower set interstitial trapping.

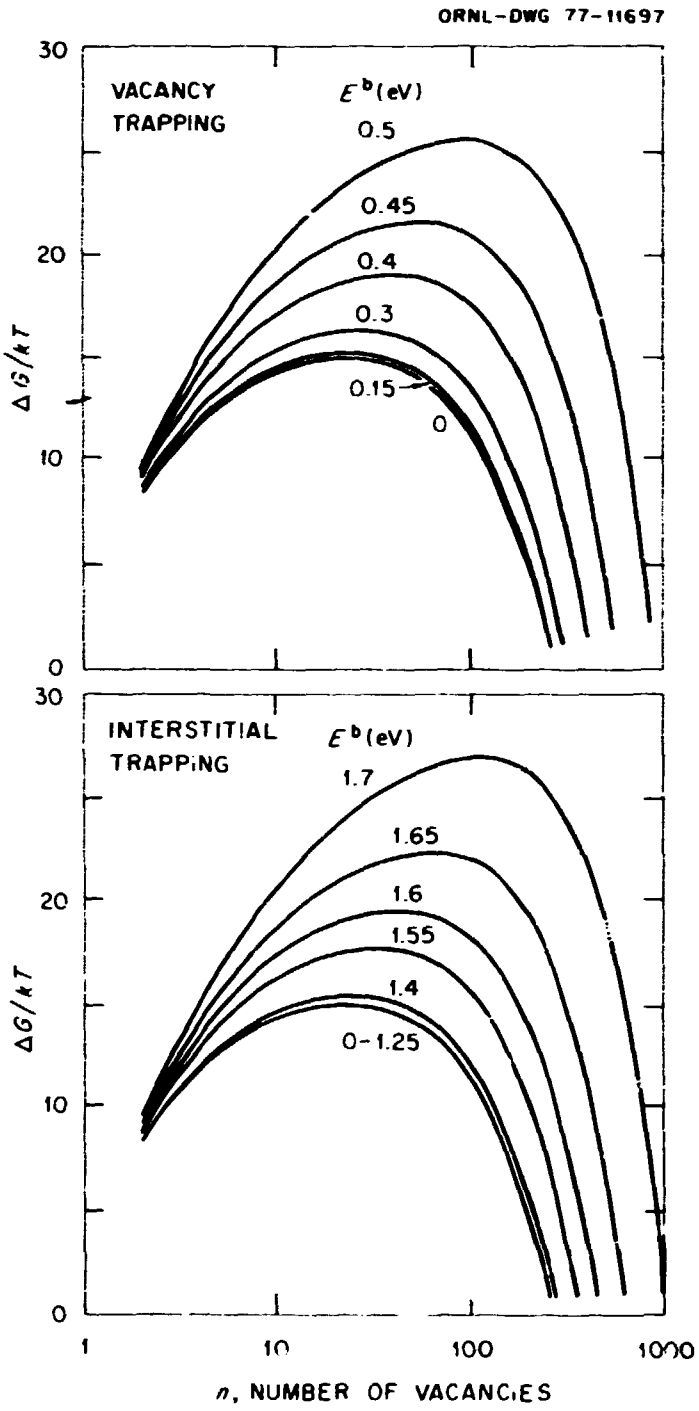

Fig. 4.2. The Effect of Impurity Trapping on the Free Energy of Void Nucleation. The nucleation rates (in nuclei per second) calculated from the curves as a function of binding energy (E_b) in eV are: Vacancy trapping: E_b = 0, 1.5 x 10^{12}, E_b = 0.3, 2.2 x 10^{11}; E_b = 0.4, 6 x 10^9; E_b = 0.5, 1.8 x 10^6. Interstitial trapping: E_b = 1.25, 1.4 x 10^{12}; E_b = 1.4, 8 x 10^{11}; E_b = 1.6, 2.9 x 10^9; E_b = 1.7, 3.5 x 10^5. Below nucleation rates of about 10^{10}/s in a typical ion bombardment experiment, voids will not be observable.

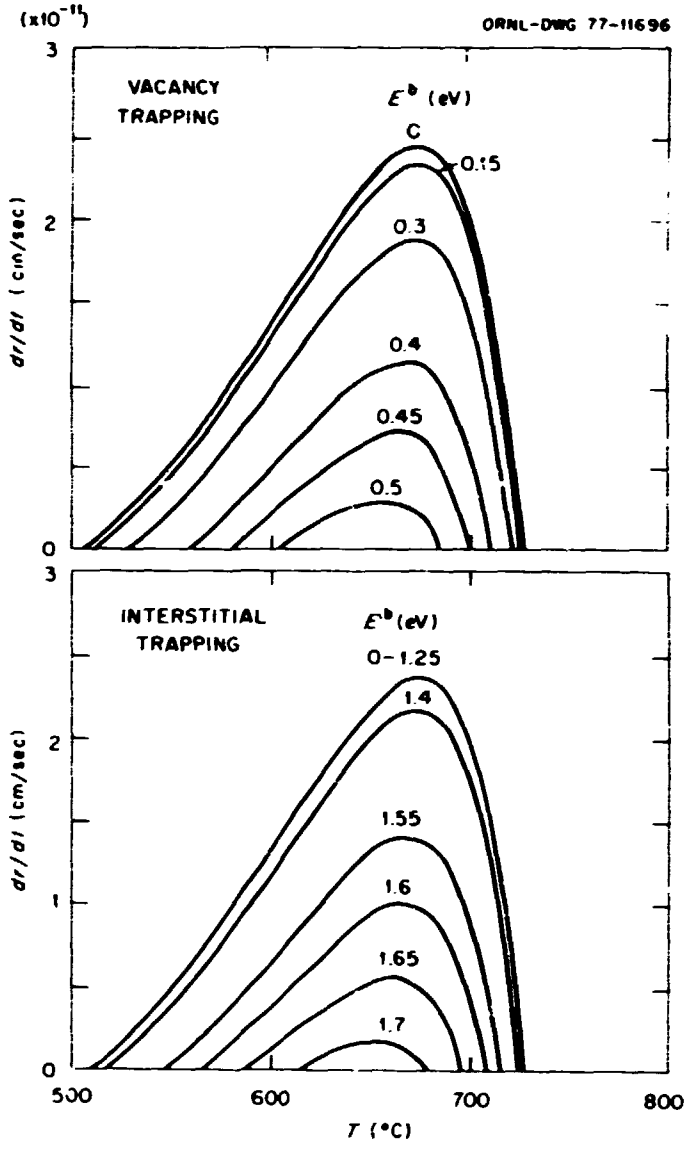

Fig. 4.3. The Effect of Impurity Trapping on Void Growth Rates.

Both interstitial and vacancy trapping produce strong reductions in swelling. To produce the same reduction in nucleation or growth rate, the binding energy required for the vacancy is much less than that for the interstitial.

Trapping reduces both the void nucleation and growth rates, with the reduction in nucleation rate by far exceeding the reduction in growth rate for a given binding energy. The nucleation rate decreases with increase in binding energy as a result of increases in both the size and free energy of the critical nucleus.

The well-known qualitative relation between increasing solute content and reduction in swelling is confirmed. From Fig. 4.1 we see, for example, that point defect trapping, even with reasonably large binding energies, is expected to have little effect if the solute concentrations are below about 10 ppm. (For smaller binding energies the level would be approximately 1000 ppm.) If a significant effect of impurities at this level is found experimentally, point defect trapping cannot be the operative mechanism. The theory predicts less sensitivity of irradiation creep to solute content, a trend that is qualitatively borne out by experiment.

4.1.3 The Reduction of Irradiation-Induced Creep Rate by Point Defect Trapping at Solutes and Vacancy Loops[7,8] — L. K. Mansur, M. H. Yoo, and W. G. Wolfer[9]

The dislocation climb creep rate is given by

$$\dot{\varepsilon} = \frac{2\Omega L}{9}\left(\Delta Z_i^d D_i C_i - \Delta Z_v^d D_v C_v\right), \qquad (1)$$

where subscripts i and v denote interstitials and vacancies, Ω is the atomic volume, L is the dislocation density, D is the diffusion coefficient, C is the free point defect concentration, and ΔZ_i^d is the difference in capture efficiency for interstitials of dislocations oriented parallel and perpendicular to the stress axis. The corresponding difference for vacancies, ΔZ_v^d, is small and thus the second term in Eq. (1) may be neglected. The creep rate is then proportional to the free interstitial concentration. The reduction in the free interstitial population by point defect trapping therefore determines the reduction in creep rate.

---

[7] A summary of work described in L. K. Manusr and M. H. Yoo, *Journal of Nuclear Materials*, in press; ORNL/TM-6134 (December 1977).

[8] L. K. Mansur and W. G. Wolfer, "The Reduction of Irradiation-Induced Creep by Point Defect Trapping," presented at the ASTM Symposium Effects of Radiation on Structural Materials, Richland, Wash., July 1978, and to be published in the proceedings.

[9] Department of Nuclear Engineering, University of Wisconsin, Madison.

The effects of point defect trapping at solutes on the dislocation climb creep rate have been explored with a range of variables of experimental interest. It is also shown that vacancy loops, generated by the collapse of cascades, may be included in the formalism together with point defect trapping at solutes. The effect of these vacancy loops on the creep rate is shown to be mathematically equivalent to a simultaneous reduction in the point defect generation rate, the free point defect recombination coefficient, and the capture coefficient of solute traps for free vacancies by the factor K_i^0/K_i in the equations that apply to a system without vacancy loops. This factor is the ratio of the sink strength for interstitials of all sinks except the vacancy loops to the sink strength for interstitials of all sinks. The combined effects of solute trapping and vacancy loops on the creep rate under several conditions are illustrated below. The reduction of the creep rate due to both solute trapping and vacancy loops is never found to be more than an order of magnitude in the parametric range explored here. This work is described in detail in ref. 8.

Figure 4.4 shows the reduction in creep rate as a function of solute concentration for typical reactor and charged particle dose rates and temperatures. We note that at the highest solute level the effect of trapping is to reduce the creep rate a factor of about 5 for charged particle and about 2 for reactor conditions. Reactor creep simulation by charged particles usually takes place near reactor dose rates and temperatures. However, it is interesting to find that at the much higher dose rates and temperatures where swelling simulation takes place (the high-dose-rate, high-temperature case of Fig. 4.4) the creep rate is expected to be more strongly reduced by trapping.

Figure 4.5 displays the effects of vacancy trapping and vacancy loops on creep rate at a typical dose rate and temperature for reactor irradiations. The relative creep rate is plotted as a function of K_i^{vl}/K_i^0, the ratio of vacancy loop sink strength for interstitials to that for all sinks excluding vacancy loops. Without trapping, the reduction in creep rate is substantial at large vacancy loop sink strengths, about a factor of 5. However, with trapping, the further reduction in creep rate due to vacancy loops is modest. For vacancy

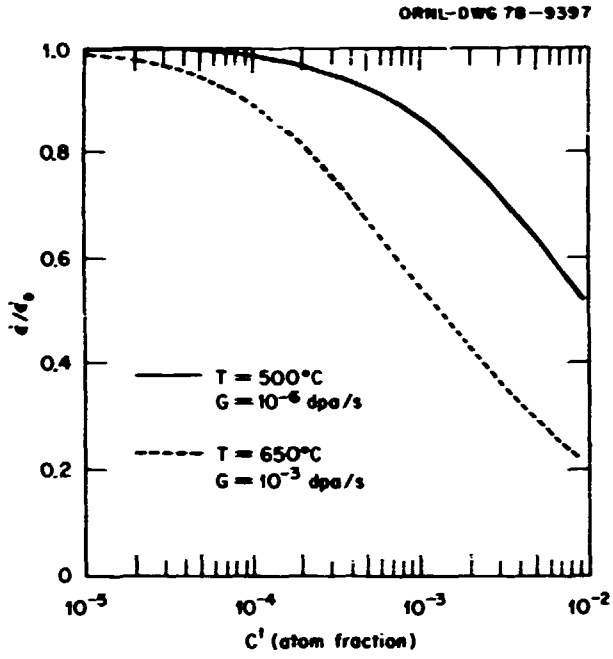

Fig. 4.4. Effect of Trapping on the Creep Rate with Increasing Solute Content. Solid curve is typical for reactor irradiation and dotted curve is typical for charged particle bombardment.

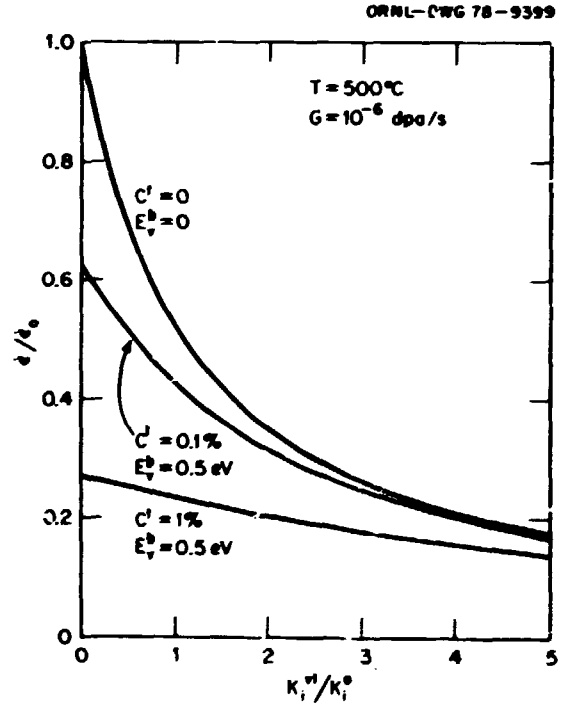

Fig. 4.5. Combined Effect of Trapping and Vacancy Loops on the Creep Rate as a Function of the Vacancy Loop Sink Strength for Interstitials, Normalized to the Sink Strength for All Other Sinks Under Typical Reactor Irradiation Conditions.

trapping with a binding energy of 0.5 eV and solute concentration of 1%, the additional reduction in the creep rate due to vacancy loops is less than a factor of 2 for vacancy loop sink strength ratio $K_i^{vl}/K_i^0 \leq 5$. These curves illustrate that as the vacancy loop sink strength increases the effect of trapping becomes less important. As the sink strength is increased the loss rate of interstitials by recombination with both free and trapped vacancies is decreased, and in the limit of large K_i^{vl}/K_i^0 the curves with free recombination (upper curve) and with free and trapped recombination (lower two curves) should approach each other since they also must approach the same value that would be obtained by neglecting recombination and trapping altogether.

Two conclusions may be based on these findings:

1. Creep rates are not expected to be greatly different in alloys with differences in solute content and binding energy — that is, chemical identity — of solutes at the levels of order 1%.

2. The possibly different steady-state vacancy loop distributions, resulting from neutrons on the one hand and the charged particles used to simulate reactor irradiation-induced creep on the other hand, are not expected to produce greatly different creep rates.

4.1.4 The Temperature Shift of Swelling with Changes in Radiation Dose Rate[10] — L. K. Mansur

The temperature region of void swelling shifts when the radiation dose rate is changed. Of particular interest is the shift that occurs between reactor irradiations and charged particle bombardments using the Oak Ridge 5-MV Van de Graaff, where the dose rates differ by three to four orders of magnitude. The work described here predicts from theory the temperature shifts to be expected under arbitrary changes in dose rate. The work has been used to support the analyses of temperature shift in pure nickel performed by Packan et al.[11]

---

[10] A summary of L. K. Mansur, "Correlation of Neutron and Heavy-Ion Damage: Part II, The Temperature Shift of Swelling with Changes in Radiation Dose Rate," *Journal of Nuclear Materials*, in press.

[11] N. H. Packan, K. Farrell, and J. O. Stiegler, "Correlation of Neutron and Heavy-Ion Damage: Part I, Influence of Dose Rate and Injected Helium on Swelling in Pure Nickel," *Journal of Nuclear Materials*, in press.

The full theory[12] for swelling rate as a function of materials and irradiation variables, including temperature and dose rate, forms the basis of this work. Swelling rate may be obtained as a function of temperature at a fixed dose rate. At a different dose rate the theory gives a different profile of swelling rate versus temperature. By comparing these results, a temperature shift for the given change in dose rate is determined. This analysis has been used[11] to give a theoretical temperature shift of 201°C where the measured value was 200°C.

Under limiting conditions, which bracket the ranges of experimental interest, explicit analytical expressions for temperature shift may be obtained. Derivations have been performed for cases where either point defect recombination or absorption at sinks is the dominant point defect loss process, where both vacancy and interstitial absorption at voids is surface-reaction- or diffusion-controlled, or where the interstitial is surface-reaction-controlled while the vacancy is diffusion-controlled.

The general result may be expressed as:

$$T^{(2)} - T^{(1)} = \frac{\dfrac{kT^{(1)2}}{E_v^m + n(E_v^f + E_v^*)} \left[\ln \dfrac{G^{(2)}S_i^{(1)}S_v^{(1)}}{G^{(1)}S_i^{(2)}S_v^{(2)}} + \ln R\right]}{1 - \dfrac{kT^{(1)}}{E_v^m + n(E_v^f + E_v^*)} \left[\ln \dfrac{G^{(2)}S_i^{(1)}S_v^{(1)}}{G^{(1)}S_i^{(2)}S_v^{(2)}} + \ln R\right]} , \quad (2)$$

where the value of $n = 1$ for sink dominated cases and $n = 2$ for recombination dominated cases, while the value of R is determined by both the dominant process and the mode of void growth. Table 4.1 gives the values of R. In the table, E_v^* is the additional energy barrier at the void surface in the surface-reaction-controlled case. Only for the first row of Table 4.1 E_v^* has a nonzero value, since only there the vacancy absorption

---

[12] L. K. Mansur, "Void Swelling in Metals and Alloys Under Irradiation: An Assessment of the Theory," *Nuclear Technology*, in press.

Table 4.1. Expressions for the Dose-Rate Dependence of Temperature Shift under Various Limiting Conditions of Point Defect Removal[a]

Mode of Absorption at Voids	Value of R in Eq. (2) when Dominant Process of Point Defect Removal is by	
	Recombination ($n = 2$)	Sinks ($n = 1$)
Interstitial and vacancy both reaction controlled	$\frac{r_c^{(1)}}{r_c^{(2)}} \left[\frac{S_i^{(2)} \exp\left(-E_v^*/kT^{(2)}\right) - S_v^{(2)} \exp\left(-E_i^*/kT^{(2)}\right)}{S_i^{(1)} \exp\left(-E_v^*/kT^{(1)}\right) - S_v^{(1)} \exp\left(-E_i^*/kT^{(1)}\right)} \right]^2$	$\frac{L^{(2)}}{L^{(1)}} \left[\frac{Z_i^d \exp\left(-E_v^*/kT^{(2)}\right) - Z_v^d \exp\left(-E_i^*/kT^{(2)}\right)}{Z_i^d \exp\left(-E_v^*/kT^{(1)}\right) - Z_v^d \exp\left(-E_i^*/kT^{(1)}\right)} \right]$
Interstitial and vacancy both diffusion controlled	$\frac{r_c^{(1)}}{r_c^{(2)}} \left[\frac{L^{(2)}}{L^{(1)}} \right]^2$	$\frac{L^{(2)}}{L^{(1)}}$
Interstitial reaction, vacancy diffusion controlled	$\frac{r_c^{(1)}}{r_c^{(2)}} \left[\frac{bS_i^{(2)} - S_v^{(2)} r_v \exp\left(-E_i^*/kT^{(2)}\right)}{bS_i^{(1)} - S_v^{(1)} r_v \exp\left(-E_i^*/kT^{(1)}\right)} \right]^2$	$\frac{L^{(2)}}{L^{(1)}} \left[\frac{bZ_i^d - r_v Z_v^d \exp\left(-E_i^*/kT^{(2)}\right)}{bZ_i^d - r_v Z_v^d \exp\left(-E_i^*/kT^{(1)}\right)} \right]$

[a]The parameters r_c, L, b, Z^d denote the radius of point defect recombination volume, the dislocation density, an atomic dimension, and the capture efficiency of dislocaions for point defects. Superscript (1) denotes value for reactor irradiation, (2) for charged-particle bombardment.

is assumed to be reaction controlled. The superscripts (1) and (2) denote the two conditions reactor irradiation and charged-particle bombardment, k is Boltzmann's constant, E^m is the point defect migration energy, E^f is the formation energy, T is the temperature, G is the radiation-induced point defect generation rate, and S is the sink strength of all sinks such as voids, dislocations, and grain boundaries for point defects.

The dominant process of point defect loss as well as the mode of void growth affects the detailed form of the temperature shift expression. When recombination dominates, the expression contains the ratio of the radii of recombination volumes at the two different temperatures in addition to the ratios of sink strengths. This occurs because a change in this parameter changes the recombination rate and hence the flux to voids. Also when recombination dominates, the temperature shift is smaller since $2E_v^f$ occurs in the denominator, whereas only E_v^f occurs when sinks dominate. The physical reason for this is that the radiation-induced void growth rate is proportional to the generation rate when sinks dominate, while it is proportional to the square root of the generation rate when recombination dominates.[12] However, the thermal shrinkage rate depends on the same exponential in temperature in both cases. Thus, a given initial ratio of thermal shrinkage rate to radiation-induced growth rate of voids may be recovered after a given increase in dose rate by a smaller increase in temperature where recombination dominates.

From Table 4.1 we see by comparing the first row (reaction controlled) with the second row (diffusion controlled) that the temperature shifts predicted for these cases are not greatly different. In Eq. (2) the main difference comes in the fact that $E_v^* + E_v^f$ multiplies n in the pre-logarithmic term for reaction-controlled void growth, while E_v^f multiplies n in the diffusion-controlled case. Since $E_v^f > 1$ eV and $E_v^* \approx 0.1$ eV, this produces a small difference in the temperature shift. This is to be compared with the very large differences possible in the dose kinetics of void growth for these two modes of void growth.[12]

4.1.5 Stress-Assisted Diffusion Bias for Prismatic Dislocation Loops[13] — W. A. Coghlan and M. H. Yoo

Dislocation loops are almost always the first observable defect in materials undergoing irradiation. Radiation damage models inadequately treat the growth of these loops because the defect interaction with these loops is complicated and the resulting diffusion problem does not have an analytical solution. Previous solutions[14,15] have used an infinitesimal approximation for the dislocation loop, which is strictly valid only for very small loops. In addition, the resulting diffusion flux depends very strongly on the choice of the cutoff radius for the core boundary condition.

We have numerically solved the problem of diffusion of vacancies and interstitials to faulted dislocation loops.[16] We have overcome both the problem of the complicated interaction energy profile and the problem of the inner boundary cutoff.

The interaction of the defect with the stress field is described by the Eshelby model and includes both the size interaction and the modulus interaction. The steady-state defect profile in a cylinder containing a torus around the loop is based on the solution[17] of

$$\frac{\partial C}{\partial t} = \nabla \cdot \left(D \nabla C + \frac{DC \nabla E}{kT} \right) = 0 , \qquad (3)$$

---

[13]Summary of a paper presented at the American Nuclear Society Winter Meeting, November 27–December 2, 1977 in San Francisco.

[14]M. H. Yoo and W. H. Butler, "Steady-State Diffusion in the Interaction Force Field," *Phys. Status Solidi (b)* 77: 181–93 (1976).

[15]W. G. Wolfer and M. Ashkin, "Stress-Induced Diffusion of Point Defects to Spherical Sinks," *J. Appl. Phys.* 46: 547–57 (1975).

[16]W. A. Coghlan "Transient and Steady State Diffusion Solution for Point Defects in a Stress Field," pp. 166–76 in *Proc. Conf. Computer Simulation for Materials Application*, ed. by R. J. Arsenault, J. I. Beeler, and J. A. Simmons, Gaithersburg, Md., 1976.

[17]F. S. Ham, "Stress-Assisted Precipitation on Dislocations," *J. Appl. Phys.* 30: 915–26 (1959).

where

C = the defect concentration,

t = the time,

D = the diffusion coefficient,

E = the interaction energy,

k = the Boltzmann constant, and

T = the absolute temperature.

The flux of defects is found at steady state by numerical integration over a surface surrounding the loop. The results can be expressed in several convenient ways. First, the ratio of the actual defect flux to the flux in the absence of an interaction can be calculated. This ratio, normally called Z (the capture efficiency), has been used extensively in radiation damage models. Another convenient way for illustrating the results is to determine the radius of an equivalent spherical sink. This method results in the effective capture radius, r^*, and the defect flux can be determined from

$$J = 4\pi D r^* (\bar{C} - C_b) \ , \qquad (4)$$

where C is the concentration at the outer boundary and C_b is the concentration at the dislocation core. A different capture radius can be calculated by excluding the stress interaction, and the ratio of these capture radii equals Z.

The choice of the core cutoff radius is simplified by the observation that the defect flux becomes independent of this parameter when the product of the defect jump length b and magnitude of the interaction gradient DE is greater than kT. This somewhat surprising result is shown in Fig. 4.6 for several cases. Another useful result is that the surfaces representing constant values of $|\nabla E| b/kT$ are nearly perfect toroids around the dislocation loop. The core radius chosen is the average radius of nearly circular cross sections.

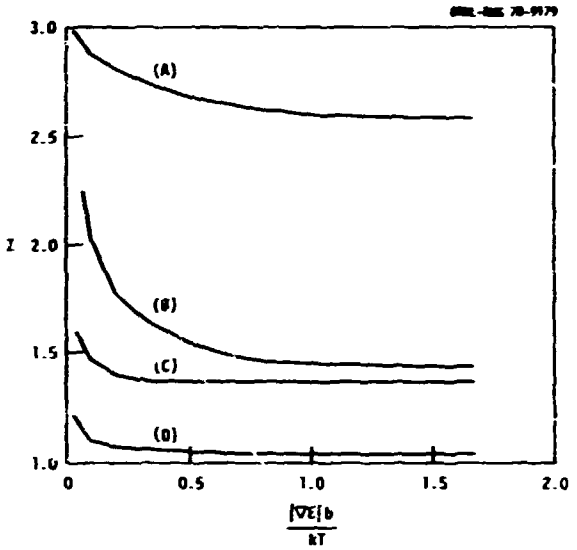

Fig. 4.6. The Dependence of the Capture Efficiency, Z, on the Magnitude of the Interaction Energy Gradient for Several Interstitial Dislocation Loops. A: Interstitials diffusing to a $20b$-radius loop; B: interstitials diffusing to a $200b$-radius loop; C: vacancies diffusing to a $20b$-radius loop; and D: vacancies diffusing to a $200b$-radius loop. All the cases are plotted for nickel at 450°C (723 K), $\Delta V/\Omega = -0.2$ for vacancies, and $\Delta V/\Omega = 1.8$ for interstitials, where ΔV is the volume change per defect and Ω is the atomic volume.

Figure 4.7 shows the loop radius dependence of the effective capture radius. The strength of the loop as a sink for defects per unit length of dislocation decreases with increasing loop size. The sink efficiency and capture radius for both defects are very high for small loops but decrease with increasing loop radius until they are comparable with the results for straight edge dislocations when the loop diameter is comparable with the outer cutoff radius used in the edge dislocations calculations. Small loops are a much stronger sink for defects than an equivalent length of edge dislocation.

In summary, we have overcome the core radius difficulty encountered in previous calculations, and have found the flux of defects to faulted dislocation loops to be much larger than that for straight edge dislocation for defects diffusing in a pure material. In addition, we have found that including the modulus interaction does not make an appreciable difference in the defect flux but does change the local defect concentration profile near the dislocation loop.

ORNL–DWG 77-20019

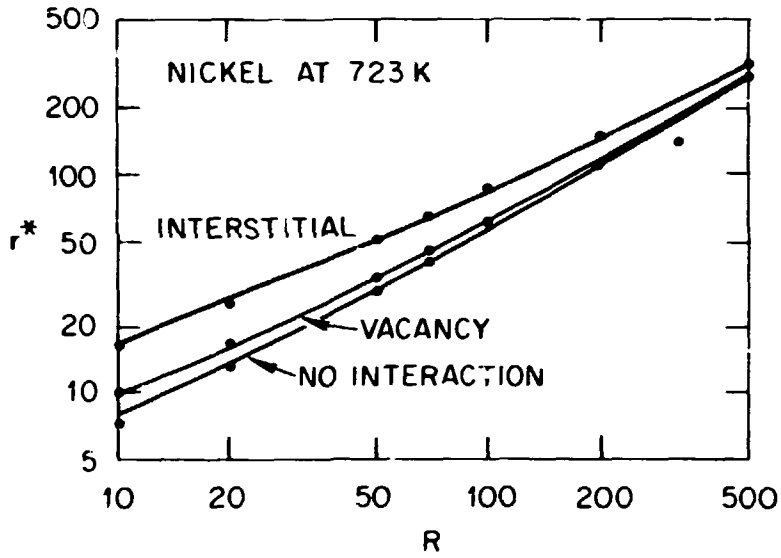

Fig. 4.7. The Dependence of the Effective Capture Radius, r^*, on the Dislocation Loop Radius for Diffusion of Interstitials and Vacancies to an Interstitial Dislocation Loop. The material parameters are the same as for Fig. 4.6.

4.1.6 Modeling the Growth Kinetics of Frank Loops under HVEM Irradiation Using Calculated Defect Preference Factors — W. A. Coghlan and M. H. Yoo

Recently, an HVEM irradiation experiment was performed at ORNL on pure nickel to determine the defect bias of a growing array of faulted dislocation loops.[18] A calculation of the required defect preference factors was completed.[19] We would like now to include the calculated defect preference factors in the general rate theory model that was used to analyze the HVEM experimental results, and then to see if the model could still be applied to the experimental results.

---

[18]M. H. Yoo and J. O. Stiegler, "Growth Kinetics and 'Preference Factor' of Frank Loops in Nickel During Electron Irradiation," *Philos. Mag.* 36: 1305–15 (1977).

[19]W. A. Coghlan and M. H. Yoo, "Modeling and Growth of a Finite Interstitial Loop Under Irradiation," *Trans. Am. Nucl. Soc.* 27: 330–32 (1977).

Two changes were made in the rate theory model. First the equations were modified to include a depth-dependent dislocation loop density. Analysis of the experimental data suggested a linear variation loop density with foil depth.

The second change was to replace the previous description for the effective capture radius of the loops. An empirical expression was derived by a least squares fit, in log space, to 70 values of capture radius from a previous calculation.[16,19] This expression for the effective capture radius r^* in units of the Frank loop Burgers vector b is given in Eq. (5):

$$r^* = a_0 R^{P(R,\xi)} \quad \text{for } 10 \leq R \leq 500 \text{ and } 0 \leq \xi \leq 700 \tag{5}$$

where

$$P = a_1 + a_2/R^{5/4} + a_3(\xi/R)^{3/4} + a_4(\xi/R)^{3/2} ,$$

R = loop radius in units of b,

$\xi = \Delta V \mu/kT$,

ΔV = relaxation volume for the diffusing defect,

μ = shear modulus of the material,

k = the Boltzmann constant,

T = absolute temperature.

The constants a_0 through a_4 are 0.5837, 0.9852, 2.779, 5.492×10^{-2}, and -2.300×10^{-3}, respectively. This equation agrees with the calculated values of r^* to ±3% on the average, with the maximum difference 11%, which was found for the smallest loop ($R = 10b$) with no interaction.

The previous analysis of the HVEM results assumed that the sink preference factors were the least well-known of the input parameters. For this new calculation the relaxation volumes of the defects and the generation rate of defects were assumed to be poorly known, and these parameters were adjusted to fit the experimental results. Figure 4.8

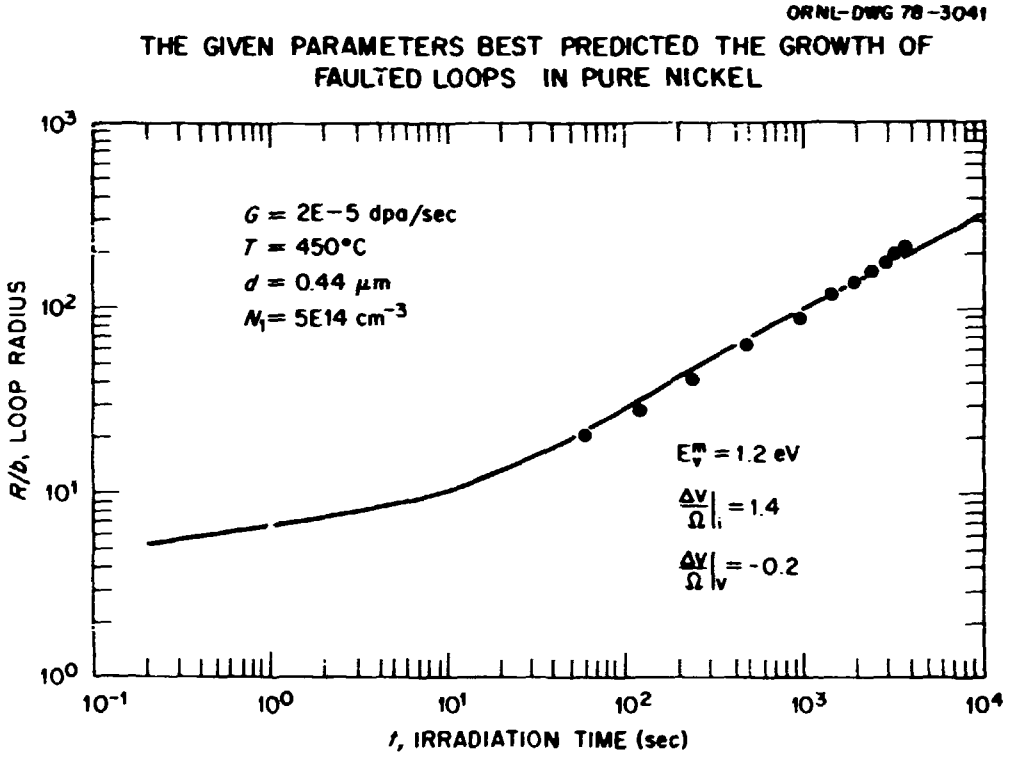

Fig. 4.8. The average loop radius vs irradiation time for HVEM irradiation of pure nickel. Each point is the average of 35 loops and the solid line is the prediction of the model.

shows the average loop radius as a function of time, and Fig. 4.9 gives the depth dependence of the loop size as a function of irradiation time. The dashed curves in Fig. 4.9 are the predictions of the previous model.

The results show that calculated preference factors can be used to fit experimental dislocation loop growth results even though they show a strong loop size dependence and also are much larger than values used previously. The fit does require a defect production rate of 2×10^{-5} dpa/s, which is about one-third the value used previously.

Two final observations were made. First, a value of 1.2 eV for the migration energy of a vacancy in nickel was required to obtain the good fit shown in Fig. 4.8. Second, the calculated preference factors halve the average defect concentration, and this reduction will be important for the calculation of nucleation rates of voids and loops in the presence of a population of loops.

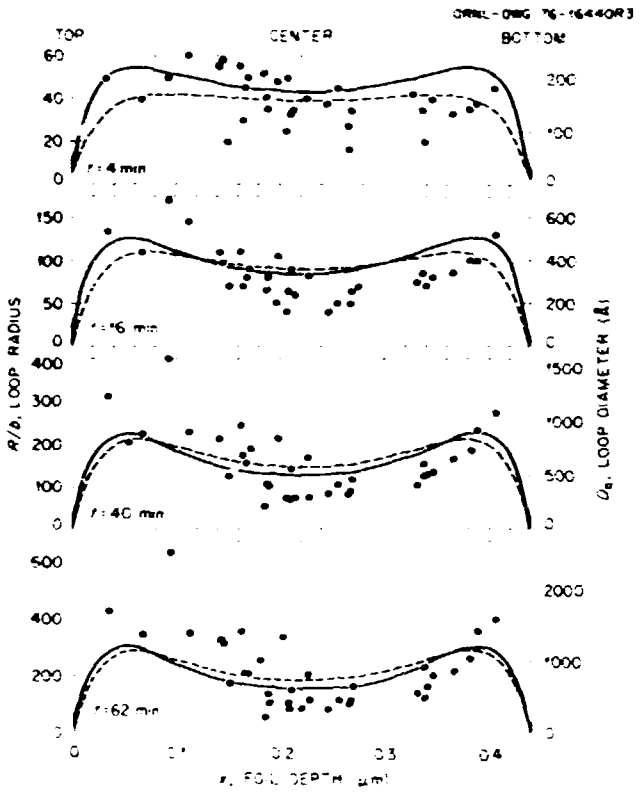

Fig. 4.9. Loop size vs Position in the Foil for Four Irradiation Times. The solid curves are the prediction of the current model while the dashed curves are the previous predictions. The depth positions were measured by stereomicroscopy, and the calculated curves were obtained with E_v^m = 1.2 eV, δ_i = 0.06.

4.2 EXPERIMENTAL STUDIES

4.2.1 Comparison of the Effects of Simultaneously Injected and Preinjected Helium on the Microstructure of Ion-Bombarded Nickel — N. H. Packan and K. Farrell

As part of a continuing effort to correlate microstructural damage produced by heavy-ion bombardment with that produced by neutrons in pure nickel at a damage level of 1 dpa, experiments have been carried out to see if there is a difference between introducing helium at room temperature before ion bombardment and injecting it during bombardment. In both cases the quantity of helium (20 at. ppm) was equivalent to that generated in the neutron-irradiated specimens studied earlier.[11] Bombardments were carried out to a dose of 1 dpa at 50°C intervals from 500 through 700°C.

The presence of helium, either preinjected or simultaneously injected, does not affect the level of heavy-ion-induced swelling at or near the peak swelling temperature of 600°C, but it does cause appreciable increases in swelling at the high- and low-temperature ends of the swelling range. The void populations in *simultaneously* bombarded specimens fairly closely resembled those in the helium-free cases; by contrast, the *preinjected* helium specimens had significantly greater (up to a factor of 10) concentrations of distinctly smaller voids. Dislocation densities were a little higher with preinjected helium.

These results indicate that in the pure nickel studies, preinjection of helium promotes void nucleation whereas simultaneously injected helium does not. This result is thought to be a consequence of the relative ease of void formation in this material, in the first case, and competition for absorption of gases and vacancies at existing sinks in the second case. In this nickel there appears to be an abundance of residual gases such as O, H, and N, which facilitate void nucleation in the early stages of bombardment; preinjection of helium aids this nucleation. If helium is trickled in during irradiation, the preexisting residual gases dominate void nucleation and the voids then either absorb the helium as fast as it is implanted or they absorb vacancies and maintain the vacancy supersaturation at a level too low to encourage further void nucleation.

There is evidence that simultaneously implanted helium has a much stronger role in materials that are inherently more resistant to void nucleation, such as some stainless steels, and this is now under investigation.

4.2.2 Effect of Gas Level and Method of Gas Implantation on Irradiation Damage Simulation in an Austenitic Alloy — K. Farrell and N. H. Packan

Simulation of neutron damage microstructures using energetic beams of electrons or ions to displace atoms is now widely used for control and isolation of individual parameters involved in evolution of damage structure, and to achieve high displacement levels in short times. A unique application of these simulation techniques is in the production

of damage structures relevant to fusion reactor conditions that cannot be met in fast-fission reactors. A major feature of these conditions is the high production rates of transmutation-created helium and hydrogen, which are expected to significantly modify the damage microstructures. We are examining the effects of high gas level and the method of implanting the gas on the development of damage structure, particularly cavity swelling, during nickel ion bombardment in our dual-accelerator irradiation facility.

The target material is a high-purity Fe–17% Cr–14% Ni–3% Mo austenitic alloy, which approximates a stainless steel and swells readily. It is free of the complications of phase changes that occur during irradiation of commercial stainless steels. Bombardment temperatures are 575, 625, 680, 750, and 825°C, with peak swelling occurring in the virgin material at 625 to 680°C. Damage levels are 1, 10, and 70 dpa, the last causing 18% swelling in the virgin alloy at 625°C. Gas implantation conditions, mostly helium, are:

1. simultaneous injection of helium at a rate of 0.2 at. ppm He/dpa to reproduce a condition similar to those in fast fission reactors;
2. simultaneous injection of helium at a rate of 20 at. ppm He/dpa, a helium generation rate similar to that expected in the first wall of a fusion reactor;
3. simultaneous injection of both helium and hydrogen at rates of 20 at. ppm He/dpa and 50 at. ppm H/dpa to examine interactive effects of hydrogen under fusion reactor irradiation conditions (see Sect. 4.2.4);
4. preinjection at room temperature with 14 at. ppm He (corresponding to 70 dpa at a simultaneous rate of 0.2 at. ppm He/dpa) and with 1400 at. ppm He (for comparison with 70 dpa at a simultaneous rate of 20 at. ppm He/dpa); and
5. preinjection at the bombardment temperatures with 14 at. ppm He and with 1400 at. ppm He.

More than half of the irradiations have been completed, and work has begun on transmission electron microscopic examination of the damage microstructures. Results to date indicate some trends.

Preinjected helium has significantly different effects on void nucleation and swelling than does simultaneously injected helium. High levels of preinjected helium considerably depress swelling at the lower temperatures by markedly decreasing the size and increasing the concentration of cavities; simultaneously implanted helium has relatively little effect in this material. At the higher temperatures the helium increases swelling by encouraging growth of cavities. The net effect of high helium level is to push the swelling curve to higher temperatures. When both helium and hydrogen are implanted, the helium dominates the microstructural changes.

4.2.3 The Influence of Helium on the Evolution of Damage Microstructure in Type 316 Stainless Steel Alloys under Ion Irradiation — E. A. Kenik

As reported last year, the swelling resistance of a silicon- and titanium-modified type 316 stainless steel (LS!A) was accompanied by segregation of silicon to irradiation-produced faulted loops and subsequent precipitation that reflects the phase instability of the alloy. In contrast to this, a nominal type 316 stainless steel alloy (G7) exhibited high swelling rates but showed little or no solute segregation or phase instability. The evolution of the damage microstructure and its dependence on the presence or absence of helium and the mode of its introduction have been under investigation during the past year.

Without helium, LS!A exhibits no void formation at doses up to 600 dpa, even though the alloy undergoes extensive phase instability. On the other hand, G7 swells rapidly, even in the absence of helium, exhibiting about 170% swelling at 600 dpa. Preinjection with helium results in a significant reduction in dislocation loop sizes and an increase in loop concentration in both LS!A and G7. This behavior appears to have only slight consequence on the damage microstructure in G7 at higher doses. As in the absence of helium, the loops evolve into a dislocation network, and void swelling occurs at a slightly enhanced rate. The enhancement of loop formation in LS!A resulting from helium preinjection has a profound effect on the subsequent solute segregation, phase instability, and void formation. A very fine-scale, high-density

platelet precipitate forms on (111) planes, reinforcing the thesis that solute segregation at loops results in phase instability at these loops. Again no void formation is observed. The injected helium may be trapped in a fine dispersion at the high density of precipitate particles. Simultaneous helium injection during the ion irradiation results in different damage evolution that depends on the relative rates of helium injection and displacement damage (helium/dpa). At ratios typical of fast-fission reactors (0.2 at. ppm He/dpa), the early evolution of damage for both G7 and LS1A was similar to the "no helium" cases. Swelling in G7 was enhanced, while in LS1A void formation was finally observed, the voids being associated with the irradiation-produced precipitate.

Segregation of silicon to the loops is evidence that in LS1A interstitial or vacancy trapping at silicon solute atoms occurs; the removal of traps can affect both nucleation and growth of voids (see Sect. 4.1.2). While phase instability in LS1A appears to be associated with void formation, it is definitely not sufficient, as is shown by the absence of swelling both uninjected and preinjected specimens, where precipitation also occurs during irradiation. The suggestion that both gross phase instability and injected helium are required to produce swelling in this alloy indicates that at least two swelling suppression mechanisms are operative, solute trapping of irradiation-produced defects and gettering of gaseous impurities by titanium and possibly silicon.

The mode of helium introduction has some effect on the damage evolution in a high-swelling, stable alloy such as G7. However, in a low-swelling, unstable alloy such as LS1A, the effects are more dramatic. Since the loop structure determines the precipitate structure, which in turn may determine the final distribution of helium, large differences occur between preinjection and simultaneous injection of helium. A critical feature of this process is the presence of sufficient helium at low doses to affect the loop evolution, which will occur both for the preinjection and high He/dpa simultaneous irradiation conditions.

4.2.4 A Technique for Simultaneously Bombarding Solids with Helium, Hydrogen, and Heavy Ions to Simulate Microstructural Damage from Fission or Fusion Neutrons — K. Farrell, M. B. Lewis, and N. H. Packan

Damage simulation techniques in which solids are bombarded with beams of heavy ions to create atomic displacements, which in turn evolve into microstructural defects, are now an accepted practice. They fall short, however, in duplicating the transmutation products hydrogen and helium, which play important roles in damage evolution. To overcome this deficiency partially, a second accelerator can be used to implant one of the gases simultaneously with the heavy ion bombardment. We have now developed a technique for simultaneously implanting from one accelerator both hydrogen and helium in any desired ratio into the displacement damage region created by heavy ions from another accelerator.

This significant improvement is achieved by including both helium and molecular deuterium in the gas accelerator ion source. These two gases have the same mass (4), and in the same charge state they are accelerated to the same energy (E) and are propelled together through the selector magnet. The deuterons in the ionized molecule are so loosely bound that they separate immediately and completely at the target face, each deuteron taking, on the average, half of the incident energy ($E/2$). The stopping power (S) of a deuteron in the target is about half that of a helium atom. Since the depth of penetration varies as E/S, the deuterons will come to rest at approximately the same depth as the helium.

By selecting an appropriate accelerating voltage the implanted helium and hydrogen can be superimposed on the displacement damage region created by a beam of heavy ions from another accelerator, in our case a 5-MV Van de Graaff. For a 4-MeV ^{58}Ni beam the peak displacement damage occurs at about 0.7 to 0.75 μm below the target surface. We overlay this region with the implanted gases by sinusoidally ramping the voltage of the gas accelerator between 0.2 and 0.4 MV to give a fairly level concentration of gas at depths between 0.5 and 0.8 μm.

The damaged region now contains all the important elements that contribute to development of the microstructure. The relative amounts of these elements can be tailored to reproduce a wide range of neutron irradiation conditions, including those for breeder reactors and for magnetic fusion reactors. Tailoring consists of adjusting the gas/dpa ratio and the He/H ratio. The former is done by appropriately balancing the ratio of the beam currents in the two accelerators. The ratio of He/H in the target is decided by the helium/molecular deuterium mix in the ion source, but since the helium and molecular deuterium have different ionization potentials the ratio in the source is not a simple function of the ratio required at the target. The correct source mix is determined empirically by backscattering analysis. Once this calibration is established, any derived ratio of He/H can be selected by manipulation of gas flow at the source.

To date we have done two irradiations with this new triple ion facility using a pure stainless steel target and the temperatures 625 and 750°C, dpa = 70, He/dpa = 20, and H/dpa = 50, to simulate future fusion reactor irradiation. Analysis of the microstructures is incomplete, but a tentative conclusion is that helium has the dominant role in altering the swelling behavior.

4.2.5 Effect of Tensile Stress on the Growth of Helium Bubbles in a Model Stainless Steel[20] — D. N. Braski, H. Schroeder,[21] and H. Ullmaier[21]

Helium embrittlement poses one of the more serious problems for structural alloys for both fission and fusion reactors. The goal of this experiment was to provide data that would help understand the basic mechanism of helium embrittlement. We determined the effect of time and stress on the growth of helium bubbles in a simple model stainless steel — Fe—20 wt % Cr—18 wt % Ni. The effect of helium bubbles on the creep properties of the alloy was also studied.

---

[20]Summary of research conducted by D. N. Braski while on assignment to KFA, Jülich, West Germany.

[21]KFA, Jülich, West Germany.

The alloy is a stable, single-phase fcc alloy with no carbide precipitates. Fine-grained foils (120 μm thick) were fabricated into tensile specimens and then were injected with about 158 at. ppm He with a cyclotron. The specimens were creep tested in high-vacuum (<10 μPa, 10^{-7} torr) creep machines under constant stress at 750°C (1023 K). Transmission electron microscopy (TEM) showed that helium bubbles grew in the absence of applied stress at different rates depending on their location in the microstructure. Bubbles in the matrix grew quite slowly compared with those located on grain boundaries or grain boundary intersections (triple point junctions). An applied tensile stress enhanced helium bubble growth, especially at the grain boundaries and junctions, as shown in Fig. 4.10. Figure 4.11 shows the results of bubble measurements made on different specimens that had been annealed at 750°C for various times and stress levels. The mean radius, $\bar{r}$, is related to time, t, by the exponent n, as follows: $\bar{r} \propto t^{n}$.

The values of n for unstressed samples of about 0.2 compared favorably with those reported for niobium at similar homologous temperatures.[22,23] The values of n for stressed samples ranged from 0.06 to 0.83 and could not be related directly to any single existing growth model for bubbles under stress. The number of helium bubbles in the grain boundaries decreased rapidly with time and then leveled off. This result indicated that a mechanism of bubble migration and coalescence was operative, perhaps assisted by grain boundary sliding. No small helium bubbles were observed after the shortest annealing time (8 h), and, therefore, bubble nucleation was probably active only during the early stages of annealing or creep. This latter observation coupled with estimates of the amount of helium in the bubbles also suggested that most of the helium precipitated in bubbles early during

---

[22]D. Aitken, P. J. Goodhew, and M. B. Waldron, "Helium Bubble Formation and Migration in Niobium," [illegible] (Proc. Conf.) 244: 15–16 (1973).

[23]L. A. Charlot, J. L. Brimhall, and D. G. Atteridge, "Transmission Electron Microscopy on Helium Implanted Niobium Tensile-Specimens," J. Nucl. Mater. 66: 203–08 (1977).

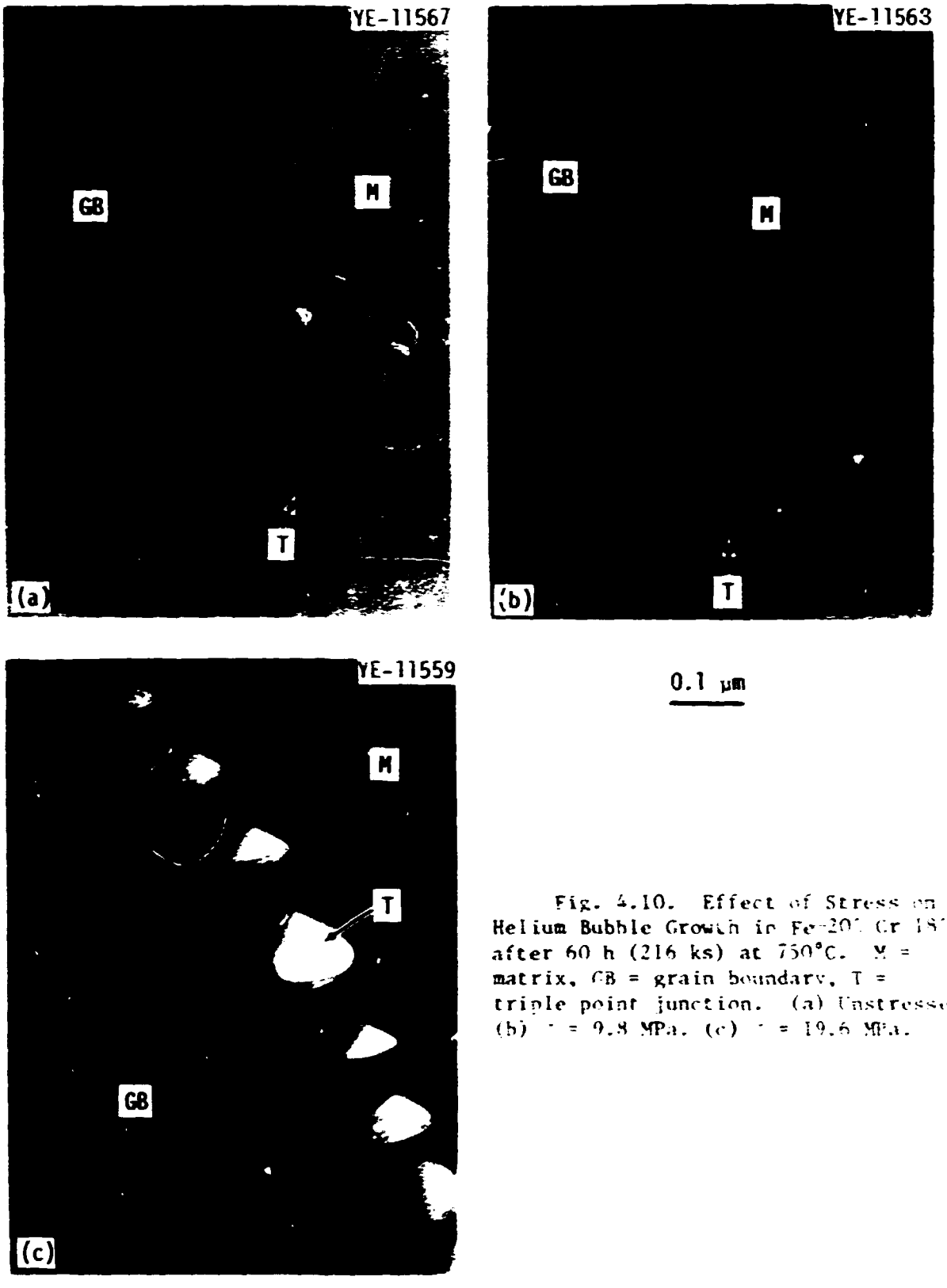

Fig. 4.10. Effect of Stress on Helium Bubble Growth in Fe-20% Cr 18% Ni after 60 h (216 ks) at 750°C. M = matrix, GB = grain boundary, T = triple point junction. (a) Unstressed. (b) [illegible] = 9.8 MPa. (c) [illegible] = 19.6 MPa.

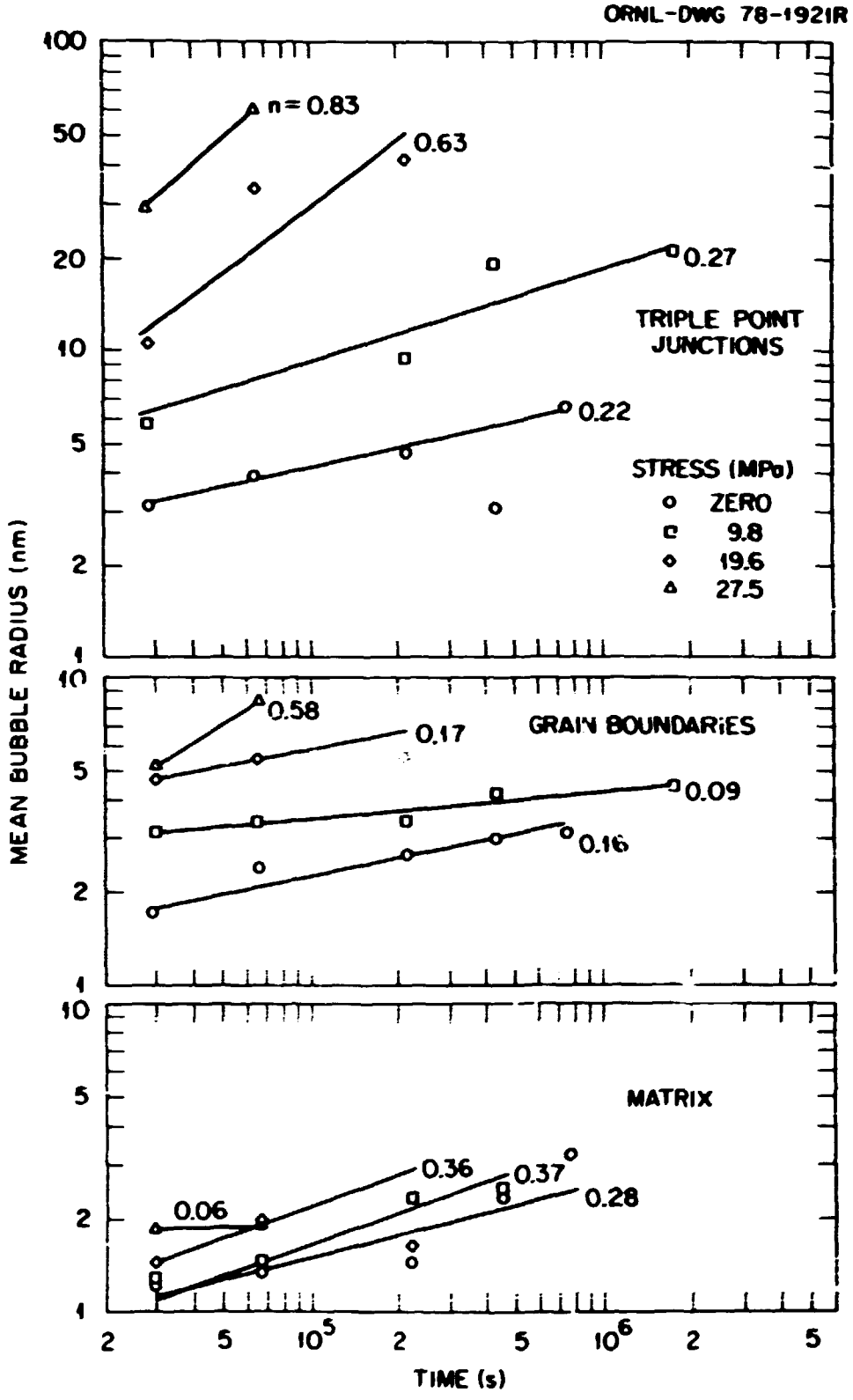

Fig. 4.11. Helium Bubble Growth in Fe–20% Cr–18% Ni at Different Stress Levels as a Function of Time at 750°C.

the anneal. Growth was then believed to occur mainly by migration and coalescence and, later, as the bubbles were quite large, by the stress-assisted diffusion of vacancies to the bubbles. With the grain boundaries serving as both sources and conductors of vacancies, one would expect the bubbles at this location to grow more rapidly, as was observed.

The presence of helium in Fe–20% Cr–18% Ni specimens increased their creep rates and caused premature failures. Scanning electron microscopy showed that the fracture mode for ruptured specimens containing helium was entirely intergranular, while that for unimplanted specimens was a mixture of intergranular fracture and ductile tearing. Grain boundary sliding was the dominant mechanism for creep in unimplanted specimens, and when helium was present, this process was accentuated. Consequently, helium-"embrittled" specimens of the soft, ductile, model alloy often demonstrated only slightly reduced ductility despite the shorter rupture times. Cracks appeared to be initiated at triple point junctions in creep specimens containing helium.

4.2.6 Radiation Effects in Ordered Alloys — E. A. Kenik and R. W. Carpenter

Van de Graaff nickel ion (4 MeV) irradiation experiments for nickel-molybdenum alloys have been extended during the past year to higher doses and to include the effects of simultaneous helium injection to enhance conditions for void nucleation. As reported[24] last year, lower molybdenum alloys such as Ni–7 at. % Mo alloys are much more resistant to void swelling than elemental nickel under simple nickel ion irradiation. The "nucleation" dose for voids was about 100 dpa, and a large amount of swelling occurred at 200 dpa. Alloys of Ni–20 at. % Mo, in which short-range order is stable during irradiation, did not exhibit any void nucleation under the same conditions

---

[24]R. W. Carpenter, E. A. Kenik, and M. H. Yoo, "Effects of Chemical Ordering and Coherent Precipitation on Void Nucleation During Irradiation," *Metals and Ceramics Div. Mater. Sci. Annu. Prog. Rep. June 30, 1977*, ORNL-5311, pp. 69–70

of nickel-ion irradiation up to a dose of 100 dpa. Both alloys were of high purity to avoid any chemical impurity effects on the irradiation experimental results. The high purity of the alloys caused concern that the apparent swelling resistance was a result of the absence of gas in the alloy lattice, thought necessary for void nucleation. The irradiation tests were repeated under the same experimental conditions plus simultaneous helium injection at the rate of 0.2 at. ppm He/dpa. The Ni–7 at. % Mo irradiation response was as observed earlier; no detectable step height was observed after an irradiation to 100 dpa at 675°C (948 K) (20 at. ppm He total). After a 200-dpa dose at 675°C (40 at. ppm He total) the average step height for three specimens was 166 nm ($\sim$7% $\Delta V/V$), a large swelling, as observed earlier for nickel-ion irradiation without helium. These results show that at least in this alloy void nucleation was not strongly affected by the presence of helium. When Ni–20 at. % Mo alloys were irradiated at 675°C to doses of 100 and 200 dpa with simultaneous helium injection of 0.2 at. ppm/dpa (20 and 40 at. ppm total He, respectively) no measurable step height was observed for either dose. This result shows conclusively that this alloy, for which short-range order is stable under the irradiation, is very resistant to swelling under favorable conditions for void nucleation.

4.2.7 The Effect of Semicoherent Precipitation on Void Swelling in Al-Cu Alloys[25] – R. W. Carpenter and M. H. Yoo

Alloys of Al–4 wt % Cu previously heat-treated (50 h at 200°C) to contain semicoherent θ' precipitate were neutron-irradiated to a fast fluence of 2.8×10^{20} n/m^2 (>0.1 MeV) at 55°C to determine the effect of the precipitate on void swelling relative to that in pure aluminum. The void swelling values were about 1% and about 12% for the alloy and elemental aluminum, respectively. The broad faces of the θ' precipitate underwent at least partial coherency loss, the matrix dislocation density increased, and some of the transmutation-formed

[25]Summary of a paper accepted for publication in *Metallurgical Transactions A*.

silicon segregated to θ′ interfaces and some to voids during the irradiation. The θ′ particle size distribution did not change significantly during the irradiation. The swelling behavior of the alloy under irradiation was analyzed by extending the rate theory of swelling to include reduction of irradiation-caused point defect concentration by indirect recombination, a result of trapping free point defects at θ′ interfaces. Calculated swelling in the alloy using the model agreed well with the experimental observation. According to the model, the suppression of swelling by θ′ precipitate under these irradiation conditions occurs by extension of the "knee" of the swelling curve, not by changing the dose exponent for swelling.

This result is shown clearly on the calculated values of swelling versus irradiation time (i.e., neutron dose) in Fig. 4.12. Three curves are shown. The solid curve for elemental aluminum represents the control specimen and the calculated swelling of 10% agrees well with the experimental result. The curves for the alloy containing θ′ show that both semicoherent and incoherent θ′ precipitate will suppress swelling, with the semicoherent precipitate having the stronger effect. The calculated suppression of swelling is in good agreement with the observed swelling result of ∿1%. These calculated curves represent the swelling behavior of the alloy if the precipitate is either semicoherent or incoherent throughout the entire radiation cycle. Our observations showed that the precipitate is semicoherent at the beginning of the irradiation but becomes incoherent during the irradiation; thus the theoretical treatment can be improved by imposing an irradiation time dependence (equivalently, a dose dependence) on the state of coherency of the precipitate.

4.2.8 Neutron Irradiation Damage in Molybdenum at High Temperatures[26] — J. Bentley and F. W. Wiffen

Commercially pure molybdenum (∿30 wt. ppm C) was irradiated in EBR-II to a fluence of about 6×10^{25} n/m^2 (>0.1 MeV), which

[26]Summary of paper presented at 107th Annual Meeting AIME, February 26–March 2, 1978, Denver, Colo.

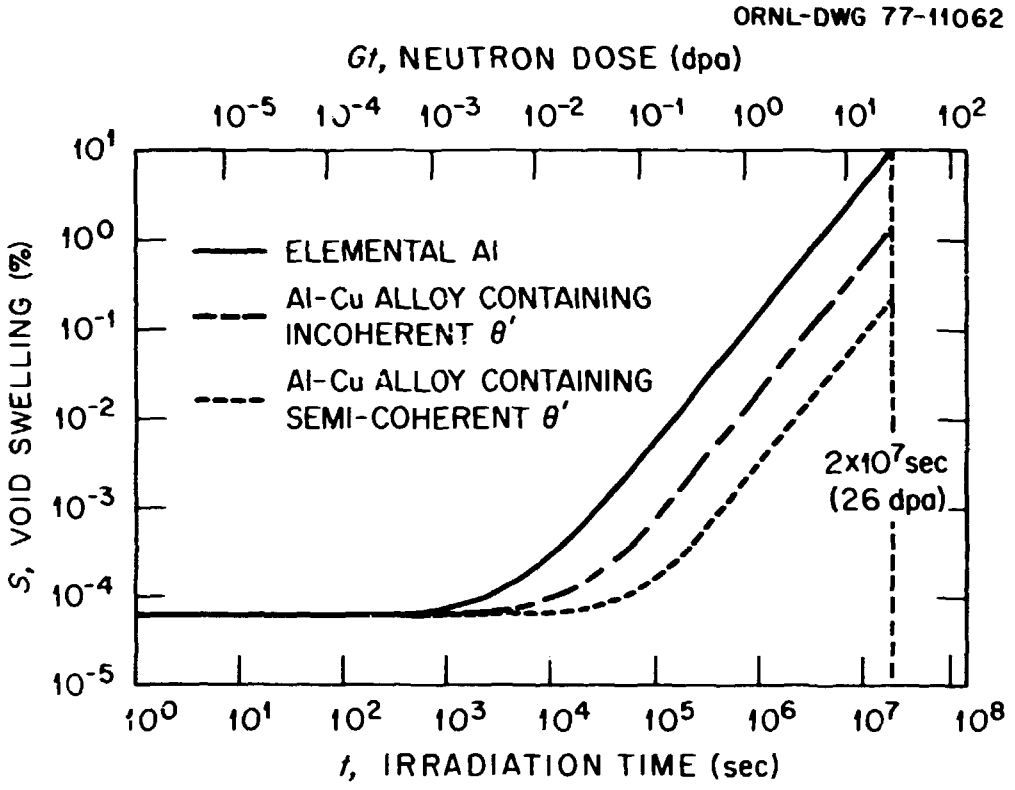

Fig. 4.12. The Dose Dependence of Void Swelling for aluminum and Al–3.8 wt % Cu Alloys Containing Different Forms of θ′ Precipitate.

corresponds to about 2 dpa. Irradiations were at nominal temperatures of 600, 900, 1100, 1300, and 1500°C (~0.31 to $0.62T_m$). Specimens were cut from the irradiated rods and thinned for transmission electron microscopy and small-angle x-ray scattering.

The irradiated microstructure contains two components — voids and dislocations. Dislocation densities were generally low, decreasing from about $2 \times 10^{14}/m^2$ at 600°C to about $5 \times 10^{11}/m^2$ at 1500°C. The dislocations were in the form of a network at all temperatures except at 600°C, where some small loops are also present.

Voids were observed at all temperatures. The void concentration decreased monotonically from about $2 \times 10^{23}/m^3$ at 600°C to below $10^{17}/m^3$ at 1500°C, and the mean void diameter increased from about 4 nm at 600°C to about 200 nm at 1500°C. The resultant values of swelling are less than 0.7% and show a general decrease with increasing irradiation temperature. At temperatures of 600 and 900°C small-angle

electron diffraction indicated imperfect void ordering on a bcc superlattice, and for temperatures up to 1100°C the equiaxed, faceted voids were distributed homogeneously. At irradiation temperatures of 1300 and 1500°C the voids were inhomogeneously distributed, and some elongated or "super" voids were observed. The crystallography of the elongated voids was complex, with examples of the "long axis" of the voids observed to be parallel to both high- and low-index directions. Also at 1300 and 1500°C precipitates of various morphologies and sizes were observed to be associated with the voids. Energy-dispersive x-ray analysis failed to reveal any detectable impurities with $Z \geq 11$ in the precipitates; further attempts at identification by electron diffraction will be made.

The observation of elongated voids is consistent with previous observations, but the mechanism of formation is still not understood. As in quenched materials, elongated voids often form in association with precipitates under conditions of low vacancy supersaturation (slow quench, high aging temperature or high irradiation temperatures, low neutron flux).

The results will be used in correlations with positron annihilation and small-angle x-ray scattering studies.

4.2.9 Faulted Loops in Neutron-Irradiated Zirconium[27] —

A. Jostsons,[28] R. G. Blake,[28] J. G. Napier,[28] P. M. Kelly,[28] and K. Farrell

The radiation damage microstructure in α-zirconium consists primarily of dislocation loops. It is necessary to characterize the nature of these loops in order to determine how the damage structure evolves. Usually the loops are perfect $(1/3)\langle 11\bar{2}0\rangle$ type. We have recently discovered some unusual, large faulted loops in high-purity zirconium irradiated at 723 K to 1.3×10^{25} neutrons/m^2 (>0.1 MeV). The transmission electron microscopy characterization of these $(1/6)\langle 20\bar{2}3\rangle$ faulted loops on (0001) is described in detail. The faulted

---

[27]Summary of *J. Nucl. Mater.* 68(3): 267–76 (1977).

[28]Materials Division, AAEC Research Establishment, Lucas Heights, N.S.W., Australia.

loops were invariably vacancy in character although the coexisting population of perfect (1/3) $\langle 11\bar{2}0 \rangle$ loops was of a mixed interstitial-vacancy nature. The faulted loops were observed in specimens of only two out of five batches of high-purity zirconium irradiated in this experiment. Even in these two specimens, the presence of faulted loops was restricted to the 723 K irradiation temperature; at 673 K only perfect (1/3) $\langle 11\bar{2}0 \rangle$ loops were seen.

4.2.10 Damage Structures in Zirconium Alloys Irradiated at 300 and 650°C (573 and 923 K) — R. W. Gilbert[29] and K. Farrell

Zirconium and its alloys are unusual because they seem to be immune to radiation-induced void formation. The cause of this immunity is not known. The temperature dependence of damage structures in zirconium has not been extensively characterized. Since there is a great technological need for the development of swelling-resistant alloys, there is clearly reason for further investigation of the radiation damage structure of zirconium and for pursuit of the source of its void resistance. Accordingly, the microstructures of annealed zirconium, Zircaloy-2, and Zr–2.5 wt % Nb alloy and Zr–2.5% Nb containing α' were studied after fast-neutron irradiations to fluences of about 1×10^{25} n/m^2 in the temperature range 300–650°C, where voids might be expected. None were found. The principal form of damage was dislocation loops, which increased in size and decreased in density with increasing temperature and did not exist above 500°C. The Burgers vector of the loops was consistent with $(a/3)\langle 11\bar{2}0 \rangle$. Half or more of the loops were of the vacancy type. There was no dislocation network. An irradiation-induced precipitate of β-niobium formed in the α' phase in quenched-and-aged Zr–2.5% Nb. This demonstrates that in α-zirconium the loop structures saturate with fluence and do not develop into dislocation structure. These microstructural changes are different from those in fcc and bcc metals that swell readily. It is argued that the bias of loops for self-interstitial atoms in

---

[29]Atomic Energy of Canada, Ltd., Chalk River Nuclear Laboratories, Ontario, Canada.

α-zirconium is very weak, permitting competitive development of vacancy and interstitial loops, preventing growth of the loops into a dislocation structure, and depressing the vacancy supersaturation so that voids cannot nucleate.

4.2.11 Microstructure and Tensile Properties of Heavily Irradiated 1100-0 Aluminum[30] — K. Farrell and A. E. Richt[31]

Aluminum 1100-0 is a soft and ductile grade of commercially pure aluminum that is used in some water-cooled nuclear reactors for applications where high strength is not required. Its mechanical properties have never been investigated after very high neutron doses. This work examines the microstructural changes and the resulting alteration of tensile properties that are caused by neutron irradiations up to 1.4×10^{27} n/m^2 (>0.1 MeV) and 2.3×10^{27} n/m^2 (<0.025 eV) at about 55°C (328 K, 0.35 T_m), corresponding to displacement levels of 200 dpa and the generation of 5.5 wt % Si. The material displayed up to about 8% swelling. Microstructural features included dislocation tangles, a precipitate of elemental silicon, and heterogeneously distributed voids coated with silicon. Alongside grain boundaries were sheets of large voids. These microstructural features are shown to be responsible for increasing the 0.2% flow stress and the ultimate tensile stress at 50°C by factors of 5 and 3 to values of 220 and 250 MPa, respectively, and by factors of 6.5 and 3.5 to about 190 MPa at 150°C (423 K, 0.45T_m). Elongation was reduced at 50°C from 32% to a plateau at 12% in the fluence range 4×10^{25} n/m^2 to 7×10^{26} n/m^2 (>0.1 MeV), followed by a sharp fall to 4% at the highest fluences, the latter concomitant with a change to intergranular fracture. In the 150°C tests the elongation declined from 56% to 4% at the highest fluences, where intergranular fracture prevailed. Most of this loss in

---

[30]Summary of a paper to be presented at ASTM 9th International Symposium on *Effects of Radiation on Structural Materials*, July 11–13, 1978, Richland, Wash., and to be published in the proceedings.

[31]Now with Union Carbide Corporation, South Charleston, W.V.

ductility is accountable in terms of dispersion hardening through changes in strain hardening parameters. We suggest that the apparent intergranular fractures are caused by tearing of sheets of voids adjacent to grain boundaries.

4.2.12 Tensile Properties of Neutron-Irradiated 6061 Aluminum Alloy in Annealed and Precipitation-Hardened Conditions[32] — K. Farrell and R. T. King

The aluminum alloy 6061 has a nominal composition of 1 wt % Mg and 0.6 wt % Si and can be hardened by precipitation of Mg_2Si. In the precipitation-hardened, or "T6" condition, the alloy is used for high-strength applications in some water-cooled reactors. In an annealed, or "0" condition, it is much weaker and is more ductile, but its mechanical response to very high neutron doses has never been measured. This work investigates and compares the tensile properties of 6061-0 with those of 6061-T6 at several test temperatures after irradiation in water at 55°C (328 K, $0.35T_m$) to fast (>0.1 MeV) fluences up to 1.8×10^{27} n/m^2 and thermal (<0.025 eV) fluences up to 3.0×10^{27} n/m^2. The corresponding maximum displacement level was 260 dpa, and over 7 wt % Si was created from transmutation reactions. The major microstructural defects were voids, dislocations, and a precipitate of silicon. Swelling from voids was less than 1%. In the "T6" material tested at 50°C (323 K, $0.35T_m$) and 100°C (373 K, $0.4\,T_m$) irradiation raised the 0.2% flow stress and the ultimate tensile strength by 45 to 60% from the unirradiated values of about 280 and 330 MPa, respectively; ductility was reduced from 15 to about 9%. At 150°C (423 K, $0.45T_m$) there was a similar degree of hardening, but ductility fell to about 5%. The alloy in the "0" condition remained softer, by 125 to 150 MPa, than the irradiated "T6" alloy, and its elongation remained above 10%. In all cases the loss in ductility occurred principally through reduction in uniform strain. Fractures were ductile.

---

[32]Paper to be presented at ASTM 9th International Symposium on *Effects of Radiation on Structural Materials*, July 11–13, 1978, Richland, Wash., and to be published in Proceedings.

4.2.13 Simulation of Irradiation Creep Using Light Ions — T. C. Reiley, R. L. Auble,[33] and R. H. Shannon

Irradiation creep is the phenomenon whereby radiation, which causes atomic displacement events, can increase the rate of deformation of load-bearing materials. This behavior is important under neutron irradiation and is observed in structural materials (stainless steels, niobium-base alloys, zirconium alloys, graphite), as well as nuclear fuels (UO_2, UC, U). The common technique for studying irradiation creep has been the use of loaded springs or pressurized tubes placed in reactor and removed at various intervals for dimensional inspection. A different approach has been taken at ORNL, among other laboratories, in which a beam of energetic light ions (60-MeV He^{2+}) from a cyclotron is focused on a specimen under load. The particle beam may be controlled to provide an atomic displacement environment that simulates a reactor environment. The experimental control is superior to that obtained in reactor and continuous experimental information may be obtained.

During this year, after several preliminary experiments, a successful irradiation creep experiment was performed. The results from this experiment are given in Fig. 4.13, in which the observed creep rate is plotted versus irradiation time for 20%-cold-worked type 316 stainless steel at an average temperature of 462°C (735 K), a stress of 140 MPa, and a calculated displacement rate of 1.3×10^{-6} dpa/s. The rapid transient in creep rate is consistent with other observations for light-ion- and neutron-irradiated stainless steels. Microstructural investigations are under way to identify the hardening mechanisms involved.

Concern has been raised about the use of light ions regarding the degree to which light ions simulate the neutron irradiation. We have modeled these differences by considering the cascade size distributions caused by different irradiating particles, and, in particular, the cascade annealing and associated defect recombination. Our conclusion is that, according to displacement cross sections, light ions are only

---

[33] Physics Division.

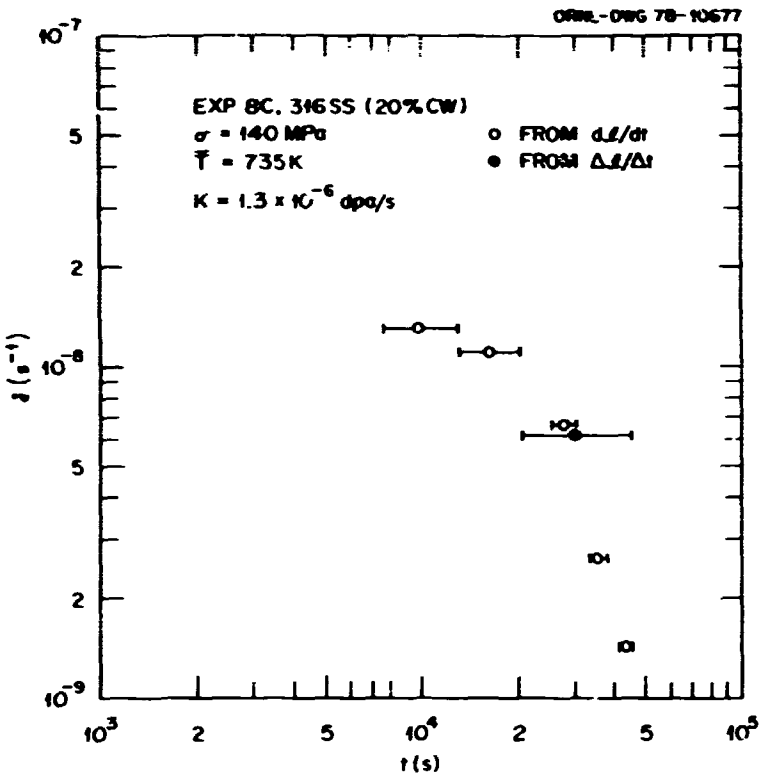

Fig. 4.13. Irradiation Creep Rate of 20%-Cold-Worked-Type 316 Stainless Steel Under 60 MeV α-Particle Irradiation.

slightly more effective than neutrons (by a factor of ∿2) in producing free interstitials able to contribute to the irradiation creep process. This is consistent with the available data on the creep under light ions of preirradiated stainless steel. Differences between the inelastic scattering processes under neutron and light-ion irradiation are currently being considered.

One important side benefit of the development of the Irradiation Creep Facility (ICF) is that an apparatus capable of detecting the extremely low rates of deformation associated with irradiation creep can also detect, with high precision, thermally induced deformation. While characterizing the vibration sensitivity of the ICF, we made the length vs time measurements shown in Fig. 4.14. This gives an indication of the high degree of accuracy available for monitoring mechanical behavior when the specimen is not being subjected to irradiation.

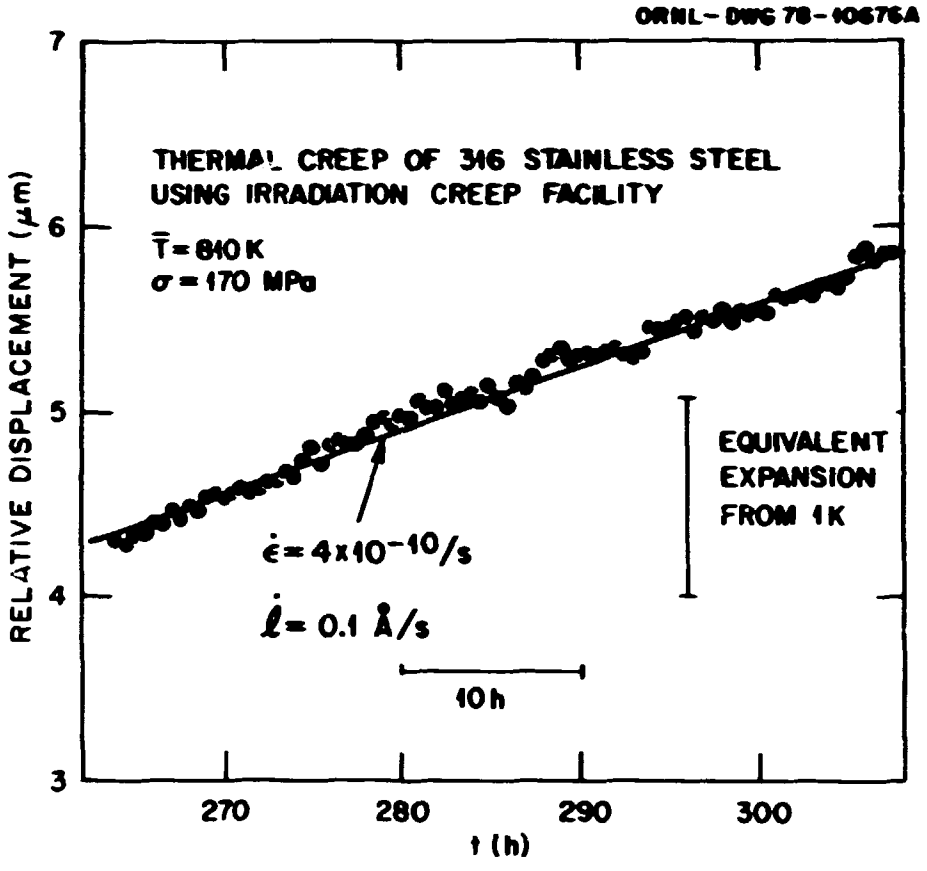

Fig. 4.14. Thermal Creep Testing of Type 316 Stainless Steel During Calibration-Resolution Experiments for the Irradiation Creep Facility.

4.2.14 The Effect of Thickness on the Creep of Type 316 Stainless Steel Tested in Vacuum and in Helium — P. G. Jung[34] and T. C. Reiley

To perform irradiation creep tests using light ions (see Sect. 4.2.13) requires thin specimens, about 100 μm. One should consider three areas in which thickness may affect the results of elevated-temperature mechanical tests: (1) the interaction of dislocations with the surface, (2) the ease of grain boundary sliding for specimens having grain boundaries traversing or nearly traversing the specimen thickness, and (3) chemical interaction with the test environment.

[34]Guest Scientist from KFA, Jülich, FRG.

To test the degree to which specimen thickness affects creep properties, a vacuum creep apparatus was modified to accommodate thin specimens. It was modified such that an entire loading and strain measuring system could be housed in the vacuum system. The specimens were spring-loaded and heated with a resistively heated tantalum enclosure. Tests could be performed in vacuum (<10 μPa, 10^{-7} torr) or in purified helium. An oxygen meter showed the helium to contain less than 1 ppm O_2 during these experiments.

The results of experiments performed on type 316 stainless steel (20% cold-worked) are shown in Fig. 4.15. The specimens tested had grain sizes of about 10 μm. This demonstrates that for the test temperature and stress chosen, 538°C (811 K) and 140 MPa, respectively, there is no marked effect of thickness between 25 and 200 μm in helium or vacuum.

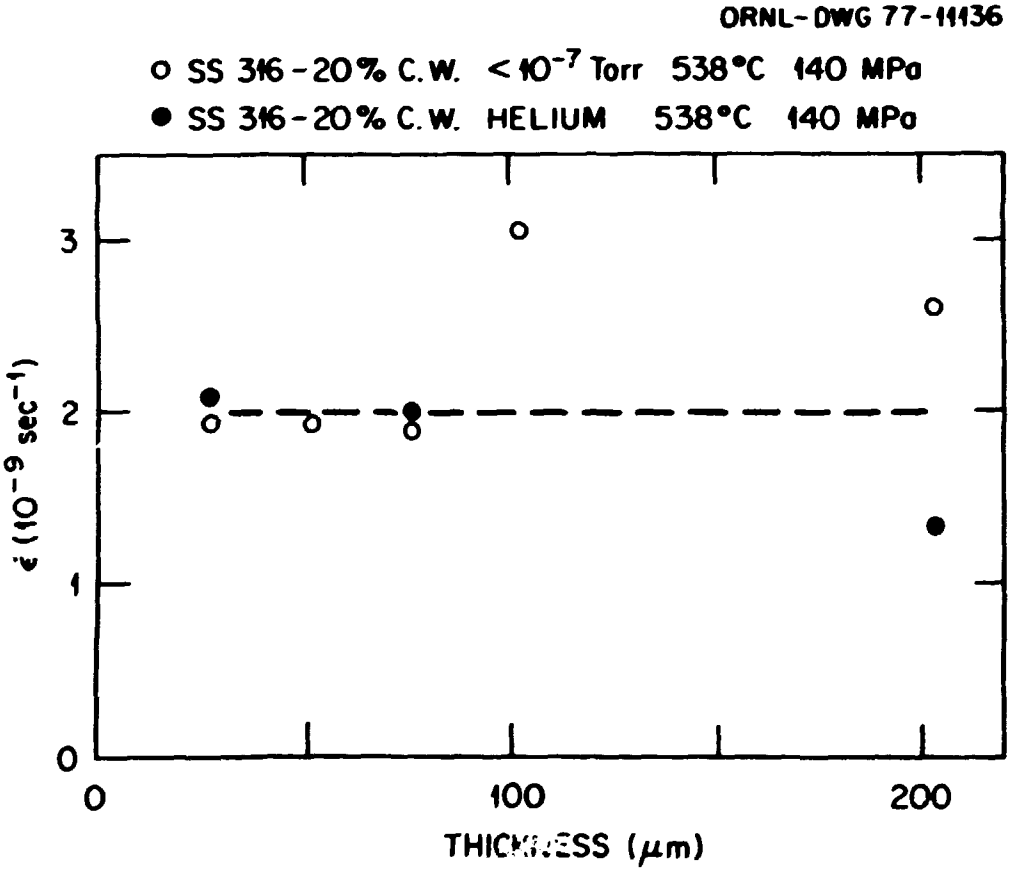

Fig. 4.15. Thermal Creep of Thin 20%-Cold-Worked Type 316 Stainless Steel, Measured at about 170 h; Grain Size ≤10 μm.

4.3 FACILITY AND TECHNIQUE DEVELOPMENT

4.3.1 Electron Microscopy Instrumentation

4.3.1.1 Electron Energy Loss Spectroscopy — N. J. Zaluzec

The addition of an Electron Energy Loss Spectrometer (EELS) to a transmission electron microscope (TEM) results in a unique analytical system. Characteristic information about the specimen is derived from changes in the angular and energy distribution of electrons transmitted through a thin sample. Measuring the distribution of inelastically scattered electrons can provide elemental information from microvolumes of material. Of particular significance is the ability to perform light-element analysis such as detection of the interstitials C, N, and O, which cannot be measured with conventional x-ray energy-dispersive techniques. Additional information about the atomic and electronic structure of the specimen can be obtained from measurements of the oscillatory extended fine structure on absorption edges (EXAFS) as well as by the shape and position of characteristic plasmon loss peaks. Spatial resolution of this technique is limited only by beam broadening effects within the specimen and can be less than 5 nm.

From the three types of spectrometers considered we chose the magnetic sector design. Electron-optical calculations on the relationship between design parameters and spectrometer performance were carried out, and a design was developed for the spectrometer pole piece. The spectrometer is of the $\pi/2$ magnetic sector type, with a central radius of 200 mm. The entrance and exit planes of the pole piece are tilted with respect to the incident beam and shaped to provide both double focusing and partial second-order aberration correction. Double focusing — that is, focusing in the plane of dispersion (plane of the figure) as well as in the plane perpendicular to the dispersion plane — is critical to the optimization of the system because of the low level of inelastic scattering relative to the unscattered beam. The calculated resolution of the spectrometer is 2.3 eV when object and image slits are 5 μm in diameter, while the

uncorrected second-order aberrations at an input divergence of 10^{-3} rad have been calculated to be less than 0.25 eV. Construction of a spectrometer to these specifications is now in progress.

4.3.1.2 Interfacing Data Acquisition Equipment for Analytical Electron Microscope Investigations — N. J. Zaluzec and R. W. Carpenter

The usual output of electron microscope investigations consists of a series of micrographs, which show microstructural features. In some instances accurate quantitative analysis requires numerical results rather than photomicrographs. The general procedure has been to obtain such results using microdensitometer traces of the image details. Direct digitization through the use of photoelectron multiplier tubes provides more accurate information and can detect even single electrons. In addition to the recording process some type of data acquisition system is reqired for both storage and analysis of information. For the case of analytical electron microscopy (AEM) this information problem becomes even more acute. Not only is the microscopist interested in quantitative analysis of image detail (TSEM) but also relative intensities in electron diffraction patterns (TSED), accurate measurement of characteristic x-ray emission using x-ray energy dispersive spectroscopy (XEDS) and the analysis of complex electron energy loss spectra (EELS). In order to handle this large data acquisition, storage, and analysis problem, a dedicated minicomputer has been acquired and is being interfaced to the microscope. The computer system (PDP 11/34) consists of 16 K words of CMOS memory, a dual floppy disk mass storage system, an LA 36 Dewriter terminal, and a Tektronics 4010-1 Graphics Display Terminal.

4.3.1.2.1 Software Developments. Interactive software developed at the University of Illinois[35] has been modified and is being introduced into our system, which provides a range of graphics as well as data analysis capabilities. Additional software allowing data transfer between the computer system and the KEVEX X-ray Multichannel Analyzer

[35] N. J. Zaluzec, *An Analytical Electron Microscope Study of the Omega Phase Transformation In Zirconium-Niobium Alloys*, Ph.D. Thesis, University of Illinois, 1978.

has been developed, and expansion of the system capabilities is in progress.

4.3.1.2.2 Hardware Modifications. The x-ray multichannel analyzer (MCA) system obtained from KEVEX has been modified to incorporate an additional data acquisition mode, multichannel scaling (MCS). Included in this modification is an external channel advance system coupled with an analog-to-digital converter, which provides a synchronous interface between the MCS and the electron microscope. Using this system we can obtain digitized line scans of either a transmission image (TSEM) or electron diffraction pattern (TSED); it will also be adapted for recording electron energy loss spectra (EELS). In addition to the sequential addressing, the microscope scanning system has been modified to allow operation interactive control of the scan length, position, and relative orientation, all of which can be observed on the microscope fluorescent screen or on a CRT display.

4.3.1.3 High-Voltage Electron Microscope (HVEM) Modification for Side-Entry Conversion — E. A. Kenik

Equipment for the conversion of the 1-MV microscope from top entry to side entry has been installed. The side-entry configuration will allow a wide range of in-situ studies to be undertaken, including gas-solid reactions, deformation, and radiation damage. The high tilt capabilities of the basic stage will facilitate defect and precipitate analysis. A variety of specimen holders compatible with the stage are presently on hand, and several others are on order. These include:

1. ambient single-tilt holder, ±60° tilt;
2. ambient double-tilt holder, ±60° tilt on main axis, ±45° tilt on orthogonal axis;
3. single-tilt heating holder, fast thermal response, ±50° tilt, room temperature to 1300 K range, ±5 K stability, compatible with environmental stage;
4. double-tilt heating holder, ±30° tilt on main axis, ±30° tilt on orthogonal axis, room temperature–1100 K range, stage temperature monitored ±2 K stability;

5. single-tilt hard straining holder, ±30° tilt;
6. single-tilt hard straining heating holder, ±15° tilt, room temperature–900 K range, ±5 K stability.

All the double-tilting holders have orthogonal tilt axes.

In addition, an environmental cell has been obtained. It will allow gas-solid reactions to be studied in situ.

4.3.1.4 High-Voltage Electron Microscope Modifications for Energy-Dispersive X-Ray Analysis — E. A. Kenik, N. J. Zaluzec, and J. Bentley

In support of theoretical calculations on the improvement of x-ray analysis at high voltages (see Sect. 4.3.2.4), experiments on the HVEM have been planned. Several modifications of the system have been designed and are being constructed. These include:

1. electrically isolating flanges to interface the x-ray detector to the HVEM.
2. a low-atomic-number specimen holder to minimize extraneous x-ray signals,
3. an x-ray collimator for the detector,
4. an aperture system to minimize high-energy x rays and electron tails incident on the specimen and holder.

Initial studies should be completed by the end of the fiscal year.

4.3.2 Electron Microscopy Research

4.3.2.1 Studies of Contamination Processes on Thin Metal Foils — J. Bentley and E. A. Kenik

A series of experiments is in progress to study the processes occurring in the formation of contaminants on metal foils, which can occur when high-current-density probes are used. Contamination is an important obstacle preventing the realization of the full potential of an analytical electron microscope (AEM). Major consequences of contamination include: (1) a lack of spatial resolution and errors in quantitative analysis during energy-dispersive x-ray analysis;

(2) severe limitations on micro-microdiffraction techniques;[36] (3) preclusion of detailed analysis on a single small region since image detail is totally obscured in a short time; (4) errors in and possibly prevention of electron energy loss spectroscopy (Sect. 4.3.1.1) at high spatial resolution.

Studies by other workers[37,38] indicate that the mechanism of contamination involves the surface migration of hydrocarbon molecules to the electron beam, where they are polymerized. The source of the hydrocarbon molecules is either the instrument vacuum or contamination carried into the high-vacuum region on the specimen (and/or holder), or both.

Modifications to the vacuum system of the JEM 100C AEM were made to minimize the instrumental contribution to contamination. As a result of these changes, routine pressure of about μPa (1×10^{-7} torr) is now achieved. Auger electron spectroscopy on aluminum specimens indicated little difference in the surface contamination of freshly electropolished specimens and specimens examined following insertion into the AEM.

4.3.2.2 Small-Angle Electron Scattering in the Transmission Electron Microscope[39] — R. W. Carpenter, J. Bentley, and E. A. Kenik

The primary advantages associated with the use of electrons for small-angle studies in a transmission microscope are first, that a real-space image and high-angle diffraction pattern of the scattering

---

[36]R. W. Carpenter, J. Bentley, and E. A. Kenik, "Analytical Electron Microscopy Investigation of Structural and Spatial Composition Variation in Lamellar Multiphase Alloys," pp. 411–22 in *Scanning Electron Microscopy*, Vol. 1, IIT Research Institute, Chicago, 1977.

[37]J. T. Fourie, "Contamination Phenomena in Cryopumped TEM and Ultra-High Vacuum Field-Emission STEM Systems," pp. 53–60 in *Scanning Electron Microscopy*, Vol. I, IIT Research Institute, Chicago, 1977.

[38]W. A. Knox, "Contamination Formed Around a Very Narrow Electron Beam," *Ultramicroscopy* 1: 175–80 (1976).

[39]Summary of paper to be published in *Journal of Applied Crystallography*.

object can be easily obtained, and second, that very high angular resolution is possible. Further, in a microscope, small-angle scattering around high-angle Bragg maxima can be studied as easily as small-angle scattering around the direct beam. These advantages accrue to the electron case because electrons can be easily focused by electromagnetic lenses.

Scattering at small angles around the direct or Bragg beams can be examined in several ways. Two general requirements must be satisfied: sufficient angular resolution must exist and the effective camera length, L, must be large enough. Angular resolution is principally determined by the incident beam divergence, $\alpha = r/L$, where r is the radius of the direct beam in the diffraction pattern. The electron probe-forming lenses (usually the first and second condensers) are operated near maximum field strength to form a strongly demagnified image of the electron gun crossover above the specimen. A small second condenser aperture is also used to reduce further the incident beam divergence. The effective camera length, L, is determined by diffraction pattern magnification with the image forming lenses following the specimen.

The two methods most often used for examination of small-angle scattering in a microscope are the long-camera-length method and the well-known selected-area diffraction method. The long-camera-length method requires that the objective lens be switched off, and an intermediate lens is usually used to form the diffraction pattern in the object plane of the projector lens. Camera lengths attainable by this method are high, up to about 150 m, and the highest angular resolution has been demonstrated by use of this method. We have easily resolved many orders of Bragg maxima from a chromium-shadowed cross-ruled grating replica of 2160 lines/mm, corresponding to a "two-dimensional" crystal with a "lattice constant" of 463 nm. The angular resolution at the low-order Bragg maxima was 1.7 μrad. Small-angle scattering at somewhat shorter camera lengths can be observed by the well-known selected-area diffraction (SAD) method. In early transmission microscopes with three-lens imaging systems, camera lengths for SAD

patterns were limited to about 0.8 m. In newer instruments having four- or five-lens imaging systems, camera lengths of up to 10 m have been obtained and longer lengths may be possible. Angular resolution for this method is usually poorer than for the first method described, because the illumination system is operated with lower lens excitations, closer to conditions used for imaging. Typically, angular resolution in the range 0.1 to 1.0 mrad can be achieved by using a small condenser aperture and over-focusing the second condenser lens. This is adequate for study of many phenomena of interest in inorganic crystals. The advantage of the SAD method relative to the long-camera-length method lies in the relationship of the real-space image of the specimen area from which the small-angle pattern is formed. Small-angle patterns can be taken from well-defined areas in the image on the order of 0.5 μm in diameter by the SAD method, while the specimen area contributing to a small-angle electron scattering pattern (SAES) by the long-camera-length method is considerably larger.

An example using the SAD method is shown in Fig. 4.16. The specimen was a Ta-8% W-2% Hf alloy internally oxidized in low-pressure oxygen at 1000°C. The oxygen formed a dense array of coherent clusters with hafnium through the specimen volume. The image shows the clusters arranged in the well-known tweed morphology. The diffuse intensity distribution in the SAES pattern extends about $0.15a^*$ from the (020) and $(23\bar{1})$ Bragg positions, where a^* is the reciprocal lattice constant, and is more intense at the high-angle side of the Bragg positions. The asymmetry in the intensity results from the interstitial nature of the strain fields at the Hf-O clusters. The rotation of the double-lobed diffuse intensity distribution away from the $[23\bar{1}]$ direction is caused by the elastic anisotropy of the alloy lattice.

Measurements of the intensity in such SAES distributions relative to intensity in the Bragg peaks can be used to calculate the magnitude of the cluster strain fields in the lattice in simple cases. Some measurements[36] of this kind have been made by the Grigson method. Further experiments are in progress using a multichannel analyzer to record the intensity distribution (Sect. 4.3.1.2).

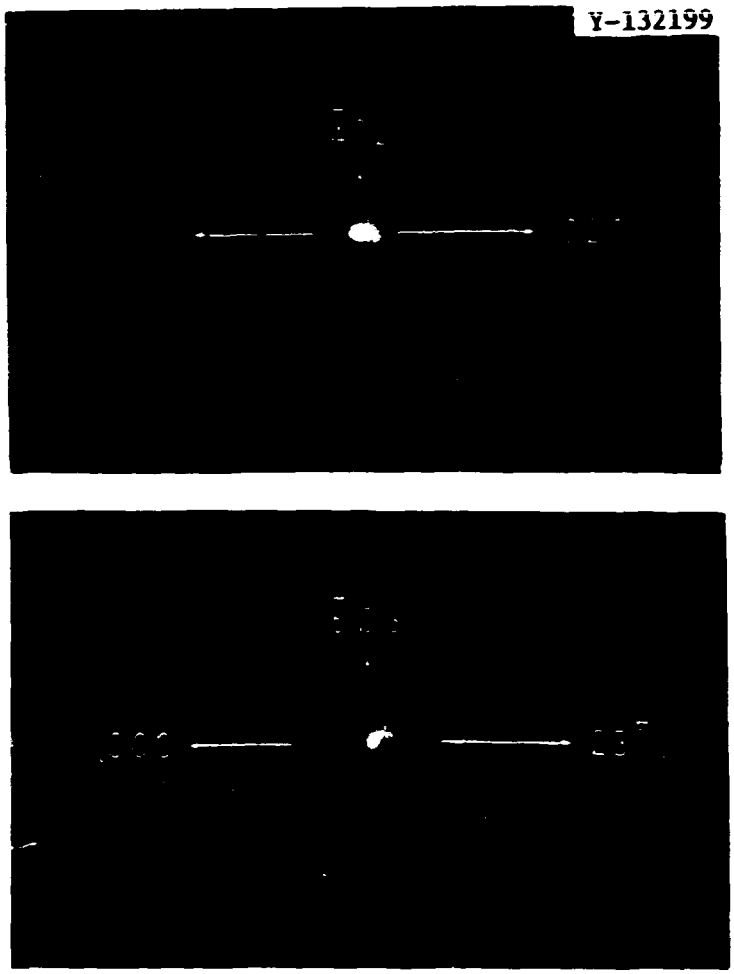

Fig. 4.16. Diffuse Electron Scattering Around [020] and [231] Bragg Reflections of a Ta–8% W–2% Hf Alloy Containing 3000 ppm O. The diffuse scattering is a result of strain in the lattice caused by the presence of oxygen.

4.3.2.3 Application of Weak Beam Dark Field (WBDF) Imaging to Radiation Effects in Alloys[40] — R. W. Carpenter and M. H. Loretto[41]

Observations of dislocations in the immediate neighborhood of θ′ precipitate interfaces in neutron-irradiated Al–4% Cu alloys have been made by WBDF and bright field (BF) transmission microscopy. This

[40]Summary of paper to be published in the *Proceedings of the Ninth International Congress on Electron Microscopy*, Toronto, 1978.

[41]Guest scientist from the University of Birmingham, England.

alloy is more resistant to void swelling than elemental aluminum as a result of the presence of the initially semicoherent precipitate (see Sect. 4.2.7). Postirradiation TEM examination showed, in BF, that some changes had occurred in the appearance of the precipitate-matrix interface, but contrast overlap from the precipitate itself prevented any detailed observations. In images of the same area in WBDF using a matrix reflection the precipitate contrast was suppressed and the nature of the changes at the interface was clearly visible. An example is shown in Fig. 4.17. At "A" in the WBDF micrograph a number of dislocation loops are adjacent to the interfaces; many of these loops have flat sides where they intersect the interface. These intersections are part of the first stage of precipitate coherency loss under irradiation. The BF micrograph shows the precipitate contrast to extend over the regions occupied by the dislocation loops and "covers up" the loop contrast. The reduction in precipitate contrast in WBDF is a result of the low sensitivity of WBDF contrast to lattice deformation of slow spatial variation. The lattice deformation from a dislocation is relatively local and produces a sharp image. This imaging method is being used to study coherency loss in Al—4% Cu and in several other alloys.

4.3.2.4 Optimum Conditions for X-ray Microanalysis in a TEM — E. A. Kenik, N. J. Zaluzec, and J. Bentley

The ultimate sensitivity of microanalysis using x-ray emission depends on selecting those experimental conditions that maximize the measured peak-to-background (P/B) ratio. Theoretical calculations[35] of the variation in the P/B ratio have been extended to the case of irradiation by 1-MeV electrons. The results show a monotonic increase in P/B with increasing overvoltage for all elements. Increases in P/B as much as 2.5 times the 100-keV results are expected, indicating the possibility of increased sensitivity for x-ray analysis on HVEMs. Modifications to the Hitachi 1-MV HVEM are now in progress to examine the feasibility of such an experiment.

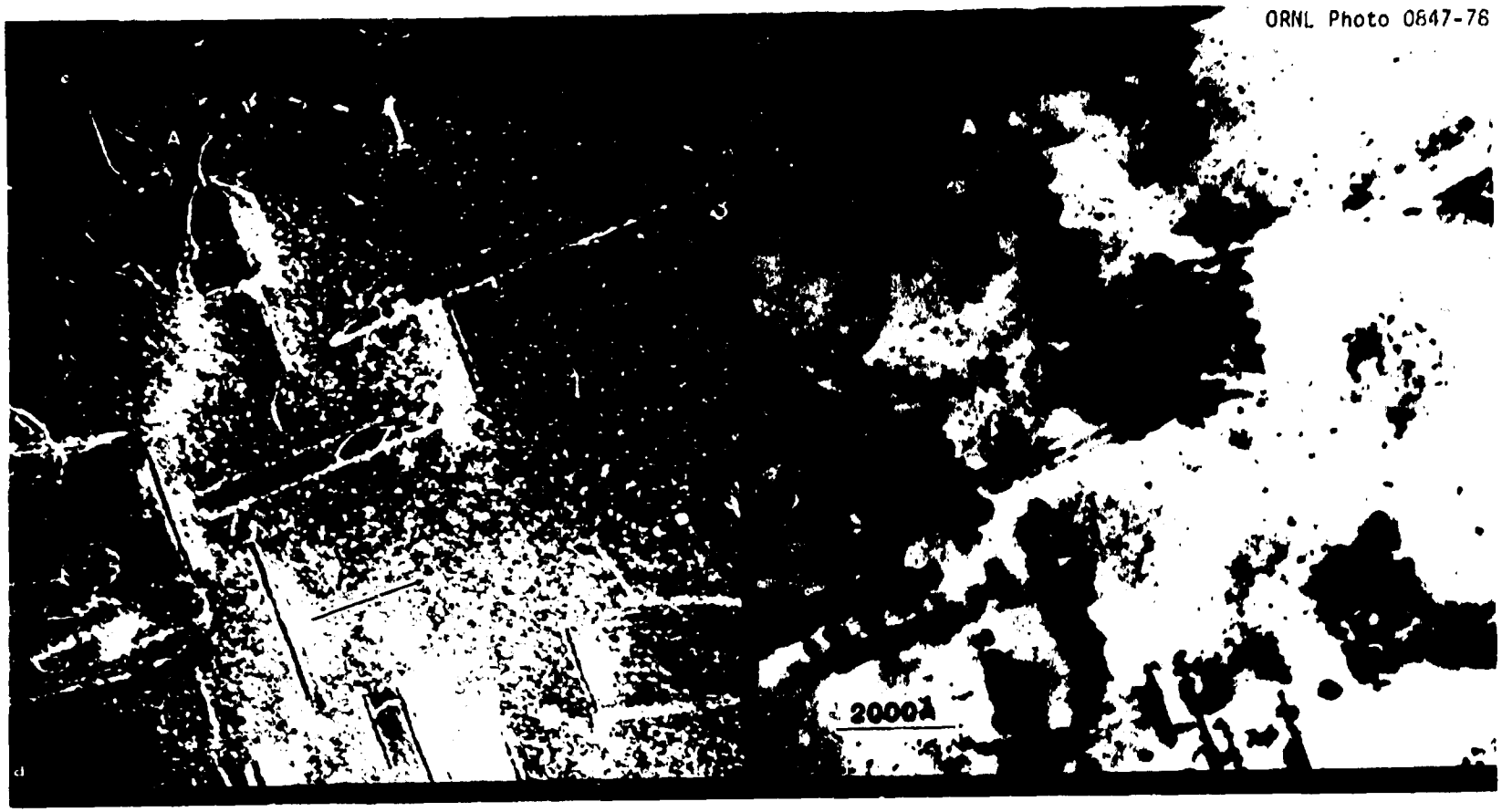

Fig. 4.17. Transmission Electron Microscope Images of Dislocation Loops at θ' Interfaces. (a) WBDF, (b) BF. Note suppression of θ' strain contrast in (a) relative to (b), and loops at A. Neutron dose 3×10^{25} n/m^2 at 57°C (330 K). $B \approx [103]$, $g = [020]$.

4.3.2.5 Identification of Precipitate in Lithium-Doped Magnesium Oxide — J. Bentley and J. Narayan[42]

Analytical electron microscopy has been used to identify Li_2O precipitate in Li-doped MgO. The low concentration ($\sim 2.5 \times 10^{19}/m^3$) and diameter ($\sim$22 nm) of the precipitate particles precluded conventional identification by selected-area diffraction. Moiré patterns were obtained for several combinations of diffracting vectors and beam directions. Fringes of 1.7 nm periodicity obtained with (220) reflections indicated a probable precipitate lattice constant of either 0.461 or 0.378 nm. To determine the lattice constant of the precipitate and its crystal structure uniquely a direct observation of the diffraction pattern is required.

A scanning transmission image was obtained, and the probe stopped near the precipicate particle. Final adjustments to the second condenser focus, astigmatism correction, and positioning of the probe were then made while the image detail in the (000) diffraction disk was observed. The crossover of the probe was positioned exactly in the specimen plane only for the short times necessary to photograph the diffraction pattern, in order to minimize the contamination. The diffraction patterns were recorded at 120 kV with a 20-μm-diam condenser aperture and an incident beam divergence of about 0.7 mrad. The minimum probe diameter under these conditions is expected to be about 20 nm.

Electron diffraction patterns indicated a cube-on-cube orientation of the precipitate with a lattice constant of 0.46 nm, which corresponds to Li_2O. Tilting experiments helped the interpretation of double diffraction effects, and the observed absence of 200-type reflections from the precipitate is also consistent with the CaF_2 (fluorite) structure of Li_2O. The identification of the precipitate as Li_2O appears certain. From the average particle size and concentration of the precipitate, we deduce that most of the 400 at. ppm Li is contained in the Li_2O precipitate.

---

[42]Solid State Division.

This positive identification together with results from high-temperature annealing and electron irradiation studies confirm that the precipitate is a source of lithium ions that produce stable $[Li]^0$ centers and result in a significant suppression of radiation damage.

4.3.3 Operation and Improvements of the Dual Van De Graaff Irradiation Facility — M. B. Lewis, M. B. Inman, and G. F. Wells[33]

The dual Van de Graaff irradiation facility is used extensively for ion implantation and studies of radiation damage of alloys. During the past year nickel beam currents have been delivered on more than 100 target assemblies, each containing up to nine specimens. The total target specimen irradiation damage amounted to approximately 50,000 dpa. The 5-MV Van de Graaff was used exclusively for nickel ion bombardments. Approximately 70% of this machine time was allocated to alloy development programs and 30% to the basic research program. The total machine use during the past year was about 1100 h.

The 0.4-MV Van de Graaff was used in one of three modes: (1) implantation of alloy specimens with helium and/or hydrogen before nickel ion bombardment, (2) implantation of specimens simultaneously with nickel ion bombardment, and (3) nuclear microanalysis in an ion scattering chamber. The total machine use was approximately 540 h during the past year, of which about 200 h was used for radiation damage experiments, while the remainder was used to develop a new energy ramping system and to carry out nuclear microanalytical experiments.

Upgrading work on the energy ramping system consisted of two parts: (1) The sawtooth or linear generator was replaced by a sine wave generator. This improved considerably the depth profile uniformity during ion implantation. (2) The mechanical focus lens drive mechanism was replaced by a light pipe and pulsing light control. The new system promises smoother and more reliable operation during energy ramping.

Additional upgrading work consisted of installing a two-axis goniometer in the ion scattering chamber. This goniometer makes it possible to orient the target with 0.1° precision about two independent

axes. This system has been calibrated with silicon and vanadium crystals by locating some of their crystallographic axes. In addition, a target chamber for light-ion backscattering is being assembled on the 5-MV beam line.

4.4 NUCLEAR MICROANALYSIS

4.4.1 The Source of Oxygen in the Anodization of Vanadium[43]

M. B. Lewis and R. A. Perkins[44]

Since vanadium oxide is partly soluble in water, a special anodization technique using a solution with a minimum amount of water had previously been developed. However, the source of oxygen that is transferred to the anode from this kind of solution is not well understood. A better understanding is needed in order to anodize metals with isotopically enriched oxygen for later depth profiling or tracing oxygen migration in metals and oxides.

Single crystals of vanadium were anodized in an acetic acid solution to trace the true source of oxygen in the resulting oxide film. The solution contained acetic acid, water, and sodium tetraborate. The acetic acid and water were separately tagged with ^{18}O in two different experiments. The isotopic contents of the resulting films were measured by a nuclear microanalysis method utilizing the $^{16}O(d,p)$, $^{18}O(d,p)$, and $^{18}O(p,\alpha)$ reactions. The results were compared with those for zirconium conventionally anodized in an ^{18}O-enriched water-based solution. The results showed that the oxygen probably came from the sodium tetraborate during the anodization of vanadium.

4.4.2 Implantation and Depth Profiling of Deuterium and Helium — M. B. Lewis

Irradiation of alloys using the technique of simultaneously implanting helium (and more recently deuterium) while carrying out

---

[43]Summary of a paper submitted to *Journal of Electrochemical Society.*

[44]Now at Owens-Corning Fiberglas, Granville, Ohio.

heavy-ion bombardments requires a knowledge of the helium and deuterium depth profiles. Such profiles can be measured nondestructively by nuclear microanalytical methods.

A target chamber with an IONIX 3072 target positioner has been set up on the 0.4-MV Van de Graaff and has been used to measure helium and deuterium depth profiles in metals. Nickel, stainless steel, and uranium targets were implanted with helium or deuterium to a level of about 1 at. %. In one case, the implantation was carried out with a 0.2 to 0.4 MeV ion energy range using a sine wave function generator to vary continuously the accelerator energy. The resulting profile showed good depth uniformity between the limits 400 and 850 nm.

In another experiment, the helium was first implanted at 0.3 MeV in a nickel specimen and the profile measured. Another implantation was carried out subsequently while a target was held at 700°C; a third target was simultaneously bombarded with 4-MeV nickel ions and also maintained at 700°C. In the latter cases the measured profile when compared with the first showed appreciable depth broadening. For example, the RMS depth deviation in the room-temperature case was 0.10 μm, whereas the 700°C case showed 0.15 μm and the 700°C plus nickel ion bombardment showed 0.17 μm. In all cases the center of the distributions was 0.65 μm.

In a third experiment, currently in progress, samples of nickel, steel, and uranium are being implanted with hydrogen at room temperature. Some will be profiled, heated, and reprofiled to study trapping. In one case, preirradiation with nickel ions has been carried out to see how effectively irradiated material can trap hydrogen.

4.5 COOPERATIVE STUDIES WITH UNIVERSITIES AND OTHER RESEARCH ORGANIZATIONS

Several groups at universities and other research organizations are taking advantage of the unique facilities available in the Radiation Effects and Microstructural Analysis Group.

The high penetrating power of the 1-MV electron microscope has attracted substantial interest in the biological community. W. B. Lushbaugh, Medical University of South Carolina, Charleston, is using the microscope to study parasites that cause diarrhea in animals and humans. The thick sections that may be viewed at high voltages allow examination of specimens attached to the intestine. R. Bagby and R. Abercrombie, University of Tennessee, Knoxville, are investigating the mechanism of contraction of muscles using thick-section stereo pairs. A. L. Olins and D. E. Olins, University of Tennessee, Oak Ridge Graduate School for Biomedical Science and ORNL Biology Division, are also using thick-section stereo pairs to examine the spatial arrangement of the 20-30-nm chromatin fibers in sections of chicken erythrocyte nuclei.

Members of the staffs of the Westinghouse Advanced Reactor Division and the General Electric Breeder Reactor Department have used the Van de Graaff facility for heavy-ion damage in materials of interest to the Fast Breeder Reactor Cladding-Duct Alloy Development Program. Additional irradiations of vanadium have been carried out for J. Schneider and M. S. Wechsler, Iowa State University. Metal oxide targets were irradiated for J. Narayan, ORNL Solid State Division.

A major neutron irradiation experiment currently in EBR-II contains specimens for J. Moteff, University of Cincinnati, and for D. Seidman, Cornell University. Specimens from previous irradiation experiments are being examined at several laboratories in this country and abroad. R. W. Gilbert, Chalk River Nuclear Laboratories, Canada, is completing a study of specimens of zirconium and Zircaloy. A. Jostsons, Lucas Heights Laboratory, Australia, is investigating damage in various grades of neutron-irradiated zirconium and titanium. He is also working with K. Farrell, ORNL, in a cooperative study of the fluence dependence of damage in pure aluminum and in dilute aluminum-silicon and aluminum-indium alloys.

R. L. McConville, University of Illinois Center for Electron Microscopy, is studying neutron damage in a series of magnesium-aluminum alloys. J. T. Stanley, Arizona State University, Tempe, is

using magnetic measurements to investigate the development of ferrite in neutron-irradiated stainless steels. W. Ellis, University of Florida, Gainesville, is looking into the possibility of using γ-γ angular correlation measurements to probe low-swelling alloys.

Specimens of neutron-irradiated aluminum, aluminum-silicon, and aluminum-magnesium alloys have been sent to J. D. McGervey, Case Western Reserve University, for investigation by positron annihilation techniques. C. L. Snead, Jr., Brookhaven National Laboratory, is also using positron annihilation measurements to investigate vacancy characteristics in a series of dilute binary nickel-base alloys that are being included in ORNL irradiation experiments. Damage structures will be examined for systematic variations that can be related to the positron annihilation measurements.

D. J. Bradley, Michigan State University, and G. R. Gessel, Iowa State University, completed Ph.D. research programs while working in the Group under ORAU graduate fellowships.

Joint theoretical studies are being conducted with W. G. Wolfer, University of Wisconsin, Madison, and A. D. Brailsford, Ford Motor Company. Wolfer is also consulting with us on use of eccentric pressurized tubes to determine stress effects on swelling and on development of techniques to use Van de Graaff irradiations to estimate irradiation creep rates.

J. J. Wert, Vanderbilt University, and C. L. White, ORNL, are conducting a joint investigation of the mechanisms of grain boundary fracture resulting from solute and impurity segregation. H. L. Marcus, University of Texas, Austin, has consulted with us on fracture and fatigue problems. We have supported an undergraduate thesis project under the direction of Marcus at the University of Texas to evaluate miniature specimen designs.

5. ENGINEERING MATERIALS SCIENCE

5.1 FUNDAMENTALS OF WELDING AND JOINING — G. M. Goodwin and J. M. Leitnaker

All energy systems contain joints. Metals, of different or the same kind, must be joined by some kind of welding process for reasons of economy. Unfortunately, the region in or near the weld constitutes a portion of the system overly sensitive to failure. It follows that this problem offers significant opportunities for improving the reliability and cost effectiveness of energy systems. To this end, the Materials Science and Materials Engineering Sections have developed a joint program in this area. The eventual goal, of course, is to be able to predict the achievable property limits obtainable for a particular joining problem.

A weld has three regions of interest: the weld itself, the metal(s) being joined, and the region between the weld and the metal being joined, that is, the heat-affected zone. The time period of interest begins during any preconditioning and extends through the life of the material. Materials of interest include both austenitic and ferritic alloys, primarily iron and nickel base.

We are investigating phase transformations that occur within weldments. The initial phase transformations involve solidification. Further transformations occur, both initially on cooling and on aging at service temperatures. Numerous such transformations occur; a few have been partially quantified. The thrust of the program is to quantify as many as possible and to establish their effect on properties. In this way the ability to predict and control properties of welds will be obtained.

5.1.1 Weld Pool Solidification Control Studies — S. A. David

This research is aimed at gaining a fundamental understanding of the basic solidification characteristics, that is, development of structure and segregation and its control in austenitic stainless steel weldments. Particular emphasis will be given to investigating welding

parameters that influence microstructural variability in welded structures, such as cooling rate and chemical compositions. Solidification structures will be related to the stability of the microconstituents, both equilibrium and nonequilibrium, and their effect on mechanical properties.

5.1.1.1 Solidification Behavior of Type 308 Stainless Steel Filler Metal

A series of experiments involving a combination of thermal analysis and interrupted solidification were carried out to understand the solidification behavior of type 308 stainless steel weld metal. Results indicate the sequence of phase occurrence during solidification to be

$$L \rightarrow L + \delta \rightarrow L + \delta + \gamma \rightarrow \gamma + \delta \ .$$

The ferrite observed at room temperature has been identified as the untransformed primary δ-ferrite that formed during the initial stages of solidification. The mode of freezing and the extent of solid-state diffusion control the amount and distribution of ferrite. Experimental evidence indicates extensive solid-state transformation due to homogenization during solidification and cooling from the nonequilibrium solidus to room temperature.

5.1.1.2 Solidification Behavior of Model Austenitic Weld Systems

A program to understand and model solidification behavior of austenitic stainless steel weld metal using the Fe-Ni-Cr system as a model system is in progress. Ternary Fe-Ni-Cr alloys and alloys with systematic additions of other alloying elements have been prepared. Experimental investigations of these alloy systems will contribute to the understanding of the role of various alloying elements on the solidification structure development and formation and stability of the microconstituents in austenitic stainless steel.

5.1.2 Transformation Reactions of Aged Weldments — J. M. Leitnaker

5.1.2.1 Transformation of δ-Ferrite to Sigma — J. M. Leitnaker, J. Bentley, and D. P. Edmonds

On aging, ferrite transforms to sigma phase, a hard intermetallic phase, which is generally believed to be deleterious to metallic structures. The formation of sigma phase generally leads to a decrease in overall ductility, with cracks opening up along the austenite-sigma boundary.

Stiegler et al.[1] have shown a large and unexplained variability in the rate of sigma phase formation in type 308 stainless steel weldments. The variability enabled them to show that cracks opened up during creep tests only in regions in which sigma phase was formed. Specimens that had little or no sigma phase were as strong as and, overall, more ductile than those containing quantities of sigma.

The weld metal 16-8-2 (nominally 16 wt % Cr, 8 wt % Ni, 2 wt % Mo, balance Fe) shows very little if any sigma phase after aging up to 10,000 h at 732°C. Regions of what were ferrite clearly showed that they remained ferrite but after this aging time were surrounded by $M_{23}C_6$. Sigma is not seen optically because the original ferrite contained within the specimens is thin. Thus, the evidence for the absence of sigma phase is negative.

The absence of sigma phase in 16-8-2 welds is consistent with two other factors: overall composition and morphology of the ferrite. The morphology of the ferrite is important for the following reason: if the chromium necessary to form sigma can diffuse to the ferrite-austenite interface, it forms $M_{23}C_6$ more rapidly than it forms sigma phase. Secondly, the overall composition of 16-8-2 is considerably lower in chromium equivalent than is type 308 weld metal; thus, the driving force for formation of sigma phase is lower.

---

[1] J. O. Stiegler, R. T. King, and G. M. Goodwin, "Effect of Residual Elements on Fracture Characteristics and Creep Ductility of Type 308 Stainless Steel Weld Metal," *J. Eng. Mater. Technol.* 97: 245–50 (1975).

5.1.2.2 Transformation of Austenite to Martensite — J. M. Leitnaker and D. P. Edmonds

During cooling, cast weld metal in the composition range of 16-8-2 (16 wt % Cr, 8 wt % Ni, 2 wt % Mo, balance Fe) can undergo a martensitic transformation from the fcc austenite phase to a bcc phase. A useful way of semiquantitatively measuring the amount of the bcc phase present is by magnetic means. We reported previously[2] that the amount of ferrite obtained via the transformation depends on the aging time. Aging the samples at 650 and 732°C results in precipitation of carbides and chi phase, which changes the composition of the matrix and permits additional martensite to form on cooling.

Aging the welds at 482°C produces a different result. Although carbides precipitate and one expects from data obtained at higher temperatures that a martensitic transformation should have occurred, the magnetic measurements produced a negative result. No martensite was believed to have formed in the samples cooled from 482°C. However, thinning the samples and examining in the electron microscope showed the heavily dislocated bcc phase typical of the martensitic phase transformation. Unaged samples of the same composition can be thinned successfully without the transformation; thus, the aging apparently is making the sample susceptible to transformation, as at higher temperatures. We believe this transformation occurs during preparation of the electron microscopy specimens. The thinning of the polycrystalline sample quite likely removes some restraining forces, easing transformation. However, it is perfectly clear that the striking difference in transformation behavior between samples cooled from 650°C and those cooled from 482°C is not understood at present.

---

[2]J.M. Leitnaker and D. P. Edmonds, "Investigation of Ferrite Content of Austentic Welds," *Metals and Ceramics Div. Mater. Sci. Annu. Prog. Rep. June 30, 1977*, ORNL-5311, pp. 30–31.

5.1.3 Precipitation Reactions in Weldments — J. M. Leitnaker

5.1.3.1 Competition of Chromium and Titanium for Carbon — J. M. Leitnaker, J. Bentley, and A. F. Rowcliffe

After aging of type 321 stainless steel, which is basically type 304 with the addition of about 0.5 wt % Ti, both $M_{23}C_6$ and TiC have been observed. Examination of type 321 stainless steel that has been aged 17 years in service in a superheater of a steam plant revealed only TiC and no $M_{23}C_6$. The observation suggests that TiC rather than $M_{23}C_6$ is the stable phase.

Experiments revealed that by limiting the amount of titanium plus carbon in the steel one can produce a homogeneous material in which a titanium level of 5 times the weight percent of carbon is sufficient to prevent the formation of $M_{23}C_6$. The total amount of titanium and carbon must be controlled at levels that depend on the temperature at which solution annealing is to be done. The product of the titanium concentration times the carbon concentration, essentially a solubility product, K, can be expressed as

$$\ln K \left(\frac{\text{moles}}{100\ \text{g}}\right)^2 = 5.8275 - \frac{2.3869 \times 10^4}{T(\text{K})} \pm 0.2750 \qquad (1)$$

over the range 1000 to 1200°C.

As an illustrative example, for 0.5 wt % Ti in solution in a type 321 stainless steel, one could have only 0.005 wt % C in solution at 1050°C according to Eq. (1). This is one-tenth that usually present and demonstrates why manufacturers are unable to eliminate the stringers found in this steel.

5.1.3.2 X-ray Intensities of $M_{23}C_6$ in Steel and Weld Specimens — J.M. Leitnaker, O. B. Cavin, and H. L. Yakel

The crystal structure of $Cr_{23}C_6$ was first described by Westgren[3] in 1933. It is a complicated structure with 92 metal atoms and 24 carbon

---

[3]A. Westgren, "Den kubiska kromkarbidens kristallbyggnad och sammansattnig," *Jernkontorets Ann.* 117: 501–12 (1933).

atoms per unit cell. This phase, which is common in aged steels and labeled $M_{23}C_6$ because of the solution of additional elements, also dissolves molybdenum but appears not to do so randomly. This can be deduced from x-ray intensities, which are observed[4] to be different from those from a random substitution of molybdenum on the $Cr_{23}C_6$ lattice.

Measurement of the relative intensities of a number of lines from x-ray patterns of 15 different specimens of $M_{23}C_6$ revealed that the relative intensities from like samples were reproductible from specimen to specimen within the counting uncertainties. However, the deviation from a calculated intensity for the $M_{23}C_6$ crystal structure was greater than the counting uncertainties for several of the lines. When molybdenum was added to the specimen the variation from the calculated value was greater than when only Fe, Cr, and Ni were present. That is, the calculated intensities for $M_{23}C_6$ in stainless steel specimens do not appear to fit the experimental data, and the arrangement of atoms appears to be less well understood than had been previously supposed.

We are investigating this problem on a number of fronts. We are varying the relative locations of the atoms in the unit cell attempting to obtain a calculated intensity that agrees with the observed intensity. Long-term agings of a number of iron-base alloys containing Cr, Cr and Ni, and Cr, Ni, and Mo are under way. The $M_{23}C_6$ precipitate will be examined as a function of time to see if relative changes in intensities occur. Finally, we hope to get a single crystal of $Cr_{23}C_6$ to investigate the crystal structure of the parent compound.

5.1.3.3 Formation of an Fe_2P and $(Fe,Cr)_2As$-Like Phase on Long-Term Aging of Steel — J. Bentley and J. M. Leitnaker

After long-term aging at 650°C of commerical type 321 stainless steel, a long needle-like precipitate has been seen, as shown in Fig. 5.1.

---

[4]Yu. B. Kuz'ma and T. F. Fedorov, "Phase Equilibria in the System Molybdenum-Chromium-Carbon," *Sov. Powder Metall. Met. Ceram. (Engl. Transl.)* 25(1): 920–22 (1965).

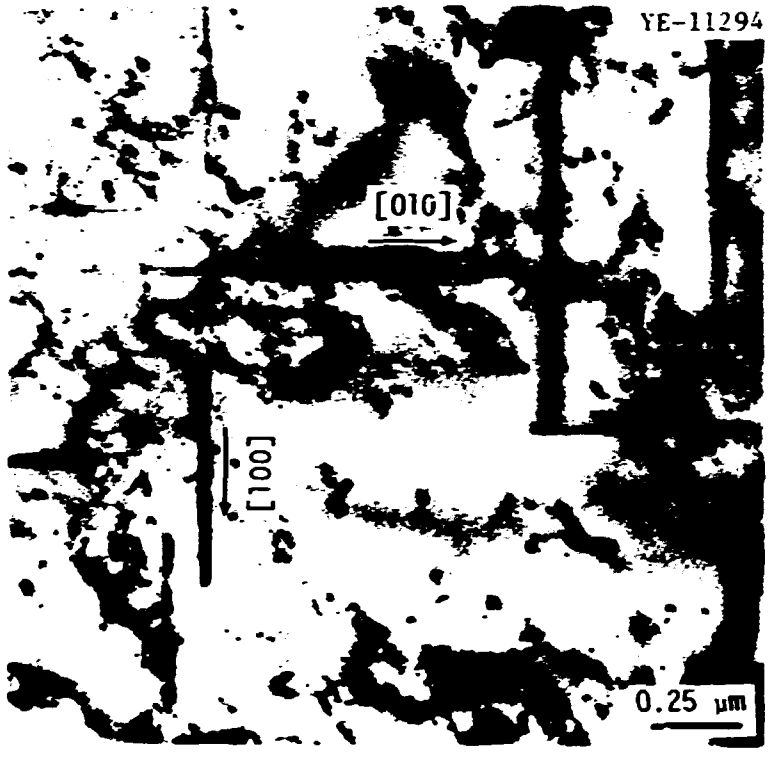

Fig. 5.1. Needlelike Phase in Aged Type 321 Stainless Steel.

Diffraction patterns in several orientations showed that the phase was hexagonal. The orientation relationship between the precipitate and matrix is:

$$(0001)\ \text{precipitate}\ ||\ (001)\ \text{matrix},$$

$$(1\bar{2}10)\ \text{precipitate}\ ||\ (110)\ \text{matrix}.$$

The lattice constants of the phase were determined to be a_0 = 0.608 nm and c_0 = 0.364 nm. The c/a ratio, 0.599, and the hexagonal structure are consistent with the c_{22} structure of Fe_2P. It is also consistent with an $(Fe,Cr)_2As$ structure identified by Hollan.[5] Efforts to extract

[5]L. Hollan, "Étude Structurale et Magnétique D'Arséniures Mixtes M_2As," *Ann. Chim.* 1: 437–48 (1966).

a phase containing phosphorus and arsenic electrolytically have been unsuccessful, possibly because the phase hydrolyzes.

From the chemical analysis we conclude that the steel contains ample arsenic and phosphorus to account for the amount of the phase seen in transmission. It seems reasonable to suppose that the two impurities are combined to yield a $(Fe,Cr)_2(P,As)$ phase. A similar appearing needle-like phase has been seen in irradiated steels, associated with voids,[6] and may be the same.

5.1.3.4 Limits on Formation of Sigma Phase in Austenite — J. M. Leitnaker and J. Bentley

Sigma phase, which forms in austenitic steels, is basically an iron-chromium intermetallic compound, which also dissolves significant quantities of other alloying elements such as Ni, Mo, Mn, and Si. The phase, a complicated structure with 32 atoms per unit cell, forms slowly, and the limits of the one-phase region in multicomponent alloys are not well known because of this sluggishness of formation; experiments require exceedingly long times at temperatures near 650°C.

From short-time experiments, Hull[7] and others have deduced formulas to set limits on the extent of the austenite boundary in the presence of sigma phase. We have examined the limit of the boundary for a type 321 stainless steel. Based on Hull's formula for a limiting "Cr equivalent," we found the limiting equivalent to be 17.9. This value should be rather close, subject only to chemical analysis errors, to a "true" value for a limiting chromium equivalent for type 321 stainless steel. However, for steels varying significantly in composition, Hull's formula is not as accurate as implied by three significant digits in the limiting equivalent. The reason is that additions of such elements as molybdenum do not have a single effect; they not only affect the stability

---

[6] E. E. Bloom and J. O. Stiegler, "Effect on the Microstructure and Creep-Rupture Properties of Type 316 Stainless Steel," pp. 360-80 in *ASTM Spec. Tech. Publ.* 529, American Society for Testing of Materials, Philadelphia, 1973.

[7] F. C. Hull, "Effects of Composition on Embrittlement of Austenitic Stainless Steel," *Weld J. (Miami)* 52: 104-s-413-s (1973).

of the sigma phase, they also affect the activity of the chromium in solution. Thus, a single-valued term in molybdenum, for example, is not appropriate if precision is desired. The epitaxial relationships between sigma and the matrix were examined, and general agreement with the literature noted.

5.1.3.5 Formation of Chi and Laves Phases in Austenitic Stainless Steels — J. M. Leitnaker, D. P. Edmonds, and A. F. Rowcliffe

Both Laves and chi phases occur in austenitic stainless steels containing molybdenum. The Laves appears to be based on a simple binary Fe_2Mo. The chi phase, on the other hand, also requires the presence of chromium. The presence of neither phase is believed to be beneficial. Beneficial elements as silicon or titanium will segregate to and dissolve in either phase. Consequently, there appears to be no reason to permit the presence of either of these phases.

Molybdenum increases the tendency to form sigma phase; however, if the "chromium equivalent" is lowered below some value, sigma phase will not form. The chi and Laves phases can still form if the molybdenum content of the alloy is significant. At about 14 to 14.5 wt % Cr, 9 to 14 wt % Ni, and 2 wt % Mo, for example, no sigma phase will form; however, either chi or Laves phase can form if the molybdenum content is above about 1 wt %. Apparently the nickel content of the matrix determines which phase forms. At 14 wt % Ni the Laves phase forms with greater than about 1 wt % Mo, while at 9 wt % Ni the chi phase forms with greater than about 1 wt % Mo. There must be a three-phase region in which Laves, chi, and austenite coexist.

5.1.4 Precipitation in Nickel Alloys — D. J. Bradley,[8] J. M. Leitnaker, and F. H. Horne[9]

5.1.4.1 Precipitation of Carbon in Nickel and Nickel-Titanium Alloys —

Carbon is an important element in nickel-base alloys. Its synergistic effects wtih other elements can have dramatic effects on

[8]ORAU Graduate Fellow. Present address, Department of Chemistry, University of California, Berkeley.

[9]Department of Chemistry, Michigan State University.

mechanical properties of these alloys. For example, increasing the carbon content of Ni–12% Mo–7% Cr–0.5% Ti alloy from 0.01 to 0.1 wt % changes the creep rupture life by approximately 4 orders of magnitude.

The present study originated from several puzzling observations made in the course of examining nickel-base alloys. Examination of anodically extracted precipitates from nickel and Ni–3% Ti samples, in which all the carbon was known to be in solution at temperature, led to the following seeming anomalies: First, x-ray diffraction intensities on extracted precipitates appeared extremely low. Second, the amount of precipitate extracted appeared to be independent of the temperature between 760 and 1200°C. And, finally, the analyzed composition of the precipitate appeared to be more than 50 wt % C; it consisted of carbon plus absorbed metallic chlorides from the extracting solution.

Careful measurement of several precipitates revealed that nearly all the carbon present in the sample was recovered as a precipitate after quenching single-phase alloys from 1200°C. Only two explanations appear possible: (1) the carbon precipitated on cooling, or (2) the carbon agglomerated during extraction. Diffusion calculations can justify the first possibility. The second possibility seems very unlikely. If the carbon does precipitate on cooling the interpretation of certain internal friction data must be altered.

5.1.4.2 Thermodynamics of Carbon in Nickel and Nickel Alloys[10]

Because of the importance of carbon in nickel alloys, the activity of carbon was measured in pure nickel, in nickel plus titanium, and in nickel plus titanium with varying additions of chromium and molybdenum. The measurements were made at 900, 1100, and 1200°C. Carbon obeyed Henry's law up to the solubility limit in all alloys studied and at all temperatures. Titanium lowered the activity coefficient of carbon in nickel; that is, carbon is more soluble in the nickel-titanium alloy than it is in pure nickel. The increase is largest at 900°C and smallest at 1200°C. Chromium additions also increase the solubility of carbon at a

[10]Summary of D. J. Bradley, *The Thermodynamics of Carbon in Nickel-Based Multicomponent Solid Solutions*, ORNL/TM-6282 (April 1978).

given activity, but molybdenum has the opposite effect. As with titanium, the magnitude of the effects varies with temperature.

The actual width of the single-phase austenite region is decreased when molybdenum is added to the system, because of the ability of the molybdenum to form cubic Mo_3C_2 and dissolve in the TiC. Addition of chromium has a further effect on the activity of molybdenum, further narrowing the range of the single-phase region.

5.1.4.3 Precipitate Phases in Nickel Alloys

Precipitate phases can either improve or degrade the properties of nickel-base alloys. In alloys of the Hastelloy N type, about 16 wt % Mo and 7 wt % Cr, the ubiquitous carbon causes formation of a massive $M_{12}C$ phase at the grain boundaries and causes the alloy to fail intergranularly in a brittle manner. Adding about 2 wt % Ti, however, and lowering the molybdenum content to 12 to 13 wt % can avoid the $M_{12}C$ phase and improve the ductility and strength.

Additional carburization of the alloy, past that usually accommodated in the MC phase, results in the formation of a long, needle-like phase within the alloy, the crystallographic nature of which has not yet been determined. For example, equilibrating at 1215°C with a carbon activity of 0.27 relative to graphite results in the three-phase mixture: alloy, MC phase, and the unknown precipitate.

5.1.5 Thermodynamics of the Face-Centered Cubic Fe-C System – D. J. Bradley,[8] J. M. Leitnaker, and F. H. Horne[9]

The thermodynamics of the Fe-C system is important, both intrinsically and because the system is used as a standard against which other things can be measured. Our re-evaluation disclosed that two values for the equilibrium constant for the $CO-CO_2$ reaction are in general use in the literature.

The discrepancy in the value for the equilibrium constant, which amounts to about 10%, arises from differences in the value of the entropy taken for CO(g). Analysis of spectroscopic data reveals that two sets of high-precision data favor one value of the entropy for CO(g), while another set of low-precision data favors a different, higher value. Our study indicates the lower value to be the correct one.

APPENDIX

Compiled by C. J. McHargue and L. Pyatt

APPENDIX

1. STAFF ASSIGNMENTS

W. H. Butler from Theoretical Studies to Department of Physics, State University of New York at Stony Brook, September 1977–August 1978.

W. A. Coghlan from Radiation Effects to Centre d'Etudes Nucleaires, Fontenay-aux-Roses, France, June 1978–June 1979.

C. C. Koch from Superconducting Materials to ORNL Central Management Offices until June 1978.

R. A. McKee from Surface and Solid State Reactions to Theoretical Physics Division, AERE, Harwell, England, February 1978–January 1979.

R. K. Williams from Physical Properties Research to Institut für Technische Physik, Kernforschungszentrum, Karlsruhe, FRG, until August 1978.

2. GUEST ASSIGNMENTS

B. L. Gyorffy, H. H. Wills Physics Laboratory, University of Bristol, England, to Theoretical Studies, July–September 1977.

J. Harris, Institut für Festkörperforschung, Kernforschungsanlage, Jülich, FRG, June 1978–June 1979.

H. M. Loretto, University of Birmingham, England, to Microstructural Analysis, July–August 1977.

P. Jung, Institut für Festkörperforschung, Kernforschungsanlage, Jülich, FRG, to Radiation Effects until July 1977.

A. Roy, Ben Gurion University, Israel, to Solar Materials Studies, November 1977–November 1978 (half time with Energy Division).

H. Schroeder, Institut für Festkörperforschung, Kernforschungsanlage, Jülich, FRG, January–December 1978.

W. Specking, Institut für Technische Physik, Kernforschungszentrum, Karlsruhe, FRG, June 1978–May 1979.

3. STAFF CHANGES

R. D. Carlson from X-Ray Diffraction Research to Brookhaven National Laboratory, September 1977.

S. David from University of Pittsburgh to Fundamentals of Welding and Joining, September 1977.

T. S. Lundy from Surface and Solid State Reactions to Coordinator of Energy Conservation Programs, October 1977.

R. A. Perkins from Surface and Solid State Reactions to Owens-Corning, January 1978.

N. J. Zaluzec from University of Illinois to Wigner Fellow, Radiation Effects and Microstructural Analysis.

4. UNIVERSITY APPOINTMENTS FOR ACADEMIC YEAR 1977–78

B. S. Borie, Professor, Metallurgical Engineering, University of Tennessee.

C. J. McHargue, Professor, Metallurgical Engineering, University of Tennessee.

R. A. Vandermeer, Professor, Metallurgical Engineering, University of Tennessee.

C. L. White, Adjunct Professor, Materials Science and Engineering, Vanderbilt University.

5. PRESENTATIONS AT TECHNICAL MEETINGS

American Ceramic Society Southeastern Section Meeting, Gatlinburg, Tennessee, July 15–16, 1977

C. S. Yust,* "Basic Mechanisms in the Erosion of Refractories"

International Conference on Crystal Growth, Boston, Massachusetts, July 17–22, 1977

J. D. Holder,* R. A. Hartzell, and G. W. Clark, "$LaCrO_3$ and $YCrO_3$ Eutectics with W, Mo, and Cr"

Gordon Conference on Corrosion, New London, New Hampshire, July 18–22, 1977

R. E. Pawel,* Zircaloy Oxidation in Steam at High Temperatures"

International Cryogenic Materials Conference, Boulder, Colorado, August 2–5, 1977

A. DasGupta,* Y. T. Chou, C. C. Koch, and D. M. Kroeger, "How Effectively Can Grain Boundaries Pin Flux Lines?"

D. S. Easton* and D. M. Kroeger, "Stress Related Damage in Nb_3Sn Superconductors"

D. M. Kroeger,* D. S. Easton, and A. DasGupta, "An Investigation of the Cause of Recoverable Current Degradation Under Stress in Nb_3Sn Superconductors"

A. J. Moorhead,* J. J. Woodhouse, and D. S. Easton, "Cryogenic Mechanical Properties of Solder Joints in a Nb-Ti Superconductor"

---

*Speaker

Twenty-Sixth Annual Denver X-Ray Conference, Denver, Colorado, August 3–5, 1977

Enzo Ricci,* C. J. Sparks, Jr., S. Raman, M. O. Krause, and R. V. Gentry, "X-Ray Fluorescence with Synchrotron Radiation"

M. O. Krause,* E. Ricci, and C. J. Sparks, Jr., "Calculation of X-Ray Fluorescence Cross Sections for K and L Shells"

Physics of Transition Metals Conference, Toronto, Canada, August 15–19, 1977

W. H. Butler,* The Rigid Muffin-Tin Approximation for the Electron-Phonon Interaction in Transition Metals"

P. Durham, B. L. Gyorffy,* C. Hague, G. M. Stocks, and W. M. Temmerman, "Soft X-Ray Emission Spectra of Cu_cNi_{1-c} Alloys"

S. Guiliano, B. L. Gyorffy, R. Ruggeri, and G. M. Stocks,* "On the Band Structure of Nb_cMo_{1-c} Alloys"

S. Gordon, W. Temmerman, G. M. Stocks,* and B. L. Gyorffy, "Fermi Surfaces of Concentrated Cu_cNi_{1-c} Alloys"

B. L. Gyorffy,* R. Jordan, D. R. Lloyd, C. M. Quinn, N. V. Richardson, G. M. Stocks, and W. V. Temmerman, "Angle Resolved Photoemission from Cu_cNi_{1-c} Random Alloys"

W. M. Temmerman,* G. M. Stocks, and B. L. Gyorffy, "Solution of the KKR-CPA Equations for Paramagnetic Cu_cNi_{1-c} Alloys"

35th Meeting of the Electron Microscopy Society of America, Boston, Massachusetts, August 22–26, 1977

R. W. Carpenter* and E. A. Kenik, "Stability of Chemical Order in Ni_4Mo Under Fast Electron Irradiation"

E. A. Kenik and J. Bentley,* "Influence of X-Ray Induced Fluorescence on Energy Dispersive of X-Ray Analysis of Thin Foils"

E. A. Kenik,* "Solute Segregation in Stainless Steel Under Irradiation"

15th International Thermal Conductivity Conference, Ottawa, Canada, August 24, 1977

D. L. McElroy,* R. K. Williams, J. P. Moore, and F. J. Weaver, "The Physical Properties of Inconel Alloy 718 from 300 to 1000°C"

J. P. Moore* and R. S. Graves, "The Ettingshausen-Nernst Coefficients and Physical Properties of Nickel and Alumel"

Fifth International Conference on High-Voltage Electron Microscopy, Kyoto Kaikan, Kyoto, Japan, August 29–September 1, 1977

R. W. Carpenter* and E. A. Kenik, "In Situ Radiation Response of Nickel-Molybdenum Alloys in an HVEM"

Fourth European Crystallographic Meeting, Oxford, England, August 29–September 2, 1977

R. W. Hendricks,* "The ORNL 10-Meter Small-Angle X-Ray Scattering Camera"

International Conference on Nuclear Structure, Tokyo, Japan, September 5–10, 1977

S. Raman,* R. V. Gentry, C. J. Sparks, Jr., W. H. Christie, M. O. Krause, E. Ricci, C. A. Gossett, and J. B. Bates, "New Results from Studies on Radioactive Giant Halos"

American Ceramic Society Fall Meeting of the Nuclear and Basic Science Divisions, Hyannis, Massachusetts, September 25–28, 1977

R. A. Perkins,* J. B. Bates, and L C Manley, Jr., "Tritium Diffusion in Rutile"

Joint Working Group on Uranium Alloys, Golden, Colorado, September 14–15, 1977

R. A. Vandermeer,* J. C. Ogle, and W. B. Snyder, "Shape Memory Effects in an Uranium–6 w/o Niobium Alloy"

State University of New York at Stony Brook, New York, Sept. 28, 1977

G. M. Stocks, "Abinitio Theory of Electronic States in Random Substitutional Alloys"

Fourth International Conference on Small-Angle Scattering of X Rays and Neutrons, Gatlinburg, Tennessee, October 3–7, 1977

S. K. Baczek, R. S. Stein,* R. D. Carlson, and R. W. Hendricks, "The Use of Anisotropic Small-Angle X-Ray Scattering Data for the Study of Deformation in Polymer Systems"

R. D. Carlson,* M. E. Druyan, and P. W. Goaz, "Small-Angle X-Ray Scattering from Developing Teeth"

R. W. Carpenter,* J. Bentley, and E. A. Kenik, "Small-Angle Electron Scattering in the Transmission Electron Microscope"

R. W. Hendricks,* "The ORNL 10-Meter Small-Angle X-Ray Scattering Camera"

J. S. Lin,* O. B. Cavin, R. W. Hendricks, and E. L. Fuller, Jr., "Characterization of an Alumina-Supported Cobalt-Molybdate Catalyst"

J. S. Lin,* R. W. Hendricks, L. A. Harris, and C. S. Yust, "Microporosity and Micromineralogy in a Bituminous Coal by SAXS and EM"

S. Liu,* J. Moteff, R. W. Hendricks, and J. S. Lin, "Small-Angle X-Ray Scattering Studies of Voids in Neutron-Irradiated Molybdenum"

J. Schelten* and R. W. Hendricks,* "Recent Developments in X-Ray and Neutron Small-Angle Scattering Instrumentation and Data Analysis"

J. M. Schultz,* J. S. Lin, and R. W. Hendricks, "A Dynamic Study of the Crystallization of Polyethylene from the Melt"

S. Spooner,* H. R. Child, and F. W. Wiffen, "Small-Angle Neutron Scattering of Reactor-Irradiated Niobium"

R. L. Stephenson,* R. W. Hendricks, and J. S. Lin, "A Computerized Small-Angle Scattering Bibliography"

Seminar at the Department of Metallurgy and Materials Science, Lehigh University, Bethlehem, Pennsylvania, October 4, 1977

A. DasGupta,* "Superconducting Properties, Materials, and Applications"

University of Tennessee Graduate Seminar, Department of Chemical and Metallurgical Engineering, Knoxville, Tennessee, October 18, 1977

J. D. Holder,* "Soret-Modified Eutectic Constitutional Supercooling Criterion"

J. D. Holder* and G. W. Clark, "Directional Solidification by Internal Zone Melting of Cr_2O_3-Mo Composites"

University of Illinois, Urbana, Illinois, October 20, 1977

R. A. Vandermeer, "Shape Memory Effects in Uranium Alloys"

TMS-AIME Fall Meeting, Chicago, Illinois, October 24–27, 1977

P. T. Carlson,* "Intrinsic Diffusion and Vacancy Flow Effects in Vanadium-Titanium Alloys"

A. DasGupta* and D. M. Kroeger, "Flux Pinning by Small Perturbations of the Order Parameter in Type II Superconductors"

D. S. Easton,* "Stress Behavior of Superconducting Composites Containing Filaments with Varying Thicknesses of Nb_3Sn"

J. S. Faulkner,* "Electronic States in Metals and Alloys"

R. W. Hendricks,* "Materials Science Research Applications of the ORNL 10-Meter Small-Angle X-Ray Scattering Camera"

C. C. Koch,* "Recent Developments in Fluxoid Pinning and Stress Effects"

D. M. Kroeger,* D. S. Easton, J. O. Scarbrough, and A. DasGupta, "Dependence of $H_{c2}(T)$ on Tensile Stress for Some Superconducting Composite Conductors"

C. J. McHargue,* "Annealing of Defects Produced by Irradiation"

R. A. Perkins,* "Diffusion of Oxygen in Oxygen Stabilized α-Zircaloy-4"

C. J. Sparks, Jr.,* "Uses of Synchrotron Radiation for Materials Science Research"

R. A. Vandermeer and W. B. Snyder, Jr., "Recrystallization of Deformed Tantalum Single Crystals"

M. H. Yoo* and J. O. Stiegler, "Growth Kinetics and 'Preference Factor' of Frank Loops During Electron Irradiation"

Stanford Synchrotron Radiation Project Users Meeting, Stanford, California, October 27–28, 1977

C. J. Sparks, Jr.,* E. Ricci, S. Raman, M. O. Krause, H. L. Yakel, and R. V. Gentry, "X-Ray Fluorescence Analysis with Synchrotron Radiation"

University of Louisville, Louisville, Kentucky, October 28, 1977

L. K. Mansur,* "Theory of Radiation-Induced Swelling in Metals and Alloys"

University of Texas, Materials Science Laboratory, Austin, Texas, October 20, 1977

R. A. McKee,* "Current Research in the Surface and Solid State Reactions Group"

Materials Research Society Conference on Catalysis, Boston, Massachusetts, November 14–16, 1977

G. S. Painter,* "Theoretical Studies of the Electronic Structure and Bonding Properties of Stepped Metal Surfaces"

Solar Energy Review Meeting, Ames Laboratories, Ames, Iowa, November 29–30, 1977

J. D. Holder,* C. P. Finch, R. A. Hartzell, and G. W. Clark, "EFG and IZG Studies of Potential Significance to Si Crystal Growth"

National Bureau of Standards Metallurgy Seminar Series, Gaithersburg, Maryland, January 11, 1978

R. A. McKee,* "The Oxidation of Fe in Pure Sulfur Vapor"

Duke University College of Engineering, Invited Seminar, Durham, North Carolina, January 20, 1978

R. W. Carpenter,* "Analytical Electron Microscopy"

Robert A. Welch Foundation Lecture Program, Texas A & M University, February 22, Sam Houston State University, February 23, and West Texas State University, February 24, 1978

C. J. Sparks, Jr.,* "Synchrotron Radiation-Intense Photon Source to Study the Chemistry of Materials or Synchrotron Radiation-Applications to Materials Science Research"

AIME Annual Meeting, Denver, Colorado, February 26–March 2, 1978

J. Bentley* and F. W. Wiffen, "Neutron Irradiation Damage in Molybdenum at High Temperatures"

W. A. Coghlan* and M. H. Yoo, "Modeling the Growth Kinetics of Frank Loops Under HVEM Irradiation Using Calculated Defect Preference Factors"

R. W. Hendricks* and W. C. Koehler, "The National Small-Angle Neutron Scattering Facility"

R. W. Hendricks,* "The ORNL 10-Meter Small-Angle X-Ray Scattering Camera"

J. M. Leitnaker* and J. Bentley, "Precipitation Phases in Type 321 Stainless Steel After Aging 17 Years at Approximately 600°C"

J. M. Leitnaker* and D. P. Edmonds, "Aging of 16-8-2 Welds Produces Changes in Martensite Content Which Can Be Explained By Microstructural Analysis"

M. H. Yoo, "Nucleation and Growth of Interstitial Dislocation Loops in Irradiated Foils"

Atomics International Division of Rockwell International, Rocky Flats Plant, February 24, 1978

R. A. Vandermeer, "The Physical Metallurgy of the Uranium–6 w/o Niobium Alloy"

Case Western Reserve University, Cleveland, Ohio, March 7, 1978

G. M. Stocks, "Electronic States in Random Substitutional Alloys: Theory and Experiment"

American Chemical Society Meeting, Anaheim, California, March 12–19, 1978

P. H. Karr, P. W. Predecki,* R. W. Hendricks, and J. S. Lin, "Melting Temperature and Lamellar Thickening During Isothermal Crystallization of Bulk Polyoxymethylene"

Oak Ridge Associated Universities Invited Lecture, March 14, 1978

R. W. Carpenter,* "High-Voltage and Analytical Electron Microscopy"

International Association for Dental Research, Washington, DC, March 16–19, 1978

M. E. Druyan,* P. W. Goaz, R. D. Carlson, and R. W. Hendricks, "Small-Angle X-Ray Scattering from Developing Teeth"

American Crystallographic Association Meeting, Norman, Oklahoma, March 19–24, 1978

R. W. Hendricks* and W. C. Koehler, "The National Small-Angle Neutron Scattering Facility"

C. J. Sparks, Jr.,* "X-Ray Cross Sections for Microanalytical Detection Limits"

Vanderbilt University, Nashville, Tennessee, March 22, 1978

C. L. White,* "Application of Auger Electron Spectroscopy to the Study of Interfacial Segregation"

American Physical Society Meeting, Washington, DC, March 27–30, 1978

P. T. Carlson,* "The Concentration and Temperature Dependence of Cd Diffusivity Enhancement in Pb-Cd Alloys"

A. DasGupta* and D. M. Kroeger, "Flux Pinning by the First Order Perturbation of Ginzburg-Landau Free Energy in Type II Superconductors"

J. S. Faulkner,* "Krein's Theorem and Cluster Calculations"

R. W. Hendricks* and W. C. Koehler, "The National Small-Angle Neutron Scattering Facility"

G. S. Painter* and G. M. Stocks, "Surface Electronic Structure of Cu-Ni Alloys in a Thin Film Model"

J. M. Schultz, J. S. Lin, and R. W. Hendricks,* "A Dynamic Study of the Crystallization of Polyethylene from the Melt"

G. M. Stocks,* B. L. Gyorffy, and W.M.E. Temmerman, "A Complete Solution of the KKR-CPA Equations"

G. M. Stocks* and G. S. Painter, "Cluster Calculation of the Electronic Structure of Oxygen Chemisorbed on the Aluminum (111) Surface"

F. J. Pinski and W. H. Butler,* "Electron-Phonon Interaction in Nb and Mo: Theory"

F. J. Pinski, P. B. Allen, and W. H. Butler,* "Calculation of Resistivity and Electron-Phonon Coupling in Pd"

C. L. Snead, Jr.,* K. G. Lynn, A. N. Goland, and F. W. Wiffen, "Swelling of Neutron-Irradiated Mo and Mo–0.5 Ti by Means of Positron Annihilation"

R. K. Williams and W. H. Butler,* "Electron-Phonon Interaction and Lattice Thermal Conductivity of Metals"

Fifth International Conference on Textures of Materials, Rheinisch-Westfalische Technische Hochschule, Aachen, West Germany, March 29–April 1, 1978

R. A. Vandermeer* and C. B. Cavin, "The Development of Texture and its Role in Shape Memory Behavior in a Uranium Alloy"

Workshop on Large Coil Project Forced-Flow Conductors, ORNL, March 31, 1978

D. S. Easton* and D. M. Kroeger, "Effect of Layer Thickness and Void Formation in Nb_3Sn Superconductors"

Workshop on Use of Dual-Ion Beams in Basic Radiation Effects Research, ORNL, April 12–13, 1978

K. Farrell,* "Dual-Ion Studies at ORNL"

L. K. Mansur,* "Outline of Important Areas for Research Using Dual-Ion Beams"

First Annual Symposium on Solid State Science Materials Problems Associated with Solar Energy, Arizona State University, Tempe, Arizona, April 12–14, 1978

A. S. Roy,* "Economic Viewpoints on Solar Photovoltaic Cells"

Scanning Electron Microscopy Meeting, Los Angeles, California, April 17–21, 1978

L. A. Harris* and C. S. Yust, "SEM and EMA Studies of an SRC Pilot Plant Carbonaceous Plug"

Nb_3Sn Workshop, ORNL, April 26–27, 1978

D. S. Easton* and D. M. Kroeger, "Stress Effects in Nb_3Sn Conductors"

American Society for Metals Educational Seminar, Knoxville-Oak Ridge ASM Chapter, Oak Ridge, April 28, 1978

D. S. Easton,* "Stress Effects in Superconducting Composites"

J. D. Holder,* "Metal Oxide-Metal Eutectic Composites: Synthesis and Applications"

American Ceramic Society, Detroit, Michigan, May 6–11, 1978

C. F. Yen, C. S. Yust, and G. W. Clark, "Mechanical Strength of TiB_2-Fe Composites"

International Conference on Residual Additives and Materials Properties, London, May 15–17, 1978

C. L. White,* R. E. Clausing, and L. Heatherly, "The Effect of Trace Element Additions on the Grain Boundary Composition of Ir + 0.3% W Alloys"

University of Oxford Metallurgy Department Seminar, Oxford, England, May 18, 1978

C. L. White,* Grain Boundary Segregation and Fracture in Iridium Alloys"

Electrochemical Society Meeting, Seattle, Washington, May 21–26, 1978

R. A. McKee, J. V. Cathcart,* and R. E. Pawel, "Oxidation Kinetics of Zircaloy in Steam and Oxygen"

R. E. Pawel,* J. V. Cathcart, and R. A. McKee, "The Kinetics of Oxidation of Zircaloy-4 in Steam at High Temperatures"

R. A. McKee* And G. F. Petersen, "Preparation and Characterization of High Purity Pyrrhotite"

R. A. McKee* and R. E. Druschel, "The Oxidation of Iron in Pure Sulfur Vapor at 0.01 mm Hg and 700°C

Superconductivity Panel Meeting of the Interagency Advanced Power Group, ORNL, May 22, 1978

D. S. Easton* and D. M. Kroeger, "The Superconducting and Mechanical Behavior of Superconducting Conductors Under Tensile Stress"

A. DasGupta, "Recent Results on Flux Pinning in Type II Superconductors and New Superconducting Materials"

American Nuclear Society, San Diego, California, June 19–22, 1978

T. C. Reiley,* R. L. Auble, R. M. Beckers, E. E. Bloom, M. G. Duncan, P. Jung, and M. S. Saltmarsh, "The Oak Ridge Irradiation Creep Facility"

6. PUBLICATIONS

S. C. Abrahams, others and H. L. Yakel, "A. Crystalline," pp. 37–47 in *X-Ray, Neutron, and Electron Scattering, Report of a Materials Science Workshop held at Oak Ridge National Laboratory, April 13–15, 1977,* CONF-770449.

B. W. Batterman, others and R. W. Hendricks, "E. Defects, Inhomogeneities, and Polymers," pp. 77–85 in *X-Ray, Neutron, and Electron Scattering, Report of a Materials Science Workshop held at Oak Ridge National Laboratory, April 13–15, 1977,* CONF-770449.

G. S. Bauer and R. W. Carpenter, "Hydrogen Induced Twinning in Thin Nickel Foils," paper 2B12 in *2nd Int. Congr. Hydrogen in Metals, Paris, June 6–11, 1977,* French Society for Metals, Paris.

S. L. Bennett, C. B. Finch, H. L. Yakel, J. Brynestad, and G. W. Clark, "Crystal Growth of Monoclinic Eu_2O_3 from Molten NaF," *J. Cryst. Growth* 41: 309–10 (1977).

A. D. Brailsford and L. K. Mansur, "Effect of Self-Ion Injection in Simulation Studies of Void Swelling," *J. Nucl. Mater.* 71: 110–16 (1977).

H. Brumberger and R. W. Hendricks, Eds., *Remarks Delivered at the Awards Ceremony* (4th Int. Conf. Small-Angle Scattering of X Rays and Neutrons, Gatlinburg, Tenn., U.S.A., Oct. 3–7, 1977), ORNL/TM-6317.

W. H. Butler, H. G. Smith, and N. Wakabayashi, "Electron-Phonon Contribution to the Phonon Linewidth in Nb: Theory and Experiment," *Phys. Rev. Lett.* 39(16): 1004–07 (October 1977).

R. W. Carpenter and E. A. Kenik, "In-Situ Radiation Response of Nickel-Molybdenum Alloys in an HVEM," *Proc. Fifth Intern. Conf. High Voltage Electron Microscopy, Kyoto, Japan,* 577–80 (1977).

R. W. Carpenter, editor, "Materials Requirements for Unconventional Energy Systems," *Met. Trans. 9A,* 142 (1978).

J. V. Cathcart, "The Role of Stress Effects in the Oxidation Behavior of High Temperature Alloys," pp. 99–119 in *Proc. Symp. Properties of High Temperature Alloys with Emphasis on Environmental Effects,* Proc. Vol. 77-1, ed. by Z. A. Foroulis and F. S. Pettit, The Electrochemical Society, Princeton, N. J., 1976.

W. A. Coghlan and M. H. Yoo, "Modeling and Growth of a Finite Interstitial Loop Under Irradiation," (Summary) *Trans. Am. Nucl. Soc.* 27(TANSAO 27): 330–32 (November–December 1977).

D. G. Doran, G. R. Odette, L. K. Mansur, and R. L. Simons, "Damage Correlation in Theory and Practice," *Radiation Effects in Breeder Reactor Structural Materials,* M. L. Bleiberg and J. W. Bennett, eds., American Institute of Mining, Metallurgical, and Petroleum Engineers, New York, 591 (1977).

K. Farrell, "3.7 Radiation Damage," pp. 325–27 in *Conf. Proc. Low Activation Materials Assessment for Fusion Reactors,* Spec. Rep. EPRI-ER-328-SR, Electric Power Research Institute, March 1977.

J. S. Faulkner, "Scattering Theory and Cluster Calculations," *J. Phys. C: Solid State Phys.* 10: 4661–70 (1977).

C. B. Finch, G. W. Clark, and M. M. Abraham, "Crystal Growth of Calcium Oxide from the Molten Solvent LiF–20 mole % CaF_2," *J. Cryst. Growth* 39(2): 223–26 (August 1977).

C. B. Finch, R. L. Fellows, and J. P. Young, "Self-Luminescence of Several Fluorite-Structure Halides Doped with Curium or Berkelium," *J. Lumin.* 16(1): 109–15 (1978).

R. J. Gray, J. F. King, J. M. Leitnaker, and G. M. Slaughter, "Examination of a Failed Transition Weld Joint and the Associated Base Metals," pp. 115–44 in *Microstructural Science Volume 5,* ed. by J. D. Braun, H. W. Arrowsmith, and J. L. McCall, Elsevier, New York, 1977.

R. J. Gray, V. K. Sikka, J. M. Leitnaker, D. P. Edmonds, R. S. Crouse, and R. T. King, "A Metallographic Study of Ferrite – Sigma Transformation Using Ferromagnetic Colloid, Microprobe Analysis, and Color Etching," pp. 65–84 in *Microstructural Science Volume 5*, ed. by J. D. Braun, H. W. Arrowsmith, and J. L. McCall, Elsevier, New York, 1977.

R. Grynszpan, K. G. Lynn, C. L. Snead, Jr., A. N. Goland, and F. W. Wiffen, "Positron-Annihilation Investigation of High-Temperature Neutron-Irradiated Molybdenum," *Phys. Lett.* 62A(6): 459–62 (19 September 1977).

B. L. Gyorffy and G. M. Stocks, "Electronic States in Random Substitutional Alloys: The CPA and Beyond," *Electrons in Finite and Infinite Structures*, ed. by P. Phariseau and L. Scheire, Plenum Press, NATO Advanced Study Institute Series, 1977.

B. L. Gyorffy, G. M. Stocks, W. M. Temmerman, R. Jordan, D. R. Lloyd, C. M. Quinn, N. V. Richardson, "Angle Resolved Photo-emission from a 001 Surface of Single Crystal $Ni_{23}Cu_{77}$ Random Solid Solution," *Solid State Commun.* 23: 637–49 (1977).

L. A. Harris, D. N. Braski, and C. S. Yust, "A Study of Factors Affecting Elemental Analyses by STEM," pp. 54–59 in *Ceramic Microstructures '76: with Emphasis on Energy Related Applications*, ed. by R. M. Fulrath and J. A. Pask, Waterview Press, Boulder, Colorado, 1977.

L. A. Harris, C. S. Yust, and R. S. Crouse, "Direct Determination of Pyritic and Organic Sulfur by Combined Coal Petrography and Microprobe Analysis (CPMA) – A Feasibility Study," *Fuel* 56: 456–57 (October 1977).

R. W. Hendricks, J. Schelten, and G. Lippmann, "Studies of Voids in Neutron-Irradiated Aluminum Single Crystals. III. Determination of Void Surface Properties," *Philos. Mag.* 36(4): 907–21 (1977).

R. W. Hendricks, "The ORNL 10-Meter Small-Angle X-Ray Scattering Camera," *J. Appl. Cryst.* 11: 15–30 (1978).

A. Jostsons, R. G. Blake, J. G. Napier, P. M. Kelly, and K. Farrell, "Faulted Loops in Neutron Irradiated Zirconium," *J. Nucl. Mater.* 68: 267–76 (1977).

E. A. Kenik, "Simulation of Radiation Damage and Stability in Type 316 Stainless Steel," (Summary) *Trans. Am. Nucl. Soc.* 27(TANSAO 27): 275 (November–December 1977).

C. C. Koch and D. S. Easton, *Mechanical Behavior and Stress Effects in Hard Superconductors – A Review*, ORNL/TM-5857 (November 1977).

C. C. Koch and D. S. Easton, "A Review of Mechanical Behavior and Stress Effects in Hard Superconductors," *Cryogenics* 17(7): 391–413 (1977).

T. G. Kollie, "Measurement of the Thermal Expansion Coefficients of Nickel from 300 to 1000 K and Determination of the Power Law Constants Near the Curie Temperature," *Phys. Rev. B* 16(11): 4872–81 (1977).

M. O. Krause, C. W. Nestor, Jr., C. J. Sparks, Jr., and E. Ricci, *X-Ray Fluorescence Cross Sections for K and L X Rays of the Elements*, ORNL-5399 (June 1978).

H. P. Krautwasser, R. L. Beatty, V. J. Tennery, and C. S. Yust, "Comparison of Pyrolytic Carbon Microstructures, Derived from MAPP-Gas and Propylene," pp. 467–76 in *Ceramic Microstructures '76 with Emphasis on Energy Related Applications*, ed. by R. M. Fulrath and J. A. Pask, Westview Press, Boulder, Colorado, 1977.

J. M. Leitnaker and J. Bentley, "Precipitate Phases in Type 321 Stainless Steel After Aging 17 Years at 600°C," *Metall. Trans.* 8A: 1605–13 (October 1977).

J. M. Leitnaker, G. A. Potter, D. J. Bradley, J. C. Franklin, and W. R. Laing, *The Composition of Eta Carbide in Hastelloy N After Aging 10,000 hr at 815°C*, ORNL-5340 (November 1977).

J. M. Leitnaker, G. A. Potter, D. J. Bradley, J. C. Franklin, and W. A. Laing, "The Composition of Eta Carbide in Hastelloy N After Aging 10,000 h at 815°C," *Metall. Trans. A* 9A: 397–400 (March 1978).

V. W. Lindberg, J. D. McGervey, and R. W. Hendricks, "Annealing Studies of Voids in Neutron-Irradiated Aluminum Single Crystals by Positron Annihilation," *Philos. Mag.* 36(1): 117–28 (July 1977).

T. S. Lundy, "Use of the Hart-Mortlock Equation to Interpret Tracer Diffusion Results," *Scr. Metall.* 12(1): 95–98 (1978).

K. G. Lynn, C. L. Snead, A. L. Goland, and F. W. Wiffen, "Positron-Annihilation Investigation of High-Temperature Neutron-Irradiated Molybdenum," *Phys. Letters* 62A: 459–62 (1977).

L. K. Mansur and W. G. Wolfer, "Influence of a Surface Coating in Void Formation," *J. Nucl. Mater.* 69/70(1&2): 825–29 (February 1978).

L. K. Mansur and W. G. Wolfer, *A Study of the Effect of Void Surface Coatings on Radiation-Induced Swelling*, ORNL/TM-5670 (September 1977).

L. K. Mansur, M. H. Yoo, and W. A. Coghlan, "The Effect of Impurities on Void Nucleation and Growth," (Summary) *Trans. Am. Nucl. Soc.* 27(TANSAO 27): 332–35 (November–December 1977).

L. K. Mansur and M. H. Yoo, *The Effects of Impurity Trapping on Irradiation-Induced Swelling and Creep*, ORNL/TM-6134 (December 1977).

J. D. McGervey, V. W. Lindberg, and R. W. Hendricks, "Positron Lifetimes in Voids and Other Defects in Annealed Neutron-Irradiated Aluminum," *J. Nucl. Mater.* 69/70(1&2): 809–12 (February 1978).

C. J. McHargue and J. L. Scott, "Materials Requirements for Fusion Reactors," *Metall. Trans.* 9A: 151–59 (February 1978).

A. J. Moorhead, J. J. Woodhouse, and D. S. Easton, "Soldering of Copper-Clad Niobium-Titanium Superconductor Composite," *Welding J. (Miami)* 56(10) 23–31 (October 1977).

G. S. Painter, "Bonding in a Cu (001) Monolayer," *Phys. Rev. B* 17: 3848–52 (May 1978).

G. S. Painter, "Bonding of Oxygen on Aluminum: Relation Between Energy Band and Cluster Models," *Phys. Rev. B* 17(12): 662–71 (January 1978).

G. S. Painter, "Level Ordering of States in a Cu (001) Monolayer," *Phys. Rev. B* 17(10): 3848–52 (May 1978).

G. S. Painter, "Theoretical Models of the Electronic Structure of Surface Irregularities," *Mater. Research Bull.* 13: 541 (1978).

R. E. Pawel, R. A. Perkins, R. A. McKee, J. V. Cathcart, G. J. Yurek, and R. E. Druschel, "Diffusion of Oxygen in Beta-Zircaloy and the High Temperature Zircaloy-Steam Reaction," pp. 119–33 in *Zirconium in the Nuclear Industry, Spec. Tech. Publ.* 633, American Society for Testing and Materials, Philadelphia, 1977.

R. A. Perkins, "The Diffusion of Oxygen in Oxygen – Stabilized α-Zirconium and α-Zircaloy-4," *J. Nucl. Mater.* 73(1): 20–29 (1978).

R. A. Perkins, "Oxygen Diffusion in β-Zircaloy," *J. Nucl. Mater.* 68(2977): 148–60 (1977).

R. A. Perkins and R. A. Padgett, Jr., "Oxygen Diffusion in Niobium and Nb–Zr Alloys," *Acta Metall.* 15: 1221–30 (1977).

T. C. Reiley and P. Jung, "The Simulation of Irradiation Creep," *Radiation Effects in Breeder Reactor Structural Materials*, M. L. Bleiberg and J. W. Bennett, eds., American Institute of Mining, Metallurgical, and Petroleum Engineers, New York, 95 (1977).

T. C. Reiley, R. L. Auble, R. M. Beckers, E. E. Bloom, M. G. Duncan, P. Jung, and M. S. Saltmarsh, "The Oak Ridge Irradiation Creep Facility," *Trans. Am. Nucl. Soc.* 28: 186–87 (1978).

G. M. Stocks, B. L. Gyorffy, W. M. Temmerman, R. Jordon, C. M. Quinn, and N. V. Richardson, "Angle Resolved Photoemission from 001 Surface of Single Crystal $Ni_{23}Cu_{77}$ Random Substitutional Alloys," *Solid State Comm.* 23: 637 (1977).

G. M. Stocks, B. L. Gyorffy, E. S. Guiliano, and R. Ruggeri, "The Coherent Potential Approximation for Nonoverlapping Muffin-Tin Potentials: Paramagnetic Ni_xCu_{1-x}," *J. Phys. F* 7(9): 1859–66 (1977).

R. A. Strehlow, L. A. Harris, and C. S. Yust, "Submicron-Sized Mineral Component of Vitrinite," *Fuel* 57: 185–86 (March 1978).

R. A. Vandermeer, J. C. Ogle, W. B. Snyder, Jr., "Shape Memory Effects in a Uranium + 14 at. % Niobium Alloy," *Scr. Metall.* 12(3): 243–48 (March 1978).

C. L. White and W. A. Coghlan, "The Spectrum of Binding Energies Approach to Grain Boundary Segregation," *Metall. Trans.* 8A: 1403–12 (September 1977).

C. L. White and D. F. Stein, "Sulfur Segregation to Grain Boundaries in Ni_3Al and $Ni_3(Al,Ti)$ Alloys," *Metall. Trans.* 9A: 13–22 (January 1978).

R. K. Williams, R. S. Graves, and J. P. Moore, *A Study of the Effects of Several Variables on the Thermal Conductivity of 2 1/4 Cr-1 Mo Steel,* ORNL-5313 (April 1978).

W. G. Wolfer, L. K. Mansur, and J. A. Sprague, "Theory of Swelling and Irradiation Creep," pp. 841–64 in *Radiation Effects in Breeder Reactor Structural Materials,* M. L. Bleiberg and J. W. Bennett, eds. American Institute of Mining, Metallurgical and Petroleum Engineers, New York, 1977.

M. H. Yoo, "Dislocation Loop Growth and Void Swelling in Bounded Media by Charged Particle Damage," *J. Nucl. Mater.* 68: 193–204 (January 1977).

M. H. Yoo, "General Rate Theory Model of Void Swelling in Irradiated Metals," (Summary) *Trans. Am. Nucl. Soc.* 27(TANSAO 27): 326–27 (November–December 1977).

M. H. Yoo and J. O. Stiegler, "Growth Kinetics and 'Preference Factor' of Frank Loops in Nickel During Electron Irradiation," *Philos. Mag.* 36(6): 1305–15 (September 1977).

M. H. Yoo and J. O. Stiegler, "Point Defect Interactions and Growth of Dislocation Loops," *J. Nucl. Mater.* 69/70(1&2): 813–15 (February 1978).

Theses

Daniel Joseph Bradley, *The Thermodynamics of Carbon in Nickel Based Alloys*, Ph.D. Thesis, Michigan State University. Published as ORNL/TM-6282 (April 1978).

Gregory Raymond Gessel, *Effects of Minor Alloying Additions on the Strength and Swelling Behavior of an Austenitic Stainless Steel*, Ph.D Thesis, Iowa State University. Published as ORNL/TM-6359 (June 1978).

Publications Pending

S. K. Baczek, "The Use of Anisotropic Small-Angle X-Ray Scattering Data for the Study of Deformation in Polymer Systems," submitted to *Journal of Polymer Science, Polymer Physics Edition.*

J. B. Bates and R. A. Perkins, "Infrared Spectral Properties of Hydrogen, Deuterium, and Tritium in TiO_2," submitted to *Physics Review.*

E. E. Bloom and W. G. Wolfer, "In-Reactor Deformation and Fracture of Austenitic Stainless Steels," to be published in the proceedings of ASTM Ninth International Symposium on Effects of Radiation on Structural Materials, Richland, WA, July 10–14, 1978.

B. S. Borie, "On the Observation of Forbidden Bragg Maxima in White Tin," accepted by *Physica Status Solidi,* Issue I, Vol. 47.

D. J. Bradley, J. M. Leitnaker, and F. J. Horne, "A Re-Analysis of the Thermodynamics of the f.c.c. Iron-Carbon System," submitted to *Metallurgical Transactions.*

D. J. Bradley, J. M. Leitnaker, and F. J. Horne, "The Precipitation of Carbon in Nickel and Nickel-Titanium Alloys," submitted to *Metallurgical Transactions.*

D. J. Bradley, J. M. Leitnaker, W. R. Laing, and F. J. Horne, "Inaccuracies in NBS Standard Reference Materials Used for Carbon Analyses," submitted to *Analytical Chemistry.*

D. N. Braski and J. M. Leitnaker, "Homogenization of Ti-Modified Alloys and Consequences to Mechanical and Corrosion Properties," submitted to *Metallurgical Transactions.*

J. Brynestad and H. L. Yakel, "Preparation and Structure of Anhydrous Zinc Chloride," to be published in *Inorganic Chemistry.*

W. H. Butler, "Momentum Dependence of the Electron-Phonon Interaction in Nb," to be published in *Journal of Physics.*

W. H. Butler and R. K. Williams, "Electron Phonon Interaction and Lattice Thermal Conductivity," submitted to *Physics Review.*

P. T. Carlson, "Intrinsic Diffusion and Vacancy Flow Effects in Vanadium-Titanium Alloys," accepted by *Metallurgical Transactions.*

R. W. Carpenter and G. S. Bauer, "Electron-Optical Investigations of Hydrogen-Induced Deformation in Nickel Single-Crystal Foils," submitted to *Acta Metallurgica.*

R. W. Carpenter and M. H. Loretto, "Observations of Dislocations Near θ′ Precipitates in Neutron-Irradiation Al–4% Cu by WBDF," to be published in the proceedings Ninth International Conference on Electron Microscopy, Toronto, Aug. 1–9, 1978.

R. W. Carpenter and E. A. Kenik, "In-Situ Radiation Response of Nickel-Molybdenum Alloys in an HVEM," to be published in the proceedings of the 5th International Conference on High-Voltage Electron Microscopy, Kyoto Kaikan, Kyoto, Japan, Aug. 29–Sept. 1, 1977.

R. W. Carpenter and J. J. Zaluzec, "Transmission Scanning Diffraction and Microscopy in a TME/STEM Instrument," to be published in the proceedings of Workshop on Analytical Electron Microscopy, Cornell University, July 24–28, 1978.

R. W. Carpenter, "Application of an Analytical Electron Microscope to Surface Deformation and Wear Research," to be published in the proceedings Ninth International Congress on Electron Microscopy, Toronto, Aug. 1–9, 1978.

R. W. Carpenter, J. Bentley, and E. A. Kenik, "Small-Angle Electron Scattering in the Transmission Electron Microscope," to be published in *Journal of Applied Crystallography*.

R. W. Carpenter and M. H. Yoo, "The Effect of Semicoherent Precipitation on Void Swelling and Segregation in Al-Cu Alloys," submitted to *Metallurgical Transactions*.

W. A. Coghlan, "A Program to Calculate Deformation Maps using an HP-9821A Calculator," ORNL/TM-6441 (in press).

A. DasGupta, C. C. Koch, D. M. Kroeger, and Y. T. Chou, "How Effectively Can Grain Boundaries Pin Flux Lines?" accepted for publication in *Advances in Cryogenic Engineering*.

A. DasGupta, Y. T. Chou, C. C. Koch, and D. M. Kroeger, "Flux Pinning by Grain Boundaries in Niobium Bicrystals," accepted for publication in *Philosophical Magazine*.

R. E. Druschel and R. A. McKee, "A Measurement of the α-γ Transformation Temperature in Iron," submitted to *Journal of Chemical Thermodynamics*.

P. Durham, B. L. Gyorffy, C. Hague, G. M. Stocks, and W. M. Temmerman, "Soft X-Ray Emission Spectra of Cu_cNi_{1-c} Alloys," accepted by *Journal of Physics*.

K. Farrell and R. T. King, "Tensile Properties of Neutron-Irradiated 6061 Aluminum Alloy in Annealed and Precipitation-Hardened Conditions," to be published in the proceedings of ASTM Ninth International Symposium on Effects of Radiation on Structural Materials, Richland, WA, July 11–13, 1978.

K. Farrell and A. E. Richt, "Microstructure and Tensile Properties of Heavily Irradiated 1100-0 Aluminum," to be published in the proceedings of ASTM Ninth International Symposium on Effects of Radiation on Structural Materials, Richland, WA, July 11–13, 1978.

J. S. Faulkner, "Electronic States in Disordered Solids," to be published in the proceedings of the 7th Annual International Symposium on Electronic Structure of Metals and Alloys, Gaubig, East Germany, April 18–22, 1977.

R. W. Gilbert and K. Farrell, "Damage Structure in Zirconium Alloys Irradiated at 573 to 923 K," to be published in the proceedings of Ninth International Congress on Electron Microscopy, Toronto, Aug. 1–9, 1978.

E. S. Giuliano, E. Ruggeri, B. L. Gyorffy, and G. M. Stocks, "Is the Rigid Band Model Valid for Mo_cNb_{1-c} Alloys," accepted by *Journal of Physics F.*

B. Gordon, W. M. Temmerman, B. L. Gyorffy, and G. M. Stocks, "Fermi Surfaces of Concentrated Paramagnetic Cu_cNi_{1-c} Alloys," accepted by *Journal of Physics F.*

B. L. Gyorffy, D. R. Lloyd, M. C. Quinn, N. V. Richardson, G. M. Stocks, and W. M. Temmerman, "Angle-Resolved Photoemission from Single Crystal Random Cu_cNi_{1-c} Alloys," accepted by *Journal of Physics F.*

L. A. Harris, "The Application of Near-Infrared Microscopy to Materials Science," submitted to *Microstructural Science.*

L. A. Harris and C. S. Yust, "SEM and EMA Studies of an SRC Pilot Plant Carbonaceous Plug," to be published in the proceedings Scanning Electron Microscopy Meeting, Los Angeles, April 17–21, 1978.

L. A. Harris, C. R. Kennedy, and C. S. Yust, "A Study of Solids Formed in a Solvent-Refined Coal Pilot Plant," submitted to *Fuel.*

L. A. Harris and C. S. Yust, "Transmitted Near Infrared Microscopy of Coal," submitted to *Fuel.*

L. A. Harris and O. B. Cavin, "Interference of Intruded Epoxy Mounting on X-Ray Diffraction Results from Carbonaceous Materials," submitted to *Carbon.*

R. W. Hendricks and L. B. Schaffer, "The International Project for the Calibration of Absolute Intensities," to be published in *Journal of Applied Crystallography.*

P. H. Karr, P. Predecki, R. W. Hendricks, and J. S. Lin, "Kinetics of Lamellar Thickening During Isothermal Crystallization of Polyoxymethylene from the Melt," submitted to *Journal of Macromolecular Science – Physics.*

C. C. Koch, "Technetium," to be published in "Data Compilation" for Vol. 1 of *Metals Handbook*, American Society for Metals, Metals Park, Ohio.

M. B. Lewis and R. A. Perkins, "The Source of Oxygen in the Anodization of Vanadium," submitted to *Journal of the Electrochemical Society*.

J. S. Lin, R. W. Hendricks, L. A. Harris, and C. S. Yust, "Microporosity and Micromineralogy in a Bituminous Coal," submitted to *Journal of Applied Crystallography*.

S. Liu, J. Moteff, R. W. Hendricks, and J. S. Lin, "Small-Angle X-Ray Scattering Studies of Voids in Neutron-Irradiated Molybdenum," submitted to *Journal of Applied Crystallography*.

L. K. Mansur, "Void Swelling in Metals and Alloys Under Irradiation: An Assessment of the Theory," submitted to *Journal of Nuclear Technology*.

L. K. Mansur and M. H. Yoo, "The Effects of Impurity Trapping on Irradiation-Induced Swelling and Creep," submitted to *Journal of Nuclear Technology*.

L. K. Mansur, "Irradiation Creep Due to Climb-Enabled Glide of Dislocations Resulting from Preferred Absorption of Point Defects," submitted to *Philosophical Magazine*.

L. K. Mansur, "The Temperature Shift of Swelling with Changes in Radiation Dose Rate," submitted to *Journal of Nuclear Materials*.

L. K. Mansur and W. G. Wolfer, "The Reduction of Irradiation-Induced Creep by Point Defect Trapping," to be published in the proceedings of ASTM Ninth International Symposium on Effects of Radiation on Structural Materials, Richland, WA, July 10–14, 1978.

M. J. McCready, J. M. Schultz, J. S. Lin, and T. W. Hendricks, "Effect of Crystallization Time on the Properties of Melt-Crystallized Linear Polyethylene," to be published in *Journal of Polymer Science: Polymer Physics Edition*.

R. A. McKee, "The Concentration Dependence of Solute Diffusion for an Alloy in Dissociative Equilibrium," submitted to *Philosophical Magazine*.

J. P. Moore and R. S. Graves, "The Ettingshausen-Nernst Coefficient and Transport Properties of Alumel from 200 to 473 K," submitted to *Journal of Physics and Chemistry of Solids*.

J. P. Moore, T. G. Godfrey, R. S. Graves, F. J. Weaver, and W. P. Eatherly, "Experimental Determinations of the Pre- and Postirradiation Thermal Transport and Thermal Expansion Properties of Simulated Fuel Rods for an HTGR," to be published in *Journal of Nuclear Materials*.

N. H. Packan, K. Farrell, and J. O. Stiegler, "Correlation of Neutron and Nickel-Ion Damage in Pure Nickel," submitted to *Journal of Nuclear Materials*.

N. H. Packan and W. A. Coghlan, "Injecting Irradiation Samples with a Uniform Concentration of Helium Using ^{244}Cm," submitted to *Nuclear Technology*.

D. A. Papaconstantopoulos, B. M. Klein, J. S. Faulkner, and L. L. Boyer, "Coherent Potential Approximation Calculations for PdH_x," submitted to *Physical Review*.

F. J. Pinski, P. B. Allen, and W. H. Butler, "Calculated Electron-Phonon Coupling and Superconducting T_c of Transition Metals: Mo and Pd," to be published in the proceedings LT-15 Conference, Grenoble, France, Aug. 15–20, 1978.

F. J. Pinski, P. B. Allen, and W. H. Butler, "Electron-Phonon Contribution to Electrical Resistivity and Superconducting 'p-Wave' Transition Temperature of Pd," submitted to *Physical Review Letters*.

A. S. Roy, "Model for Comparing the Cost of Flat Array and Concentrator Photovoltaic Solar-Cell Systems," to be published in the proceedings 13th IEE Photovoltaic Specialists Meeting, Washington, D.C., June 5–8, 1978.

A. S. Roy, "A Practical Electrochemical Transport Equation for Concentrated Solutions," submitted to *Journal of the Electrochemical Society*.

A. S. Roy, "Economic Methodology for Solar-Power Generating Systems," to be published in the proceedings 13th Intersociety Energy Conversion Engineering Conference, San Diego, Aug. 20–25, 1978.

J. Schelten and R. W. Hendricks, "Recent Developments in X-Ray and Neutron Small-Angle Scattering Instrumentation and Data Analysis," submitted to *Journal of Applied Crystallography*.

J. M. Schultz, J. S. Lin, and R. W. Hendricks, "A Dynamic Study of the Crystallization of Polyethylene from the Melt," submitted to *Journal of Applied Crystallograpy*.

C. J. Sparks, "Mosaic Crystals for Obtaining Larger Energy Bands and High Intensities from Synchrotron Radiation Sources," to be published in a report on the Workshop on X-Ray Instrumentation for Synchrotron Radiation Research, Stanford, Synchrotron Radiation Laboratory, Stanford, CA, April 3–5, 1978.

C. J. Sparks, "Synchrotron Radiation Provides an Intense Photon Source to Probe Matter," to be published in *Physics News in 1977* by the American Institute of Physics.

G. M. Stocks, W. M. Temmerman, and B. L. Gyorffy, "A Complete Solution of the KKR-CPA Equations: Cu-Ni Alloys," submitted to *Physical Review Letters*.

W. M. Temmerman, B. L. Gyorffy, and G. M. Stocks, "Solutions of the KKR-CPA Equations for Paramagnetic Cu_cNi_{1-c} Alloys," accepted by *Journal of Physics*.

W. M. Temmerman, B. L. Gyorffy, and G. M. Stocks, "The Atomic Sphere Approximation to the KKR-CPA: Electronic Structure of Paramagnetic Cu_cNi_{1-c} Alloys," accepted by *Journal of Physics F*.

R. A. Vandermeer and O. B. Cavin, "The Development of Texture and Its Role in Shape Memory Behavior in a Uranium Alloy," to be published in the proceedings 5th International Conference on Texture of Materials, Rheinisch-Westfalische Technische Hochschule, Aachen, West Germany, March 29–April 1, 1978.

C. L. White, R. E. Clausing, and L. Heatherly, "The Effect of Trace Element Additions on the Grain Boundary Chemistry of Ir + 0.3% W Alloys," submitted to *Metallurgical Transactions*.

H. L. Yakel and J. Brynestad, "A Refinement of the Crystal Structure of Orthorhombic Zinc Chloride," submitted to *Inorganic Chemistry*.

D. W. Yarbrough and R. K. Williams, "Method for Estimating the Lattice Thermal Conductivity of Metallic Alloys," ORNL-5434 (in press).

C. F. Yen and R. L. Coble, "Defect Centers in Gamma-Irradiated Single Crystal Al_2O_3," submitted to *Journal of the American Ceramic Society*.

M. H. Yoo, "A Generalized Model of Void Swelling — The Depth Dependent Swelling by Self-Ion Irradiation," submitted to *Journal of Nuclear Materials*.

C. S. Yust, "Unifying Factors in Erosion and the Wear of Machine Elements," to be published in the proceedings International Conference on Fundamentals of Tribology, Massachusetts Institute of Technology, Cambridge, June 19–23, 1978.

C. S. Yust and R. S. Crouse, "Melting at Particle Impact Sites During Erosion of Ceramics," submitted to *Wear*.

N. J. Zaluzec, "Optimizing Conditions for X-Ray Microchemical Analysis for Analytical Electron Microscopy," to be published in the proceedings Ninth International Congress on Electron Microscopy, Toronto, Aug. 1–9, 1978.

BLANK PAGE

METALS AND CERAMICS DIVISION

AUGUST 1, 1978

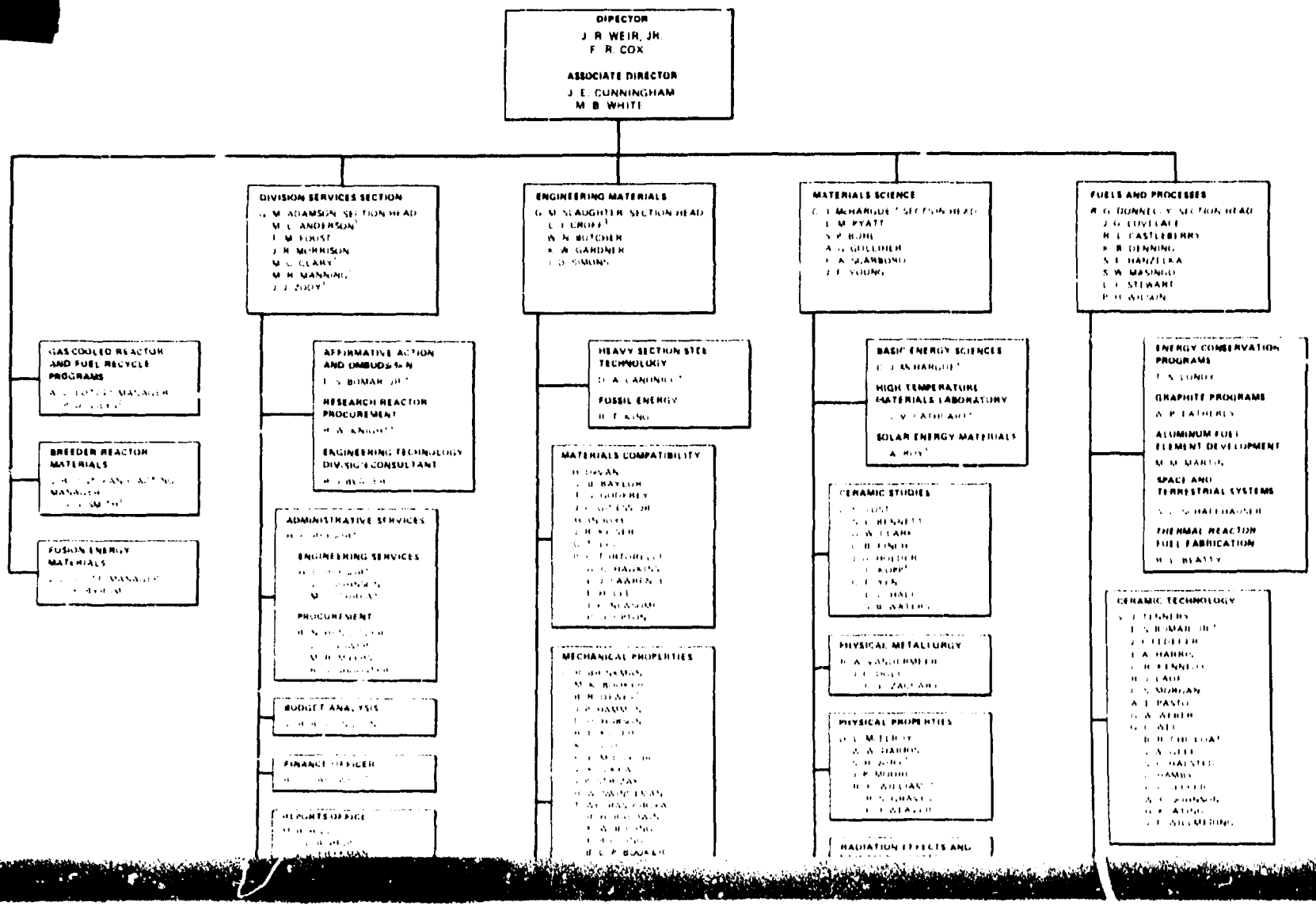

BLANK PAGE

AND FUEL CYCLE PROGRAMS

BREEDER REACTOR MATERIALS

FUSION ENERGY MATERIALS

AND OMBUDSMAN

RESEARCH REACTOR PROCUREMENT

ENGINEERING TECHNOLOGY DIVISION CONSULTANT

ADMINISTRATIVE SERVICES

ENGINEERING SERVICES

PROCUREMENT

BUDGET ANALYSIS

FINANCE OFFICER

REPORTS OFFICE

C. E. FREEMAN
G. E. HARGUS[5]
J. P. HOLLEY[5]
J. C. JACKSON
N. A. RICHARDS[5]
K. A. WITHERSPOON[5]

QUALITY ASSURANCE

R. J. BEAVER[5]

SAFETY, RADIATION, AND SAM CONTROL

A. D. MILLER JR.
H. A. KNIGHT[5]
J. B. FLYNN[5]

TECHNICAL EDITOR

S. PETERSON

TRU OPERATIONS

C. C. WILLIAMS
B. J. STRADER
W. JENNINGS JR.

METALLOGRAPHY

R. J. GRAY[5]
P. S. CROUSE
R. L. LESLIE
M. D. ALLEN
L. ANGEL
S. W. [illegible]
E. R. BOYD
A. H. FARMER
P. HALTOM
T. J. HENSON
C. N. HOOD
T. L. MARLAR[5]
J. R. MAYFIELD
J. W. NAVE
N. H. ROUSE
R. J. RUSSELL
L. O. SHRADER

TECHNOLOGY

D. A. CANONICO[5]

FOSSIL ENERGY

R. T. KING

MATERIALS COMPATIBILITY

J. H. DEVAN
C. R. BAYLOR
T. G. GODFREY
J. C. GRIESS JR.
H. [illegible]
J. R. KEISER
C. T. LIU
P. F. TORTORELLI
W. C. HARRIS
C. J. LAWRENCE
R. E. LEE
J. H. NEKSON
R. C. SVENSON

MECHANICAL PROPERTIES

C. R. BROOKMAN
W. R. CORWIN
J. M. DEVAN[5]
J. A. HAMMONS
D. G. HOOD[5]
R. L. KLUEH
P. T. LEE
J. M. MCCLAIN JR.
C. E. PAGE
J. P. SMITH[5]
L. GORDON VAN
T. NISHIOKA[5]
J. M. ALEXANDER
P. S. BOLING
E. E. [illegible]
R. L. PERSON
L. K. EGNER
J. C. FEATHER
J. L. GRIFFITH
B. MCNABB JR.
T. D. OWINGS JR.
E. B. PATTON JR.
C. T. RATCLIFF
C. O. STEVENS
B. C. WILLIAMS

NONDESTRUCTIVE TESTING

R. A. MCCLUNG
J. ADLER[5]
R. S. GOOR
W. S. HYLTON[5]
J. [illegible] DODD
D. W. FLETTING[5]
R. E. FOSTER
G. A. SCOTT
W. A. SIMPSON JR.
J. H. SMITH
C. D. SNYDER
L. D. CHITWOOD
R. A. CUNNINGHAM JR.
F. V. DAVIS
W. J. MASON

PRESSURE VESSEL TECHNOLOGY

D. A. CANONICO[5]
R. G. BERGOSSIAN
C. E. LONG JR.
R. A. NANSTAD
W. J. STELZMAN
R. D. WILLIAMS
T. N. JONES JR.
R. L. WAY

WELDING AND BRAZING

J. W. [illegible]
S. [illegible]
D. P. EDMONDS
J. J. KING
J. W. MCELHENEY

C. J. MCHARGUE[5]

HIGH TEMPERATURE MATERIALS LABORATORY

J. V. CATHCART[5]

SOLAR ENERGY MATERIALS

A. [illegible]

CERAMIC STUDIES

[illegible]
S. L. BENNETT
G. W. CLARK
C. R. FINCH
J. O. HOLDER
[illegible] KOPP[5]
C. T. YEN
E. C. HALL
S. R. WATTS

PHYSICAL METALLURGY

R. A. VANDERMEER
J. G. [illegible]
C. E. ZACHARY

PHYSICAL PROPERTIES

D. C. MCCLUNG
A. A. HARRIS
S. H. [illegible][5]
[illegible] MOORE
R. A. ALLEN[5]
R. S. GRAVES
P. J. SLAVIN

RADIATION EFFECTS AND MICROSTRUCTURAL ANALYSIS

J. O. STIEGLER
J. BENTLEY
E. E. BLOOM
D. N. BRASKI
H. W. CARPENTER
R. L. CLAUSING
W. A. COGHLAN[5]
R. H. DOROSE
L. C. EMERSON
K. FARRELL
G. R. GESSEL
M. L. GROSSBECK
J. A. KINK
E. H. LEE
J. M. LEITNAKER
M. B. LEWIS
L. K. MANSUR
P. J. MAZIASZ
P. MOODY-ZEWSKI
N. H. PACKAN
T. C. REILEY
A. F. ROWCLIFFE
H. SCHROEDER[5]
P. S. SKEAD
C. L. WHITE
F. W. WIFFEN
W. J. ZALOZEC
R. A. BOND
R. L. [illegible]
C. [illegible] GIBSON
[illegible] HEATHERLY
J. E. HOUSTON
M. B. [illegible]
L. G. MCKAMEY
G. A. POTTER
R. H. SHANNON
W. H. SMITH
J. F. [illegible]

SUPERCONDUCTIVITY

[illegible] KOSS
C. W. CROEVER
A. DASGUPTA
D. S. EASTON
A. SPEZIALI[5]

PROGRAMS

T. S. LUNDY

GRAPHITE PROGRAMS

W. P. EATHERLY

ALUMINUM FUEL ELEMENT DEVELOPMENT

W. M. MARTIN

SPACE AND TERRESTRIAL SYSTEMS

A. L. SCHAFFHAUSER

THERMAL REACTOR FUEL FABRICATION

R. L. BEATTY

CERAMIC TECHNOLOGY

V. J. TENNERY
E. S. R. MAE JR.[5]
J. J. FEDERER
C. A. HARRIS
C. R. KENNEDY
R. J. LAUF
C. S. MORGAN
A. E. PASTO
G. A. REBER
G. C. ALT
R. B. [illegible]
J. A. [illegible]
S. C. HALSTED
C. [illegible]
C. [illegible]
A. R. [illegible]
[illegible] LATTAU
J. F. [illegible]

FUEL CYCLE ENGINEERING

R. A. BRADLEY
B. J. BAXTER[14]
J. A. CARPENTER JR.
D. R. JOHNSON
R. R. JUDKINS
A. R. OLSEN
T. F. SCANLAN
H. R. TIVESEY
H. J. WALLACE

FUEL CYCLE TECHNOLOGY

W. J. LACKEY
P. ANGELINI
A. J. CAPUTO
R. F. HELMS[14]
I. D. MACK
H. [illegible][5]
J. [illegible] SEITZ
D. P. STINTON
R. R. SUCHOMEL
S. M. TIEGS
S. W. COOK
C. E. DAVOST
A. H. ELLIOTT JR.
J. B. FLYNN[5]
G. F. GALLOWAY
G. S. HENDRICKS
J. C. MCLAUGHLIN
W. R. STINES

FUELS EVALUATION

J. J. HOMAN
J. A. HOMAR
E. L. LONG JR.
J. M. ROBBINS
B. A. THIELE[5]
T. N. TIEGS
J. W. WOODS
D. W. HEATHERLY
P. J. JONES
E. L. RYAN

ON LOAN/LEAVE

A. M. BRADLEY
J. H. GOODEN[5]
R. H. [illegible]
A. H. GRAY[5]
W. J. KANNA[5]
A. PATHARKAR[5]
P. [illegible]
B. D. KEIST
T. [illegible]
G. A. SPEZIALI

BLANK PAGE

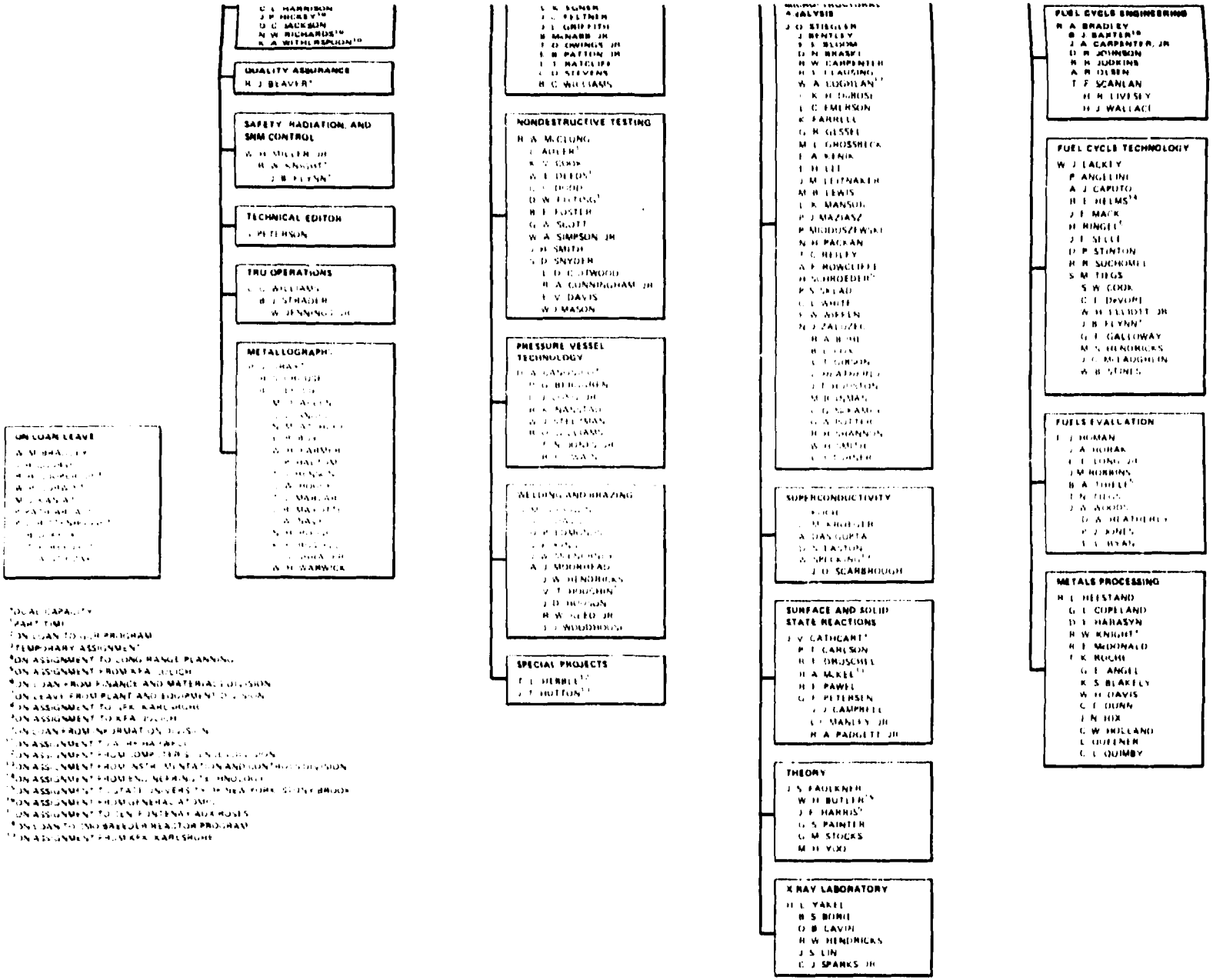

*LOCAL CAPACITY
[1]PART TIME
[2]ON LOAN TO U.S. PROGRAM
[3]TEMPORARY ASSIGNMENT
[4]ON ASSIGNMENT TO LONG RANGE PLANNING
[5]ON ASSIGNMENT FROM RFA, JÜLICH
[6]ON LOAN FROM ENGINEERING AND MATERIALS DIVISION
[7]ON LEAVE FROM PLANT AND EQUIPMENT DIVISION
[8]ON ASSIGNMENT TO JFR, KARLSRUHE
[9]ON ASSIGNMENT TO RFA, JÜLICH
[10]ON LOAN FROM SEPARATION DIVISION
[11]ON ASSIGNMENT TO A.D. HARRIS, INC.
[12]ON ASSIGNMENT FROM COMPUTER SCIENCES DIVISION
[13]ON ASSIGNMENT FROM ASSESSMENTS AND CONSERVATION DIVISION
[14]ON ASSIGNMENT FROM ENGINEERING TECHNOLOGY
[15]ON ASSIGNMENT TO STATE UNIVERSITY OF NEW YORK, STONY BROOK
[16]ON ASSIGNMENT FROM GENERAL ATOMIC
[17]ON ASSIGNMENT TO GENERAL ATOMICS
[18]ON LOAN TO SNR BREEDER REACTOR PROGRAM
[19]ON ASSIGNMENT FROM KFK, KARLSRUHE

BLANK PAGE

ORNL-5437
Distribution
Category UC-25

INTERNAL DISTRIBUTION

1–2. Central Research Library
3. Document Reference Section
4–13. Laboratory Records Department
14. Laboratory Records, ORNL RC
15. ORNL Patent Office
16. G. M. Adamson
17. J. Bentley
18. B. S. Borie
19. C. R. Brinkman
20. W. H. Butler
21. D. A. Canonico
22. P. T. Carlson
23. R. W. Carpenter
24. J. V. Cathcart
25. G. W. Clark
26. R. E. Clausing
27. W. A. Coghlan
28. J. H. Coobs
29. F. L. Culler
30. J. E. Cunningham
31. A. DasGupta
32. J. H. DeVan
33. J. R. DiStefano
34. W. H. Dodson
35. R. G. Donnelly
36. D. S. Easton
37. K. Farrell
38. J. S. Faulkner
39. C. B. Finch
40. G. M. Goodwin
41. R. J. Gray
42. W. O. Harms
43. L. A. Harris
44. R. L. Heestand
45. R. W. Hendricks
46–48. M. R. Hill
49. J. D. Holder
50. D. W. Jared
51. L. H. Jenkins
52. O. L. Keller
53. E. A. Kenik
54. C. C. Koch
55. W. C. Koehler
56. D. M. Kroeger
57. J. M. Leitnaker
58. M. B. Lewis
59. R. S. Livingston
60. A. L. Lotts
61. L. K. Mansur
62. R. W. McClung
63. D. L. McElroy
64. F. K. McGowan
65–74. C. J. McHargue
75. J. P. Moore
76. J. C. Ogle
77. S. M. Ohr
78. N. H. Packan
79. G. S. Painter
80. P. Patriarca
81. R. E. Pawel
82. S. Peterson
83. M. T. Robinson
84. A. F. Rowcliffe
85. A. C. Schaffhauser
86. J. L. Scott
87. G. M. Slaughter
88. C. J. Sparks
89. P. H. Stelson
90. J. O. Stiegler
91. G. M. Stocks
92. V. J. Tennery
93. D. B. Trauger
94. R. A. Vandermeer
95. J. R. Weir, Jr.
96. C. L. White
97. F. W. Wiffen
98. M. K. Wilkinson
99. R. K. Williams
100. C. E. Winters
101. R. F. Wood
102. H. L. Yakel, Jr.
103. M. H. Yoo
104. F. W. Young, Jr.
105. A. Zucker

BLANK PAGE

106. R. W. Balluffi (consultant)
107. P. M. Brister (consultant)
108. F. C. Brown (consultant)
109. J. H. Frye, Jr. (consultant)
110. W. R. Hibbard, Jr. (consultant)
111. M. J. Mayfield (consultant)
112. A. W. Overhauser (consultant)
113. N. E. Promisel (consultant)
114. C. G. Shull (consultant)
115. John Stringer (consultant)

EXTERNAL DISTRIBUTION

116. S. Amelinckx, SCK/CEN, B. 2400 Mol, Belgium
117. K.H.G. Ashbee, H. H. Wills Physics Laboratory, University of Bristol, Bristol, England
118. W. Bauer, Physical Research, Sandia Laboratories, Livermore, CA 44550
119. J. P. Charlesworth, AERE, Harwell, Didcot, Oxon, OX11, ORB, England
120. J. L. Cook, Executive Vice-President, Silag, Inc., 1251 Avenue of the Americas, New York, NY 10020
121. J. H. Crawford, Jr., Department of Physics, University of North Carolina, Chapel Hill, NC 27514
122. A. N. Goland, Department of Physics, Brookhaven National Laboratory Upton, NY 11973
123. D. Gurinsky, Applied Science Division, Brookhaven National Laboratory, Upton, NY 11973
124. P. Haasen, Institut für Metallphysik, University of Gottingen, Gottingen, West Germany
125. A. L. Hunt, Lawrence Livermore Laboratory, L-386, University of California, P.O. Box 808, Livermore, California 94550
126. W. Johnston, General Electric Research and Development Center, Schenectady, NY 12301
127. Bernard H. Kear, United Technologies Research Center, East Hartford, CT 06108
128. Librarian, Building 465, Atomic Energy Research Establishment, Harwell, Didcot, Oxon, OX11, ORB, England
129. K. Lücke, Technische Hochschule Aachen, Aachen, West Germany
130. R. J. Mauer, Materials Research Laboratory, University of Illinois, Urbana, IL 61801
131. D. J. Michel, Met. Div., Code 6397, Naval Research Laboratory, Washington, DC 20375
132. T. E. Mitchell, Department of Met. and Mat. Sci., Case-Western Reserve University, Cleveland, OH 44106
133. H. Nichol, Director, Institut für Reaktorwerkstoffe, Kernforschungsanlage, Jülich GmbH, 5.7 Jülich 1, Postfach 1913, West Germany
134. B. F. Oliver, Department of Chemical and Metallurgical Engineering, University of Tennessee, Knoxville, TN 37919
135. ORAU Technical Library, MERT Division, Oak Ridge Associated Universities, P.O. Box 117, Oak Ridge, TN 37830
136. L. W. Roberts, Chemistry and Materials Science, Lawrence Livermore Laboratory, P.O. Box 808, Livermore, CA 84550
137. W. Schilling, Institut für Festkorperförschung der Kernforschungsanlage, Jülich, D-517 1, Postfach 365, West Germany

138. W. Schmatz, Institut für Festkorperförschung der Kernforschungsanlage, Jülich, D-517 1, Postfach 365, West Germany
139. A. Seeger, Institut für Theoret und Angew, Physik der Universitat Stuttgart, 7000 Stuttgart 80-Pfaffenwaldring 57/V1, Germany
140. D. Seidman, Department of Materials Science and Engineering, Cornell University, Ithaca, NY 14850
141. D. Shirley, Director, Materials and Molecular Research Division, Lawrence Berkeley Laboratory, Berkeley, CA 94720
142. S. Spooner, Department of Chemical Engineering, Georgia Institute of Technology, Atlanta, GA 30332
143. R. Smallmen, Department of Metallurgy, University of Birmingham, Birmingham, England
144. E. E. Stansbury, Department of Chemical and Metallurgical Engineering, University of Tennessee, Knoxville, TN 37919
145. H. Ullmaier, Institut für Festkorperförschung, Kernforschungsanlage, Jülich, D-517, Jülich 1, Postfach 365, West Germany
146. F. L. Vook, Dept. 5110, Sandia Laboratories, Albuquerque, NM 87115
147. J. B. Wagner, Department of Materials Science, Arizona State University, Tempe, AZ 85281
148. M. S. Wechsler, Department of Metallurgy, Iowa State University, Ames, IA 50010
149. A. M. Weinberg, Institute for Energy Analyses, ORAU, Oak Ridge, TN 37830
150. C. Wert, Dept. Met. and Mining Eng., University of Illinois, Urbana, IL 61801
151–158. R. R. Winters, Director, Oak Ridge Science Semester, GLCA Denison University, Main Street, Granville, OH 43023
159. USDOE, Fossil Energy Division, Washington, DC 20545

    H. Frankel

160–162. USDOE, Division of Magnetic Fusion Energy, Washington, DC 20545

    K. M. Zwilsky
    T. C. Reuther
    C. Finfgeld

163–167. USDOE, Division of Materials Sciences, Washington, DC 20545

    J. S. Kane
    L. C. Ianniello
    D. K. Stevens
    M. C. Wittels
    S. Wolf

168. USDOE, Oak Ridge Operations Office, P.O. Box E, Oak Ridge, TN 37830

    Research and Technical Support Division

169–395. USDOE, Technical Information Center, Office of Information Services, P.O. Box 62, Oak Ridge, TN 37830

For distribution as shown in TID-4500 Distribution Category, UC-25 (Materials).

*U.S. GOVERNMENT PRINTING OFFICE: 1978-740-190/230